1-1-2014

Non-Specific Interactions Between Cationic Nanoparticle-Polymer Composites and Biomolecules

Matthew Alexander Caporizzo
University of Pennsylvania, mcaporizzo@gmail.com

Non-Specific Interactions Between Cationic Nanoparticle-Polymer Composites and Biomolecules

Abstract
This dissertation describes the consequences of non-specific binding between cationic nanoparticles (NPs) and biological materials ranging from persistence length reduction of single actin filaments, to modified kinetics of myosin V motility, and culminating with correlating THP-1 cell metabolic stress to viscoelastic changes. The bulk of the thesis (chapters 3-5), utilizes optically transparent polymer-NP composites with controllable hierarchical roughness to tune the interaction strength between actin filaments and the surface and impact myosin V kinetics. To generate hierarchical roughness, precise control over the thermodynamics and dynamics of NH_2-functionalized NPs in polystyrene-ran-acrylic acid (SAA) is demonstrated in chapter 3. In particular, an interplay between aggregation and dispersion of NPs occurs by varying SAA composition, leading to roughness ranging from a few nms to hundreds of nms and tunable wettability with water contact angles ranging from 70° to 170°. Chapter 4 describes the relationship between roughness and actin binding with a model based on the worm-like chain model that weighs the bending energy associated with actin binding to surface features based on their size and density against the electrostatic potential of the surface. The model predicts the experimentally observed weakening of f-actin surface binding with increasing roughness, from immobilized, to side-on wobbly, and eventually end-on. Chapter 5 quantifies how perturbations in actin structure by electrostatic surface attachment effects myosin V kinetics. Myosin V velocity is slowed by backward stepping on NP-decorated surfaces. The Michaelis-Menten relationship of myosin velocity versus [ATP] exhibits a reduction in K_M and V_{MAX} explained by a reduced coordination between myosin and f-actin which causes backwards stepping and an increased ADP affinity. Chapter 7 outlines the method of variable indentation-rate rheometric analysis by Laplace transform (VIRRAL) which is developed to utilize basic Hertzian fitting of force curves to measure the viscoelasticity of THP-1 cells. Dextran-lysozyme nanogels loaded with Ag nanoparticles cause mitochondrial damage which metabolically stresses cells decreasing the ATP/ADP. Reduced [ATP] increases f-actin concentration and slows intracellular transport making the cytoplasm stiffer by increasing both low and high-frequency elasticity and the viscosity. Thus, metabolic stress in THP-1 cells is correlated with proportional increases in viscosity and elasticity, while the relaxation time of the cell, τ, remains unchanged.

Degree Type
Dissertation

Degree Name
Doctor of Philosophy (PhD)

Graduate Group
Materials Science & Engineering

First Advisor
Russell J. Composto

Keywords
actin, atomic force microsopy, myosin, nanocomposite, roughness, viscoelasticity

Subject Categories
Biomedical | Mechanics of Materials | Toxicology

NON-SPECIFIC INTERACTIONS BETWEEN CATIONIC NANOPARTICLE-POLYMER COMPOSITES AND BIOMOLECULES

Matthew Alexander Caporizzo

A DISSERTATION

In

Materials Science and Engineering

Presented to the Faculties of the University of Pennsylvania in Partial Fulfillment of the Requirements for the Degree of Doctor of Philosophy

2014

Russell J. Composto, Professor of Materials Science and Engineering

Supervisor of Dissertation

Shu Yang, Professor of Materials Science and Engineering

Graduate Group Chairperson

Dissertation Committee:

David M. Eckmann, Department of Anesthesiology

Yale E Goldman, Department of Physiology

Daeyeon Lee, Department of Chemical and Biomedical Engineering

NON-SPECIFIC INTERACTIONS BETWEEN

CATIONIC NANOPARTICLE-POLYMER COMPOSITES AND BIOMOLECULES

Dedicated to the memory of Michael V. Caporizzo

Acknowledgements

Coming to an atmosphere like Penn to do research is an amazing opportunity to "stand on the shoulders of giants" and follow the legendary minds who have come before our time to pave the road ahead of us. I have had an amazing opportunity here at Penn, not only to walk in the footsteps of our Founding Fathers, but to work for some of the great minds of this age. I owe my accomplishments to the patience and direction of my mentors at Penn as well as to the numerous acts of support and encouragement that have come from the amazing family I have. I have also been afforded an extremely unique opportunity by my advisor Russ Composto through the Nano-Bio Interface Center at the University of Pennsylvania to collaborate throughout the entirety of my Ph.D. with the Yale Goldman lab in the Pennsylvania Muscle Institute and get real exposure in the field of biological physics from one of the world's premier experts in molecular motility.

In particular, I am extremely grateful to Professor Russ Composto who has been an extraordinary mentor and advisor and who has shown me that it is possible for the same person to be a loving father and a world-class scientist. (The rarity of which cannot not go under-stated) I arrived at Penn with little research experience, and Russ took me under his wing and has been patient with my dozens of drafts of papers and figures as I slowly learned the scientific writing process. What is perhaps most impressive about Russ is his ability as a teacher to take his expertise of polymer physics and universally share it with graduate students, undergraduate students, and high-school students alike. This is perhaps most evident by Russ's passion for the chemistry of cooking, and I have had the privilege to tag along with him at outreach programs such as one at Central High-school. Making caramels in class to demonstrate the "dehydration polymerization of glucose," you can see the faces of kids of all ages light up as he puts polymer

physics within the realm of their physical perception, and inspires future scientists. This is who Russ is. As far as professor's in the Material's Science Engineering Department, Russ has the reputation for being the most approachable, and he often stuns new graduate students and post docs who have come from labs at other universities when he expresses a genuine concern for their well-being during weekly meetings. My growth as a scientist and a person has benefited immensely from Russ's mentorship because he has allowed me to pursue my own ideas and learn from my own mistakes regardless of his personal agenda.

The project I was assigned to for my dissertation involved the attachment of actin filaments to NP-decorated surfaces combining the work of two of Russ's graduating students, Marla McConnell and Jay Park. As a result I would meet Dr. Yuji Sun a post-doc in the Goldman Lab. Yuji is an amazing scientist, and I was privileged to receive training from him in myosin motility assays and in using FIONA before he left for a faculty appointment. Yuji has the neatest lab notebooks I have ever seen; unfortunately I cannot claim to have picked up note keeping from him. This was how I came into contact with Yale Goldman, whose generosity and willingness to teach has enabled me to become an active part of the Pennsylvania Muscle Institute. Yale has allowed me to take his self-designed feedback class as well as private courses following the literature on myosin kinetics starting with AF Huxley, to Lymn and Taylor, and culminating with his own work in developing single molecule techniques. Yale is a brilliant person, an electrical engineer/MD/PhD, there isn't much he doesn't know, can't fix, or doesn't understand. Consequently presenting at his group meetings could make for some pretty tough Monday mornings, but Yale's continual critical thinking and scientific insight has inspired a degree of rigor in my experimentation and data analysis that I would not have otherwise.

Jody Dantzig is the lab manager of the Goldman Lab, and her continued drive to ensure that everyone is following proper chemical hygiene stems from more than just her motherly

concern for everyone in the lab. Jody has educated me on the importance of precision, repeated controls, and testing of solutions before drawing conclusions from biological assays. For example a vial in the -20 ^{o}C freezer marked “1120 mM ATP” could really contain as much as 10% ADP depending on its age and storage conditions due to the collision complex between ATP and itself leading to the gradual degradation of ATP stock solutions. Thus ATP must always be fresh, and when you first hear this your heart sinks and you being retesting all of your previous results. Jody has been a great friend to me, and I don’t know if I would have had the persistence to continue with a lot of the tedious biological assays if it weren’t for her constant encouragement.

The members of both the Composto and Goldman lab are a constant pleasure to be around. Marla McConnell trained me on how to make NH_2 NPs and graft them to SAA thin films. Thanks to Adam Hendricks for help troubleshooting in the FIONA setup when things were not aligned well and for directing me to the Kerssemakers’ step-finder algorithm. Rob Ferrier, thanks for always being in an awesome mood. Matt Brukman has been a continual help in the now Singh Center, he knows the Asylum instruments better than anyone, and has been my sanity check on more than one occasion when running into the plethora of complications that usually shroud the TIRF-AFM. Thanks to Osamu Sato and Ikebe Mitsuo for synthesizing the myosin V construct that I was able to use for my studies. Thanks to Judith Kandel for teaching me how to culture cells, teaching Charles Roco to culture cells, culturing cells for us, and helping us with the biological aspect of things. Showing me what a cell nucleus looked like at 100x, and showing me how to stain and count cells. Judith is one of the more patient graduate students I have met along the way. Literally every time she used the TIRF-AFM for virtually an entire year something new and different was broken or wrong with the instrument. Thanks Emma-Beth

Parrish and Meg Grady for proofing some of my thesis chapters. And thank you Hyun-Su Lee for teaching me QCM-D.

Thanks to my dissertation committee for being extremely cooperative in setting up a date and time, reading my thesis and helping me get it into the best shape possible. Thanks Daeyeon Lee and David Eckmann for your patience with the date selection and your quality insight into the research in my dissertation. Thank Karen Winey for being willing to stand by at last minute notice if anyone can't make it.

My entire family has truly been amazing as I have delayed the onset of adult life for half a decade. My grandparents, God bless them, are always sending me cards and making sure that I am doing ok. Without my parents I wouldn't have a college degree, let alone a Ph.D. They have been there for me every step of the way, including moving home half way through gradschool, and again during writing my dissertation. They are always thrilled to have me, and they have encouraged me to continue my education long after I lost faith in myself. They have bailed me out more than once, from a car accident, to bike accidents. I could not ask for two better role models in my life.

Matthew A Caporizzo

ABSTRACT

NON-SPECIFIC INTERACTIONS BETWEEN

CATIONIC NANOPARTICLE-POLYMER COMPOSITES AND BIOMOLECULES

Matthew A. Caporizzo

Russell J. Composto

This dissertation describes the consequences of non-specific binding between cationic nanoparticles (NPs) and biological materials ranging from persistence length reduction of single actin filaments, to modified kinetics of myosin V motility, and culminating with correlating THP-1 cell metabolic stress to viscoelastic changes. The bulk of the thesis (chapters 3-5), utilizes optically transparent polymer-NP composites with controllable hierarchical roughness to tune the interaction strength between actin filaments and the surface and impact myosin V kinetics. To generate hierarchical roughness, precise control over the thermodynamics and dynamics of NH_2-functionalized NPs in polystyrene-ran-acrylic acid (SAA) is demonstrated in chapter 3. In particular, an interplay between aggregation and dispersion of NPs occurs by varying SAA composition, leading to roughness ranging from a few nms to hundreds of nms and tunable wettability with water contact angles ranging from 70^o to 170^o. Chapter 4 describes the relationship between roughness and actin binding with a model based on the worm-like chain model that weighs the bending energy associated with actin binding to surface features based on their size and density against the electrostatic potential of the surface. The model predicts the experimentally observed weakening of f-actin surface binding with increasing roughness, from immobilized, to side-on wobbly, and eventually end-on. Chapter 5 quantifies how perturbations in actin structure by electrostatic surface attachment effects myosin V kinetics.

Myosin V velocity is slowed by backward stepping on NP-decorated surfaces. The Michaelis-Menten relationship of myosin velocity vs [ATP] exhibits a reduction in K_M and V_{MAX} explained by a reduced coordination between myosin and f-actin which causes backwards stepping and an increased ADP affinity. Chapter 7 outlines the method of variable indentation-rate rheometric analysis by Laplace transform (VIRRAL) which is developed to utilize basic Hertzian fitting of force curves to measure the viscoelasticity of THP-1 cells. Dextran-lysozyme nanogels loaded with Ag nanoparticles cause mitochondrial damage which metabolically stresses cells decreasing the ATP/ADP. Reduced [ATP] increases f-actin concentration and slows intracellular transport making the cytoplasm stiffer by increasing both low and high-frequency elasticity and the viscosity. Thus, metabolic stress in THP-1 cells is correlated with proportional increases in viscosity and elasticity, while the relaxation time of the cell, τ, remains unchanged.

Table of Contents

List of Tables

List of Figures

Chapter 1: Parameters governing *in-vitro* and *in-vivo* interactions between nanoparticles and biomolecules

1.0 Introduction

The rapid growth of technology continually demands smaller more efficient devices which is met by the synthesis and assembly of smaller components. In walks the nanoparticle, NP. Over one thousand times smaller than the human hair, nanoparticles are stable, microscopic, catalytic units with a vast array of controllable properties. The small scale and versatility of NPs has led to an explosion in their use over a wide variety of applications such as energy storage,[1] chemotherapeutics,[2] sun-screen,[3] anti-microbial coatings,[4] drug delivery,[5] and high-density data storage.[6] As a direct consequence of their frequent use, NPs come in contact with humans on a daily basis. Once considered safe, recent studies show that nanoparticles reduce the activity of enzymes,[7] cause damage to DNA,[8] and mutate cells to appear cancerous.[3] For example, the TiO_2 NPs used in sunscreen are linked to cytotoxicity and inflammation in human fibroblasts and lung cells[9] as well as DNA damage and genetic instability in mice.[10] NP toxicology studies identify the presence of undesirable biological interactions between NPs and biological materials, and work to predict the consequences of NP interactions with a cell. Identifying how a NP will affect a cell is synonymous with identifying what biomolecules the particle associates with in the complex environment of the cytoplasm.[11] Within the cytoplasm there is a dense array of protein, nucleic acid, salt, and lipid which exhibit selective affinities for NPs that depend on the size, shape, and surface chemistry of the NP.[12] *In-vitro* assays regularly

demonstrate reduced activity of NP-associated enzymes,[7,13,14] but correlating these findings with *in-vivo* toxicology requires accurately predicting the biomolecules that will associate with NPs in the cytoplasm. Progress needs to be made to understand the competitive NP-biomolecule interactions that occur in complex environments and ultimately define bioadverse effects. Understanding interactions between nanoparticles and biomolecules is necessary to design NPs that mitigate negative biological effects through processes like surface passivation[15] or more specific targeting.

1.1 Specific Interactions in Biology

Nanoparticles can interact with biological molecules either specifically or non-specifically. A specific interaction is that of a receptor (analogous to a lock) which uniquely recognizes a target structure known as a substrate (analogous to a key) enabling the unique docking of two molecules containing receptor-substrate structures (figure 1.1). By functionalizing NPs with natural or engineered receptors (purple V's and red circles in figure 1.1) and tagging biomolecules with substrate molecules (purple arrows and red U's), specific targeting is achieved even in the presence of a high concentration of contaminant molecules. The "lock and key" model is the ubiquitous biological mechanism by which molecular recognition occurs regularly in a crowded and complex environment.[16] Common examples include antibody/antigen targeting, enzyme catalysis, and signal transduction. The high specificity of the lock and key mechanism is largely attributed to a multiplicity of weak non-covalent interactions creating a single unique strong interaction.[17] Engineered targeting for fluorescent tracking is employed by grafting biomolecules, such as streptavidin, to fluorescent quantum dots to make use of the extremely high affinity ($K_D = 10^{-14} - 10^{-15}$ M)[18] of the streptavidin protein for biotin.[19] Quantum dots, QDs, are CdS, CdSe, CdTe, or PbSe nanoparticles, 10's of nms in size, that are functionalized with streptavidin or other

biomolecules through a number of established functionalization techniques.[19] Streptavidin coating of a fluorescent NP makes it a specific target for biotin. Subsequent engineering of biotin into a specific site on a protein, as depicted in figure 1.1, generates a biomolecule which can be labeled with sub-domain precision by the introduction of the receptor-functionalized quantum dots.[20]

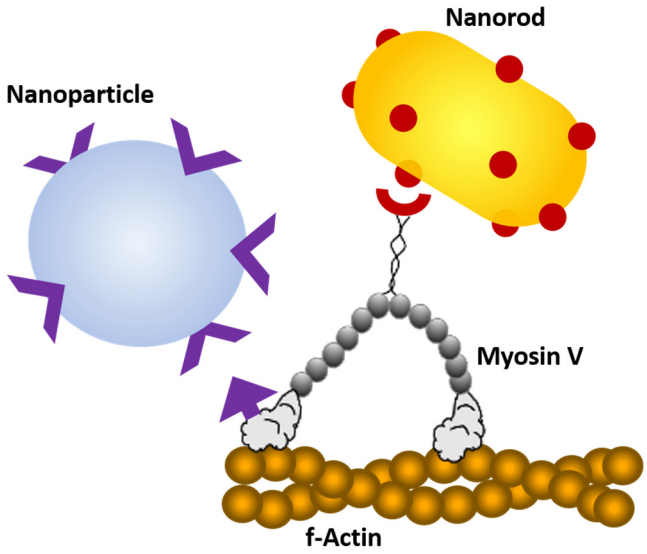

Figure 1.1: Specific binding between a protein and a nanoparticle by grafting a receptor molecule (purple V's and red circles) to a particle and engineering the substrate molecule (purple arrows and red U's) into a specific domain of a protein. Here Myosin V is depicted to be labeled with an arrow at the catalytic head and with a U at the cargo binding tail.

Specific targeting of NPs is desirable in pharmaceutical applications where attaching a drug to a NP creates a particle that targets a biomolecule (frequently an enzyme) as a drug but has a higher potency.[21] NPs offer an advantage over single-compound traditional drugs because direct targeting of NPs to the treatment site (i.e., a tumor) can be achieved by coating the outside of the NP with a targeting ligand that localizes the NP (functionalized with the drug) exclusively to the treatment site in the body.[21] NP delivery enhances therapeutic efficacy and simultaneously minimizes side effects. Not surprisingly NPs are of increasing use in pharmaceutical applications. As the use of NPs in biotechnology increases, addressing the

potential for undesired side-effects of NPs will occur.[22] A working understanding of the core principals governing biocompatibility is necessary to be able to predict and eventually mitigate bioadverse effects of NPs. NPs typically create bioadverse interactions though non-specific binding forces such as van der Waals forces (VDW), hydrophobic interactions, and electrostatic interactions by which NPs interact with any biomolecule.[23] The local surface potential gradient created by a NP can induce structural reorganization of the amino-acids significantly enough to reduce activity.[11]

1.2 Non-specific Binding

By the nature of their environmental exposure, free surfaces are energetically unfavorable and constitute a reactive site. For example, amorphous SiO_2 ionizes to SiO^- in an aqueous environment leading to the non-specific electrostatic accumulation of positively charged molecules on the SiO^- surface and SiO_2 NPs are linked with increased reactive oxygen species (ROS) in cells.[24] ROS readily oxidize surrounding proteins and nucleic acids causing cellular damage referred to as oxidative stress, which the cell regularly works to repair.[25] Increased oxidative stress in cells is linked to carcinoma and triggered cell death.[25] In addition to providing reactive surfaces, association of NPs non-specifically with proteins leads to conformational changes in proteins which reduce their activity without chemical reaction.[7,13,14]

Structural reorganization is the direct response of the 1000's of weak interactions defining a protein's structure to the gradient field introduced by a NP. Figure 1.2 illustrates the denaturing of an enzyme on the surface of a NP. Charge sign and magnitude are some of the most important factors leading to strong non-specific NP-protein interactions that reduce protein activity.[7,26] While proteins contain positive, negative, and apolar residues, the net charge of the protein being opposite in magnitude to the NP shows the largest propensity for

non-specific absorption.[26] For nanoparticles the magnitude of the electrostatic interaction increases with the size of the NP in a meaningful way.[23] Namely, increasing the diameter of SiO_2 particles from 10 nm to 100 nm results in a 60% decrease in adsorbed lysozyme activity that directly correlates with denaturing of the enzyme by circular dichroism, analogous to the illustration in figure 1.2.[7]

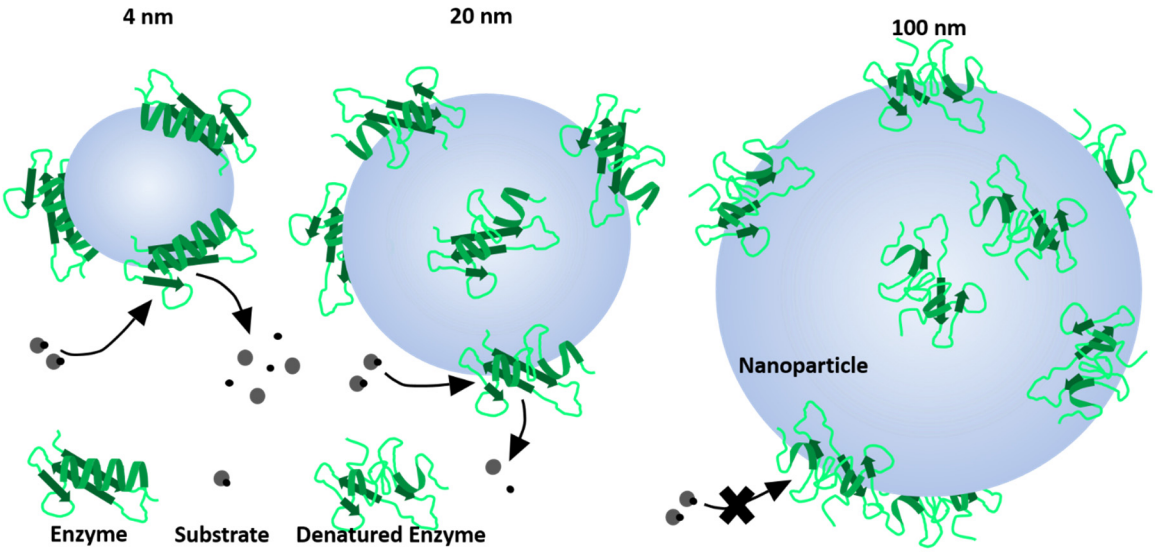

Figure 1.2: Non-specific binding between an enzyme and a nanoparticle reduces enzyme activity by compromising enzyme secondary structure. In the NP diameter range of 1-100 nm the electrostatic potential gradient changes in magnitude enough to significantly affect the activity of small enzymes such as lysozyme. The reduction in activity that occurs as the NP size increases correlates with a loss in secondary structure and a reduced affinity of the enzyme for the substrate.

The first molecular dynamics simulations of protein-NP interactions accurately predict that NP-induced structural changes reduce the activity of L-lactate dehydrogenase (LDH). LDH binding to mercapto-undecanoic acid, MUA, grafted gold NPs (5 nm) decreases the mobility of the solvent-exposed residues of the side chains.[14] A reduction in side chain mobility of LDH leads to an inability to appropriately coordinate with the substrates, lactate and NADH, which translates into decreased activity.[14] Supporting the molecular dynamics simulations,

experimental results show a near 50% reduction in LDH activity when LDH binds non-specifically to MUA-gold.[14]

1.3 The Michaelis-Menten Relationship and NP-modified Kinetics

Enzymes lend themselves particularly well to studying the correlation between structural changes associated with NP-binding and activity loss because the reaction velocity for a typical enzyme is well characterized. Enzymes are proteins that act on substrate molecules to catalyze necessary reactions in the cell. In an enzymatic reaction, (1.1), the enzyme, E, first binds to the substrate, S, to catalyze the conversion of the substrate into the product, P,[27]

$$E + S \underset{k_{-1}}{\overset{k_1}{\rightleftarrows}} ES \xrightarrow{k_f} E + P \quad . \qquad (1.1)$$

The rate of product formation is defined as the reaction velocity, $V = {}^{\partial P}/_{\partial t}$, and depends on the reaction rates and the concentrations of enzyme and substrate. Under the assumption that reaction is in steady state (i.e. ${}^{\partial [S]}/_{\partial t} = 0$ and ${}^{\partial P}/_{\partial t} = constant$), the reaction velocity is well described by the Michaelis-Menten, MM, relationship,[28]

$$V([S]) = \frac{V_{MAX}[S]}{K_M + [S]} \quad . \qquad (1.2)$$

The fundamental parameters of an enzyme's activity as expressed by the MM relationship are the maximal velocity at saturating substrate concentration, V_{MAX}, and the half-saturation substrate concentration, K_M. Under steady state conditions, K_M is an estimate of the dissociation constant of the enzyme-substrate complex and thereby is a good quantitative measure of how structural changes in the enzyme alter an enzyme's affinity for a substrate. The ratio, V_{MAX}/K_M, is a measure of the efficiency of the enzyme in converting the substrate to

product and is sensitive to structural changes within the enzyme's catalytic binding pocket. Measuring the activity of an enzyme as a function of substrate concentration to access MM parameters is a useful way to compare changes in E-S affinity and enzyme catalytic efficiency.

MM kinetics have been employed to measure the effect of NPs on the enzymatic activity of L-lactate dehydrogenase, which binds to β-NADH to convert pyruvate to lactate, figure 1.3.[14] The activity of the complex can be measured by the binding kinetics of either pyruvate or β-NADH to the enzyme and both processes follow MM kinetics. Furthermore, since pyruvate and β-NADH bind at different locations to L-lactate dehydrogenase, the dependence of the kinetics on the [β-NADH] and [pyruvate] probe structural perturbations in different areas of LDH. Figure 1.3 shows that non-specific attachment of L-lactate dehydrogenase to gold NPs increases K_M for β-NADH binding but does not affect K_M for pyruvate binding indicating that the affinity of L-lactate dehydrogenase for β-NADH is reduced by the gold NP while the affinity for pyruvate remains mainly unaffected. V_{MAX} is lower for both β-NADH binding and pyruvate binding as shown by the asymptote in figure 1.3b, c which suggests similar reductions in catalytic efficiency by MUA-gold NPs at both binding sites.[14] Differences in kinetic changes induced by NPs at different catalytic sites suggests that structural changes are heterogeneous and the downstream effects on substrate affinity are difficult to predict. These findings motivate more in-depth work involving systematic changes of NP properties and different enzymes to develop an understanding of the nature and consequences of non-specific interactions.

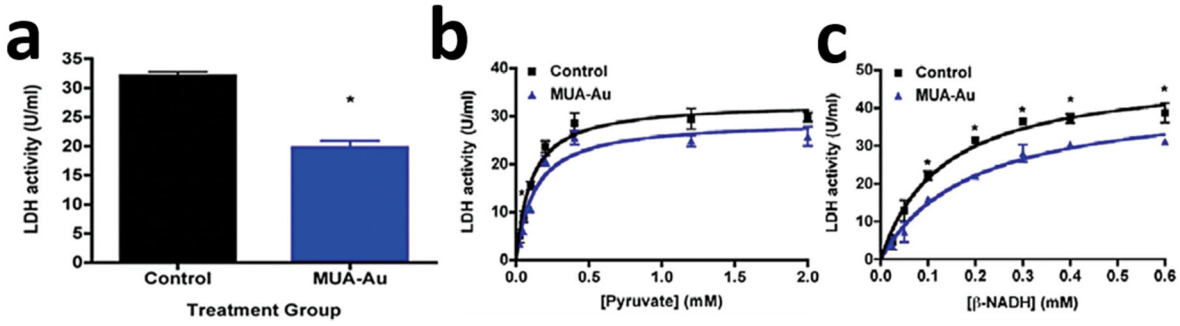

Figure 1.3: Reduction of lactate dehydrogenase activity when bound to MUA-grafted 5 nm gold nanoparticles as a function of substrate concentration. **a.** The overall activity of the dehydrogenase at saturating substrate concentrations is reduced. **b.** Michaelis-Menten kinetics approximate the relationship between [pyruvate] and activity showing a decreased V_{Max} and no change in K_M. **c.** Michaelis-Menten kinetics of LDH activity on [b –NADH] shows a decrease in both K_M and V_{max} suggesting a reduced affinity of LDH for b –NADH drives the reduction in activity. Reproduced with permission.[14]

1.4 Mechano-enzymes for intracellular transport, locomotion, and signaling

Enzymes are abundant in cells and structurally diverse because catalysis of each reaction requires a unique lock-and-key structure for specific recognition analogous to figure 1.1. The class of enzymes responsible for cellular locomotion, intra-cellular transport, and cell signaling are the mechano-enzymes that convert the energy of adenosine triphosphate, ATP, hydrolysis into mechanical force to overcome diffusion inside a cell and move material against a concentration gradient.[29] There are a multitude of different classes of mechano-enzymes which are classified by the filamentous tracks they move on as illustrated in figure 1.4a. Kinesins (purple) and dyneins (green) are microtubule associated motors and myosins (grey) associate with f-actin.[29] Each family of molecular motors has several sub-types that function as passive tethers, mechanical ratchets, or cargo-transporters.[28] The function of a molecular motor is determined by the kinetics of the molecular motor's ATP hydrolysis cycle which is regulated by a combination of weak and strong binding to the filamentous track.[30] For example, myosin acts as

a mechanical ratchet or a cargo transporter if the rate limiting step is phosphate release or ADP release respectively.[30]

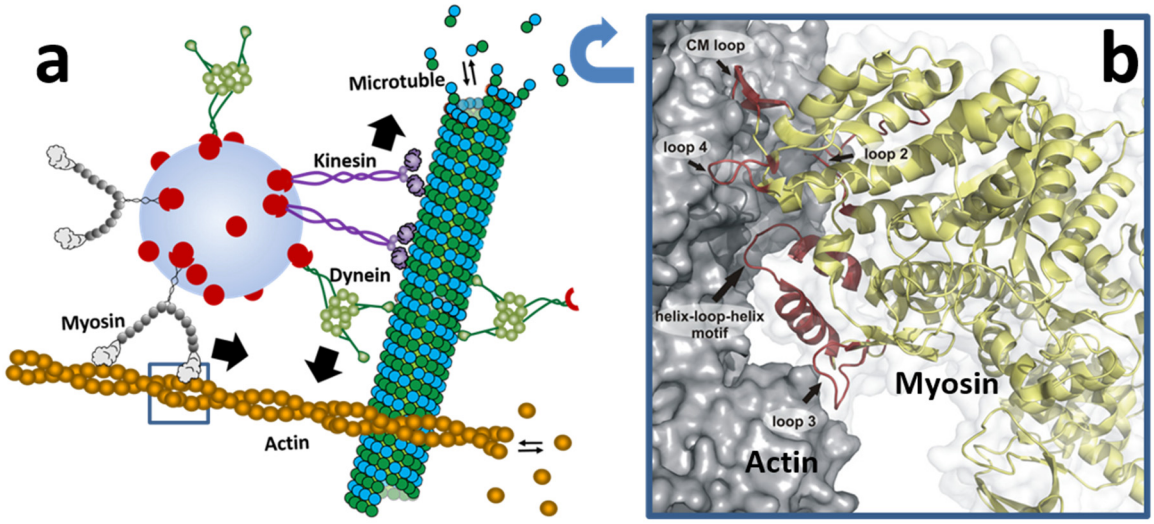

Figure 1.4: Intracellular tug-of-war governs vesicular transport *in-vivo*. a. Schematic showing common molecular motors (myosin, kinesin, and dynein) and their associated dynamic tracks (actin and microtubules) as they drag a specifically labeled cargo (blue sphere decorated with red circles) in a molecular tug-of-war. **b.** Structural docking of myosin V (yellow and red) and f-actin (grey). Interactions between multiple motifs of myosin (red domains) and f-actin govern the weak-strong binding transition in the regulation of ADP and phosphate from myosin to initiate force generating structural changes. Figure 1.4b reproduced with permission.[29a]

The fraction of time a molecular motor spends attached to its track during its catalytic cycle is defined as its duty ratio.[31] Muscle myosin II spends the majority of its catalytic cycle detached from actin so that the catalytic head remains primed for rapid contraction to maximize the power output of muscle.[32] Muscle myosins therefore have a low duty ratio, and phosphate release as the rate limiting step ensures that these myosin spend the majority of their cycle in the phosphate bound structure which has a weak affinity for f-actin.[33] Conversely, cargo transporters, like myosin V, must have a high duty ratio to reduce the probability of dissociating from the actin filament. Cargo transporting myosins are rate limited by ADP release, and spend the majority of the catalytic cycle in the ADP bound, pre-power stroke state, which strongly binds to f-actin.[34a]

When myosin is not associated with actin, completion of the ATPase cycle uses ATP without performing useful work for the cell (futile cycling). Futile cycling is avoided by actin catalyzing ATP hydrolysis in myosin, speeding up hydrolysis byproduct release more than one hundred fold.[34b] Thus, in the absence of actin, myosin can bind ATP and hydrolyze it, but the release of phosphate and ADP are slow so as to block completion of the ATPase cycle and binding of an additional ATP to myosin.[29b] The coordination of myosin and actin is vitally important to catalyze myosin activity. Shown in figure 4b, multiple domains (red) on myosin specifically interact with f-actin as the myosin ATPase cycle progresses to support and catalyze force generation by the molecular motor. Mutations in these loops reduce the coordination of myosin with actin and are linked with disease.[35] For example, mutations in the cardio myopathy, CM, loop (figure 3.4b) reduces coordination between actin and myosin causing insufficient force generation in heart muscle and eventual heart failure, namely hypertrophic CM.[35] The coordination between actin and myosin can also be reduced by NP induced structural changes in actin associated with non-specific NP binding. NP induced changes in actin structure could stress multiple cellular processes as regulation of the multitude of myosin dependent tasks will have altered kinetics. NP-induced changes in myosin kinetics and the actin cytoskeleton motivate the study of the role of molecular motors in NP-induced cell-injury. In particular, *in-vivo* imaging techniques capable of dissecting local kinetics of enzymes with sub-cellular or even single enzyme resolution, would be capable of correlating transport changes associated with molecular motor abnormalities to spatial and temporally localized regions of the cell to more deeply understand the cell-injury process.

1.5 Single-Molecule Kinetics

The kinetics of mechano-enzymes can be measured both *in-vitro* and *in-vivo* with single molecule resolution using Fluorescence Imaging at One Nanometer Accuracy (FIONA).[36] Since

the point spread function limits the resolution of fluorescent microscopy to half the wavelength of light, 100's of nms, the precise location of a fluorescent molecule is calculated by fitting the intensity distribution collected from a fluorophore to the 2-D Gaussian fucntion.[37] The attainable resolution is the quality of the fit and depends on the number of photons collected above the background in an imaging frame.[37] Specific attachment of QDs to mechano-enzymes is a typical method of fluorescent labelling that has the advantage over dye molecules of brightness and fluorescence lifetime. 2D resolution of a few nms is routinely attainable using QD labelling of enzymes specifically attached through the streptavidin-biotin complex. Single molecule detection enables the observation of heterogeneity in populations of molecules that is otherwise averaged out by ensemble measurements.[38] Single-molecule localization is particularly important for *in-vivo* kinetic assays where rates are otherwise inaccessible because biochemical reactions cannot be synchronized inside cells.[38,43]

The step-size and stepping rate of a molecular motor can be measured using FIONA to image the motion of a motor labeled with a QD on the tail domain (cargo domain). Labelling the tail has little effect on the kinetics of ATP hydrolysis of the catalytic heads.[20] However, dissection of inter-head coordination[20] and resolution of individual steps in complex experiments such as molecular motor tug-of-war,[40] have employed specific labelling of the QD directly to the catalytic head of the motor. The hydrodynamic diameter of the QD ranges from 10-50 nm which is commensurate with the size of myosin and may very well "trip" the heads during translocation leading to measurable activity differences.[41] Remarkably, studies where both heads of a processive myosin dimer are labeled with different color quantum dots detect minimal changes in the ATPase kinetics and motor processivity.[20] In this way, motility assays inadvertently demonstrate that strong specific NP-enzyme interactions are capable of occurring without reducing enzyme activity. Specific labelling of QDs to molecular motors avoids the

complications associated with non-specific interactions with the myosin enzyme. Streptavidin coated QDs and domains of myosin that interact with actin are both positively charged and are non-specifically repulsive which minimize affinity changes between myosin and actin associated with specific labelling of QDs.

1.6 The importance of f-actin structure

Structural changes in actin disrupt myosin ATPase kinetics by altering the affinity of actin for myosin. The catalysis of myosin's hydrolysis byproduct release is controlled by the coordination of myosin with actin at five different motifs, namely, the cardiomyopathy, CM, loop, loops 2-4, and the helix-loop-helix motifs, shown in figure 1.4b.[29] The complex coordination between actin and myosin can be altered by the handling of f-actin during experimental procedures. *In-vitro* assays of molecular motors require the immobilization of actin filaments on an artificial surface (typically a glass coverslip) to enable imaging of myosin motors. Actin filaments retain their native structure in these assays by specifically binding to a surface grafted with N-ethylmalemide (NEM) treated myosin bundles. NEM-myosin is typically adsorbed to surfaces coated by a hydrophobic polymer, such as poly-(methyl methacrylate), PMMA, since the hydrophobic tail groups of the myosin preferentially coat the hydrophobic surface leaving the catalytic heads exposed for actin binding. Actin filaments are kept from gliding on the surface by NEM treatment of surface bound myosin because NEM binds with cysteines in myosin rendering it unable to hydrolyze ATP.[42]

Recent studies show that positively charged surfaces can also immobilize f-actin through non-specific binding, and immobilization increases as the surface potential becomes more positive on amine functionalized hydrogels[26] and nanoparticle functionalized surfaces.[44] One of the more striking observations of these studies is that fluorescent actin filaments bind to surface

features and form tight rings or bends that exceed those observed in solution or on NEM-myosin coated coverslips. Tight rings suggest that cationic surface features are capable of disrupting f-actin structure. The energy associated with a bend is directly related to the persistence length, P ~ 17 μm,[45] of the filament. Bends of radius less than P cost actin filaments substantial energy and create perturbations in the equilibrium structure of the filament.[46] Changes in the structure of actin could affect the kinetics of myosin motors and have a toxic impact on cells. In fact, a reduction in myosin V velocity has been observed on actin that is non-specifically attached to NP-decorated surfaces, figure 1.5. A reduction in myosin velocity caused by changes in actin filaments associated with cationic NPs can locally affect transport *in-vivo* where NPs contact actin filaments within the cytoplasm. The consequence would be local defects in myosin dependent transport and the potential accumulation of motor trafficked cargo in the region surrounding NP aggregates.

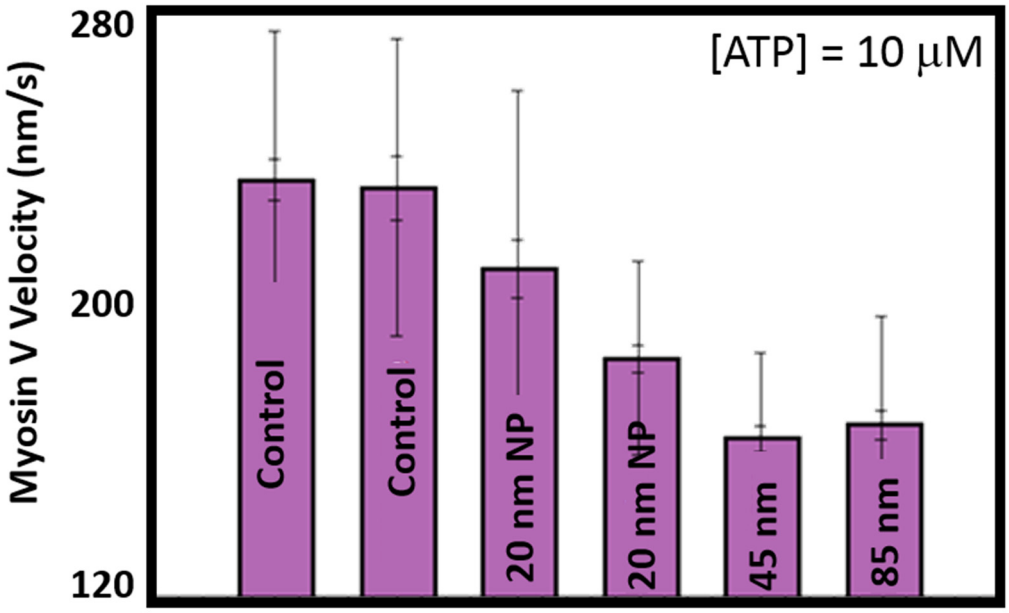

Figure 1.5: Non-Specific binding between positively charged NPs and f-actin reduces Myosin V velocity. The reduction in myosin reaction velocity increases as NP diameter (labeled on bars)

increase. The method of labelling the myosin in the control study between a QD (left) and a fluorophore, rhodamine, (right) does not alter the activity. The nanoparticles were amine functionalized silica spheres.

1.7 Cationic NPs

Cytotoxicity can only occur when NPs penetrate the cell by passing through the membrane in a process known as endocytosis, figure 1.6. Endocytosis can occur through several pathways all of which require NPs to interact with the cell membrane through cooperative (specific or non-specific) interactions with lipids or membrane proteins to curve the membrane around the particle overcoming the elastic bending energy of the membrane and initiating endocytosis, figure 1.6 inset and step 1.[47] Since phospholipids of the membrane are negatively charged, cationic NPs are more likely to generate the necessary curvature, step 2, through electrostatic interactions and enter the cell membrane.[48, 49] Once inside an endocytotic vesicle, proton pumps such as ν-ATPase work to acidify the vesicle to a pH of around 5, step 3. Cationic NPs and polymers such as polylysine act as a "proton sponge" by buffering the pH change created by the proton pumps.[50,51] As a result there is a continued flux of protons, Cl^-, and water across the membrane which increases internal osmotic pressure of the vesicle leading to its eventual rupture and release of contents into the cell, as depicted in step 5.[52] Cationic NPs are considered more toxic than anionic or hydrophobic particles likely because they more readily enter the cell.[53]

Once inside the cell, cationic NPs are associated with toxicity that is cell-type dependent and occurs by lysosomal rupture, intracellular calcium flux, or mitochondrial injury.[50] Cationic polystyrene spheres 60 nm in diameter have been shown to induce mitochondrial damage, steps 6 and 7, in multiple lines of cells through a process which leads to greater than a 90% drop in the available [ATP] after 8 hours.[50] Direct imaging of particles *in*-vivo by fluorescent labelling

or electron microscopy shows that cationic particles associate with mitochondria, induce swelling, and eventually trigger degradation of the mitochondrial lamin, as illustrated in step 7.[50] As summarized in table 1.1, induced mitochondrial damage and subsequent ATP depletion is also observed for other cationic or cation generating particles such as ZnO[51] and Ag.[54] ZnO can dissolve in the acidic environment of the endosome leading to the release of toxic Zn^{+} while Ag NPs are linked to mitochondrial injury.[51,54] Grafting dextran or starch to the surface of silver NPs enables them to more easily enter the cell.[55] A decrease in available [ATP] by as much as 80% due silver NPs toxicity is reported in human cells showing that silver induces metabolic stress.[54]

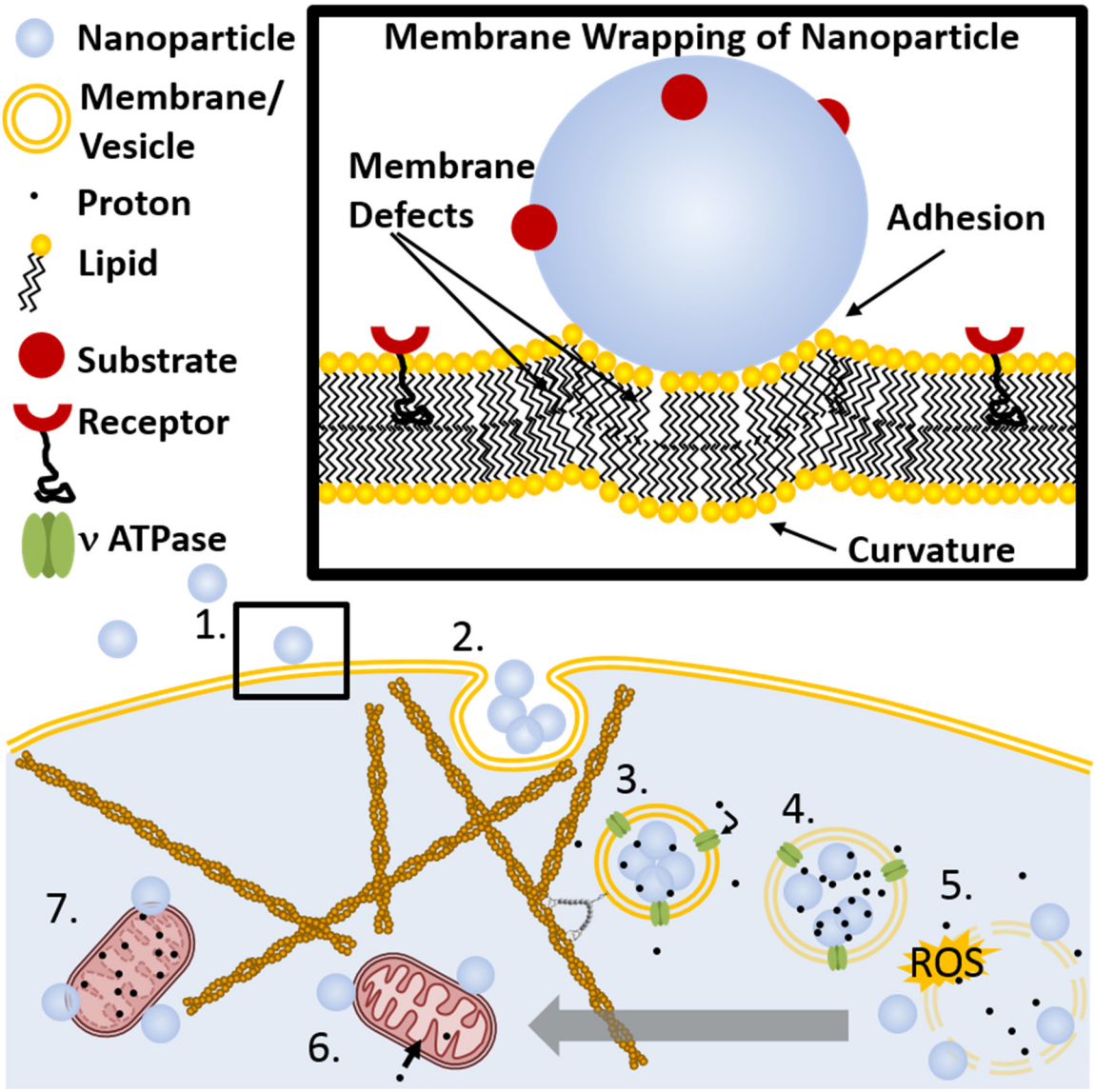

Figure 1.6: NP-membrane interaction potential governs membrane permeation. 1. NPs must first bind to the membrane and adhesive forces between the membrane and the particle must bend the membrane to initialize endocytosis. (Zoom-in inset) 2. Actin, clatharin, and other proteins mediate endocytosis and NPs enter the cytoplasm encapsulated in the endosome. 3. Protein pumps work to create an acidic pH inside the endosomal compartment. 4. In the "proton sponge effect" positively charged particles buffer the pH change leading to accumulation of protons, Cl^-, and water inside the endosome leading to its rupture. 5. The endosome ruptures releasing reactive oxygen species, toxic cations, or toxic cationic particles which can damage the cell. 6. Cations or cationic particles target the mitochondria by an unknown mechanism (grey arrow). 7. Accumulation of cations in or around the mitochondria lead to mitochondrial toxicity and a drop in available [ATP] consequently increasing the [f-actin].

NP type	Toxicity Mechanism
TiO_2/SiO_2	ROS production[25] Membrane Disruption[21] Non-specific interactions with proteins[7]
ZnO	Inflammation[50] ROS production[50] Toxic Cations[50]
Ag	Ag ion inhibition of respiratory enzymes[54] Ag ion mitochondrial injury[54] ROS production[54]
Au	Non-toxic[53,56]
Anionic	ROS production[21,53]
CdSe	Cadmium Hepatotoxicity[57,58] Mitochondrial injury[57,58]
Cationic	Membrane Damage[50] Endosomal compartment Bursting[50] Mitochondrial Toxicity[50]

Table 1.1: Common NPs and observed toxicity mechanism.

1.8 A need for real time tracking of cytotoxicity

Cell damage and the mechanism of damage due to NP exposure can be accurately assessed by measuring the concentration of ATP, monitoring enzymes associated with membrane leakage such as lactose dehydrogenase, or measuring ROS concentration.[59] Because these measurements require staining or lysing cell cultures, each experiment captures only a single predetermined time point. Dissecting the mechanism of cytotoxicity of NPs requires real time imaging of treated cells with the capability of measuring factors like ROS and ATP concentrations within the cell. Progress is being made at developing injectable probes such as a [ATP] sensitive FRET sensor capable of discerning real time ATP availability in a cell.[60] Cellular viscoelasticity can be measured by the atomic force microscope, AFM, to directly probe the structure and dynamics of the membrane, cytoplasm, or nucleus at potentially nm scale lateral resolution.[61]

1.9 Correlating cellular metabolism with viscoelasticity

The development of the AFM as a diagnostic tool shows promise in distinguishing between cancerous and healthy cells by their elastic properties.[62,63] Elastic measurements by AFM are accomplished by poking cells with a cantilever at a fixed velocity and measuring the cantilever deflection, figure 1.7. The force exerted to bend the cantilever, F, is plotted against the cantilever position as the tip is brought into contact with the cell, red curve, and then retracted, green curve in figure 1.7. The curve generated by the approach, red, is fit to the Hertz equation (equation 1.3) to determine the elastic modulus,[64]

$$F = \frac{4}{3} * \frac{E}{1-\nu^2}\sqrt{R} * (\delta - \delta_o)^{3/2} \quad . \qquad (1.3)$$

The force, F = kx , is determined by Hooke's law using the spring constant, k, and deflection, x, of the cantilever. The radius of the indenter, R, and the Poisson's ratio of the cell, $\nu = 0.37 \pm 0.03$[65] are known quantities, and the position of the cantilever, δ, is normalized by the contact point with the cell, δ_o. In equation 1.3, the fitting parameters are the zero indentation depth, δ_o, and the elastic modulus, E.[61]

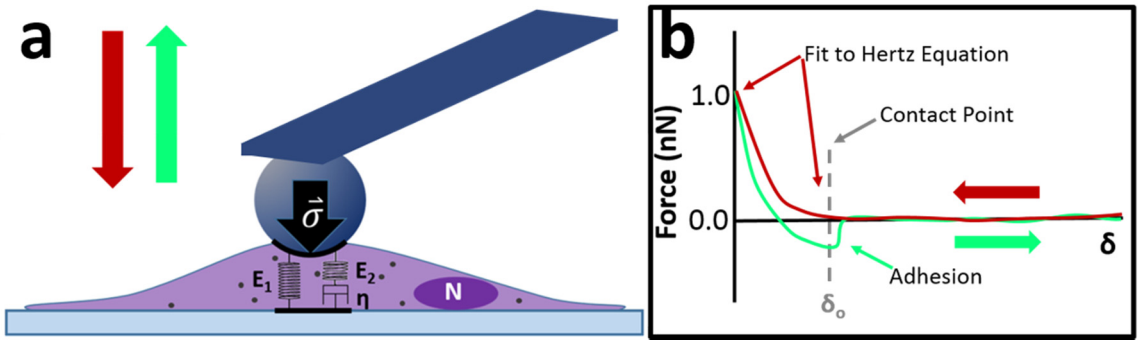

Figure 1.7: Atomic force microscopy to measure the viscoelasticity of the cytoplasm. **a.** Cellular viscoelasticity is probed by pressing on the cell with a stress, $\vec{\sigma}$, leading to deflection of the cantilever, x, that determines the force, F, exerted on the cantilever by the cell through the spring constant of the cantilever. Cells have been shown to exhibit linear viscoelasticity consistent with the standard-linear solid model (Zener model) shown inside the cell. The

primary parameters are the low frequency elasticity, E_1, the high frequency elasticity, E_2, and the viscosity, h. **b**. Typical shape of an indentation curve by an atomic force microscope on a living cell. Force is plotted against cantilever height, and the shape of the contact curve (section of the curve to the left of the dotted line) is fit to the Hertz equation to determine the complex elastic modulus. The retraction curve shown in green typically exhibits some adhesion (arrow) between the cell and the cantilever that results in negative deflection of the cantilever and thus the evolution of negative force during retraction.

The elastic modulus, E, represents the magnitude of the complex modulus, $E = |E_{elastic} + iE_{Viscous}|$ and is a rate-dependent combination of elastic and viscous properties in the cell. For cells, E ranges from 0.1 – 60 kPa[66] and healthy cells can be phenotyped by elastic modulus.[69] Breast and lung cancer cells are softer than normal cells of the same phenotype by approximately 4-fold, while carcinoma cells of the pancreas exhibit the same modulus as healthy cells.[62,63] Because the magnitude of E depends on the rate of indentation, $(d\delta/dt)$,[67,68] direct comparison between experiments using different indentation rates give different modulus values, highlighting the need to understand both the viscous and elastic components of biological materal in a self-consistent fashion. Efforts to determine both the viscous, $E_{viscous}$, and elastic, $E_{elastic}$, moduli independently by AFM are realized by the development of creep tests.[69] Creep tests have demonstrated that there are significant differences in both the viscous and elastic moduli between cell phenotypes enabling identification of cell type by elastic properties.[70]

The modulus of a population of cells typically has a variance around the magnitude of the average modulus, which implies that ongoing processes such as metabolism vary between individual cells enough to create significant viscoelastic differences. Cancer cells are measurably softer than normal cells, which is may be due to their increased metabolic rate, and the metastatic transformation of carcinoma cells correlates with a reduction in viscoelasitcity.[71] The viscoelasticity of cells changes with the expression of filamentous proteins, in particular f-actin.[72] For example, an increase in f-actin concentration by treatment with jasplakinolide causes a

150% increase in $E_{elastic}$, while depolymerization of f-actin by latrunculin yields a 5-fold decrease in $E_{elastic}$ and a 5-fold decrease in $E_{viscous}$.[74] Conversely, increases or decreases in microtubule concentration insignificantly change the viscoelastic modulus. [74]

Creep tests have also shown that the Zener model for viscoelasticity (drawn inside the cell in figure 1.7a) is an accurate model of cytoplasmic viscoelastic behavior.[69,70,73,74] Since actin is the primary component responsible for cellular viscoelasticity it follows that the components of the Zener model, E_1, E_2, and η, are directly related to the density of actin filaments and associating proteins in the cytoplasm. Figure 1.8 illustrates the correlation between viscoelastic properties of the cytoplasm and cytoskeletal f-actin. The low frequency elastic modulus, E_1, measures the entropic resistance of actin filaments to compression and is therefore a measure of [f-actin]. The high frequency elastic component is sensitive to cross links in the actin network, generally caused by molecular motors or other actin associated proteins that detach under load during low frequency elastic measurements. And the viscosity of the cell, η, measures the rate at which those detachments occur.[75,76] Since AFM is sensitive to the expression of f-actin in a cell, local metabolic processes which affect f-actin degree of polymerization or myosin-motor function[77] should be detectable as local viscoelastic perturbations.

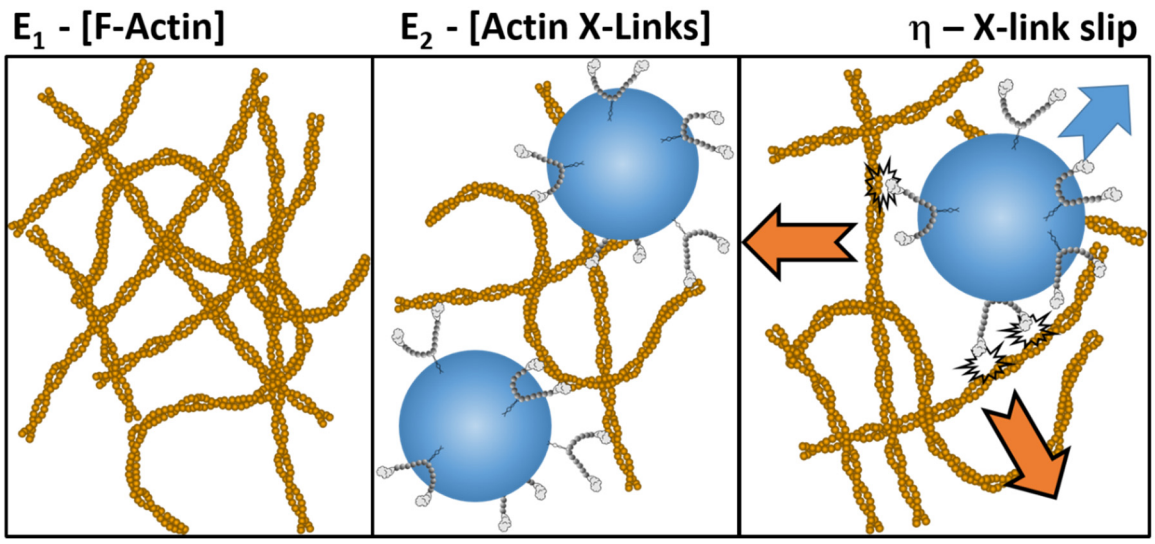

Figure 1.8: Cytoskeletal components probed by the various terms in the standard-linear solid model. The low frequency elastic component, E_1, is sensitive to the local density of actin filaments. The high frequency elastic component, E_2, is sensitive to the molecular motor or other dynamic cross linkers of f-actin in the cytoskeleton. The viscosity, h, is derived from the slippage rate of the cross links and cytoskeletal filaments in response to stress.

F-actin concentration and NP toxicity are directly linked through [ATP] within the cytoplasm. As previously mentioned, NP-induced mitochondrial injury can reversibly lower the ATP concentration in a cell by more than 80% in a few hours. Figure 1.9 shows how the concentration of f-actin within a cell is regulated by the available ATP through the selective sequestering of ATP-G-actin by $T\beta_4$ which prevents actin polymerization. When [ATP]/[ADP] decreases, the [G-actin] available for polymerization increases because $T\beta_4$ can no longer associate with G-actin which shifts the actin equilibrium towards increased [f-actin].[78] In this way, metabolic stress caused by cationic NPs decreases the available ATP in cells, leading to a measurable increase in cell viscoelastic modulus due to increased actin polymerization. Furthermore, cross-linking of the cytoskeleton in smooth-muscle by myosin during *rigor-mortis* is linked to a 20-40 fold increase in cell elastic modulus.[79] Thus, molecular motors respond to reductions in [ATP] by cellular stiffening either analogous rigor mortis in extreme cases or by viscosity increases associated with molecular-motor slow down. As discussed previously, in the

absence of ATP, molecular motors strongly associate with their track, and thus cytoskeletal cross-linking is directly measured as increased elastic modulus. Similarly, cancer cells are known to be supermetabolic, maintaining a high level of aerobic metabolism through the Warburg effect that supports the demand of rapid proliferation for tumorigenesis.[80,81] The high metabolic rate of cancer may be directly linked to the comparative softness of carcinoma cells.

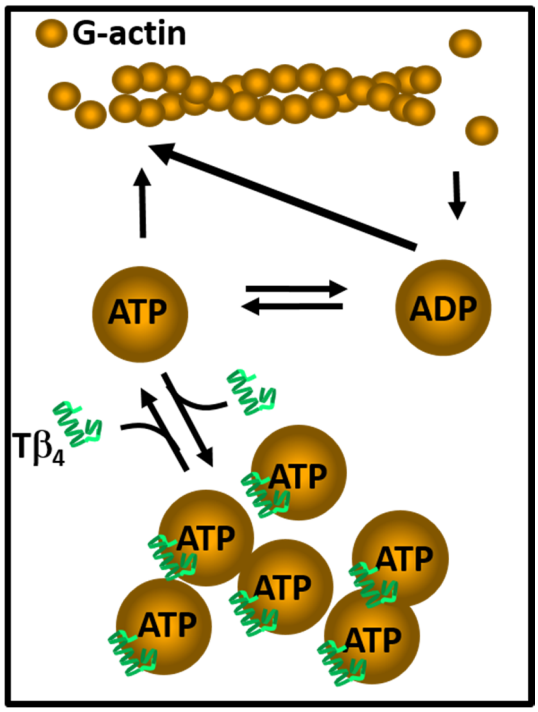

Figure 1.9: [ATP] regulates the [f-actin] in the cytoplasm through the protein Tβ4. G-actin (circles) binds and hydrolyzes ATP during the polymerization process. The amount of available G-actin and the amount of f-actin in the cell create a dynamic equilibrium that sets the relative concentration of f-actin in the cell. Tb_4 binds exclusively to ATP-G-actin removing it from the equilibrium leading to depolymerization of f-actin to maintain the G-f actin dynamic equilibrium. In the case of ATP depletion, ATP G-actin becomes highly depleted and thus $T\beta_4$ unbinds from the majority of G-actin in the cell leading to an increase in the G-actin pool available for polymerization. The result is an increase in [f-actin] directly associated with metabolic stress, i.e. decreased [ATP].[78]

1.10 Conclusion

This chapter outlines the mechanism of nanoparticle toxicology with an emphasis on the role of cationic nanoparticles. Specific interactions between particles and biomolecules are generally desirable because molecules can be directly targeted even in the presence of contaminating background. Specific labelling defines many drugs and fluorescent probes. Non-specific interactions are the primary source of undesired cytotoxicity because NPs will interact non-specifically with all molecules. Electrostatic potential is one of the primary determinants of cytotoxicity, and cationic particles are found to be more toxic than anionic particles. The high toxicity of cationic particles is attributed to the ease with which cations strongly interact with the cell membrane and promote endosome escape by the "proton sponge effect". Once inside a cell, cationic NP toxicity occurs by lysosomal compartment rupture, Ca^{2+} flux, and mitochondrial injury in a cell phenotype dependent manner. NPs reduce the activity of enzymes such as lysozyme, L-lactate dehydrogenase, and Myosin V *in-vitro* in a fashion which depends on NP size. Analyzing enzyme activity through the Michaelis-Menten kinetic relationship distinguishes between structural changes which effect enzyme-substrate affinity and enzyme catalytic efficiency. The kinetics of molecular motors, such as myosin, are carefully regulated by their track through catalysis of byproduct release and the duty-ratio of the motor. Since molecular motors lend themselves to single molecule kinetic characterization, high resolution tracking of molecular motors may provide a key to understanding the mechanism of cellular injury by NP toxicity with sub-cellular spatial resolution in real time because myosin kinetics directly respond to changes in [ATP] and [Ca^{2+}]. Local cell viscoelasticity is also linked to metabolism through the available [ATP] and molecular motor dynamics. [F-actin] is the most significant contributor to cell elasticity and a decrease in available [ATP] associated with metabolic stress and mitochondrial injury leads to an increase in [f-actin] through the release of

G-actin for polymerization by $T\beta_4$. The viscoelasticity is closely linked to actin-motor dynamics and therefore myosin duty-ratio which dramatically increases, analogous to *rigor-mortis,* as myosin velocity is reduced by ATP depletion leading to filament cross linking. Thus the atomic force microscope may provide a crucial tool for measuring local metabolic changes in cells non-invasively with nm lateral resolution.

1.11 References

1. Che G, Lakshimi BB, Fisher ER, Martin CR, Carbon nanotube membranes for electrochemical energy storage and production, *Nature,* 393, **1998**, 246-349.
2. Peer D, Karp JM, Hong S, Farokhzad OC, Margalit R, Langer R, Nanocarriers as an emerging platform for cancer therapy, *Nature Nanotechnology*, 2, **2007**, 751-760.
3. Kocbek P, Tesac K, Kreft ME, Kristl J, Toxicological Aspects of Long-Term Treatment of Keratinocytes with ZnO and TiO_2 Nanoparticles, *Small*, 6, 17, **2010**, 1908-1917.
4. Podsiadlo P, Paternel S, Rouillard J-M, Zhang Z, Lee J, Lee J-W, Gulari E, Kotov NA, Layer-by-layer Assembly of Nacre-like Nanostructured Composites with Antimicrobial Properties, *Langmuir*, **2005**, 21, 25, 11915-11921.
5. Mura S, Nicolas J, Couvreur P, Stimuli-responsive nanocarriers for drug delivery, *Nature Materials*, 12, **2013**, 991-1003.
6. Sun S, Murray CB, Weller D, Folds L, Moser A, Monodisperse FePt Nanoparticles and Ferromagnetic FePt Nanocrystal Superlattices, *Science*, 287, **2000**, 1989-1992.
7. Vertegel AA, Siegel RW, Dordick JS, Silica nanoparticle size influences the structure and enzymatic activity of adsorbed lysozyme. *Lngmuir*, 20, **2004**, 6800-6807.
8. Sharma V, Anderson D, Dhawan A, Zinc oxide nanoparticles induce oxidative DNA damage and ROS-triggered mitochondria mediated apoptosis in human liver cells (HepG2), *Apoptosis*, 17, **2012**, 852-870.
9. Sayes CM, Wahi R, Kurian PA, Liu Y, West JL, Ausman KD, Warheit DB, Colvin VL, Correlating Nanoscale Titania Structure with Toxicity: A Cytotoxicity and Inflammatory Response Study with Human Dermal Fibroblasts and Human Lung Epithelial Cells, *Toxicological Sciences*, 91, 1, **2006**, 174-185.
10. Trouiller B, Reliene R, Westbrook A, Solaimani P, Schiestl RH, Titanium Dioxide Nanoparticles Induce DNA Damage and Genetic Instability *In vivo* in Mice, *Journal of Cancer Research*, 15, 69, **2009**, 8784-8789.
11. Nel AE, Madler L. Velegol D, Xia T, Hoek EM, Somasundaran P, Klaessig F, Castranova V, Thompson M, Understanding biophysiochemical interactions at the nano-bio interface, *Nature Materials*, 8 **2009**, 543-557.
12. Lundqvist M, Stigler J, Elia G, Lynch I, Gedervall T, Dawson KA, Nanoparticle size and surface properties determine the protein corona with possible implications for biological impacts, *PNAS,* 105, **2008**, 14265-14270.
13. Pan H, Qin M, Meng W, Cao Y, Wang W, How Do Proteins Unfold upon Adsorption on Nanoparticle Surfaces? *Langmuir*, 28, 35, **2012**, 12779-12787.
14. Steuker O, Ortega VA, Goss GG, Stepanova M, Understanding Interactions of Functionalized Nanoparticles with Proteins: A Case Study on Lactate Dehydrogenase, *Small*, 10, 10, **2014**, 2006-2021.

15. Levard C, Hotze EM, Colman BP. Dale AL, Truong L, Yang XY, Bone AJ, Brown GE Jr, Tanguay RL, DiGiulio RT, Bernhardt ES, Meyer JN, Wiesner MR, Lowry GV, Sulfidation of Silver Nanoparticles: Natural Antidote to Their Toxicity, *Environmental Science and Technology*, 47, **2013**, 13440-13448.
16. Fischer E, Einfluss der Configuration auf die Wirkung der Enzyme, *Ber. Deutsch chem. Gesell.* 27 **1894** 1255-1256.
17. Chen B, Piletsky S, Turner APF, Molecular recognition: Design of "keys", *Combinatorial Chemistry and High Throughput Screening*, 5, 6, **2002**, 409-427.
18. Green M, Avidin, *Advances in protein chemistry* 29, **1975**, 85-133.
19. Resch-Genger U, Grabolle M, Cavaliere-Jaricot S, Nitschke R, Nann T, Quantum dots versus organic dyes as fluorescent labels, *Nature Methods*, 5, 9, **2008**, 763-775.
20. Warshaw DM, Kennedy GG, Work SS, Krementsova EB, Beck S, Trybus KM, Differential labeling of myosin V heads with quantum dots allows direct visualization of hand-over-hand processivity, *Biophysical Journal*, 88, **2005**, L30-L32.
21. Shi J, Votruba AR, Farokhzad OC, Langer R, Nanotechnology in Drug Delivery and Tissue Engineering: From Discovery to Applications, *Nano Letters*, 10, **2010**, 3223-3230.
22. Medina C, Santos-Matinex MJ, Radomski A, Corrigan OI, Radomski MW, Nanoparticles: pharmacological and toxicological significance, *British Journal of Pharmacology*, 150, 5, **2007**, 552-558.
23. Min Y, Akbulut M, Kristianen K, Golan Y, and Israelachvili, The role of interparticle and external forces in nanoparticle assembly, *Nature Materials*, 7, **2008**, 527-538.
24. Park E-J, Park K, Oxidative stress and pro-inflammatory responses induced by silica nanoparticles in vivo and in vitro, *Toxicology Letters*, 184, 1, **2009**, 18-25.
25. Yu BP, Cellular Defenses Against Damage From Reactive Oxygen Species, *Physiological Reviews*, 74, 1, **1994**, 139-162.
26. Park J-H, Sun Y, Goldman YE, Composto RJ, Self-assembled charged hydrogels control the alignment of filamentous actin, *Soft Matter*, 6, **2010**, 915-921.
27. English BP, Min W, van Oijen AM, Lee KT, Luo G, Sun H, Cherayil BJ, Kou SC, Xie S, Ever-fluctuating single enzyme molecules: Michaelis-Menten equation revisited, *Nature Chemical Biology*, 2, 2, **2006**, 87-94
28. Michaelis L, Menten ML, Kinetics of invertase action, *Biochemi. Z.*, 49, **1913**, 333-369.
29. (a) M. Preller and D.J. Manstein, 4.8 Myosin Motors: Structural Aspects and Functionality, Comprehensive Biophysics, Edward H. Egelman, Elsevier, Amsterdam, **2012**, Pages 118-150. (b) Goldman YE, Ostap EM, 4.9 Myosin Motors: Kinetics of Myosin, Comprehensive Biophysics, Edward H. Egelman, Elsevier, Amsterdam, **2012,** 151-169.
30. De La Cruz EM, Ostap EM, Relating biochemisty and function in the myosin superfamily, *Current Opinion in Cell Biology*, 16, 1, **2004**, 61-67.
31. Howard J: *Mechanics of Motor Proteins and the Cytoskeleton*. Sunderland, MA: Sinauer Assoc; **2001**.
32. Marston SB, Taylor EW, Comparison of the myosin and actomyosin ATPase mechanisms of the four types of vertebrate muscles, *Journal of Molecular Biology*, 139. **1980**, 573-600.
33. Dantzig JA, Goldman YE, Millar NC, Lacktis J, Homsher E, Reversal of the cross-bridge force-generating transition by photogeneration of phosphate in rabbit psoas muscle fibres, *Journal of Physiology*, 451, **1992**, 247-278.
34. (a) De La Cruz EM, Wells AL, Rosenfeld SS, Ostap EM, Sweeney HL, The kinetic mechanism of myosin V, *PNAS*, 96, **1999**, 13726-13731. (b) De La Cruz EM, Well AL,

Sweeney HL, Ostap EM, Actin and light chain isoform dependence of myosin V Kinetics, *Biochemistry*, 39, **2000**, 14196-14202.
35. Reubold TF, Eschenburg S, Becker A, Kull FD, Manstein DJ, A structural model for actin-induced nucleotide release in myosin, *Nature Structural Biology*¸**2003**, 10, 10, 826-830.
36. Yildiz A, Forkey JN, McKinney SA, Ha T, Goldman YE, Selvin PR, Myosin V walks hand-over-hand: single fluorphore imaging with 1.5 nm localization, *Science*, 300, **2003**, 2061-2065.
37. Ruhnow F, Zwicker D, Diez S, Tracking single particles and elongated filaments with nanometer precision, *Biophysical Journal*, **2011**, 100, 11, 2820-2828.
38. Forkey JN, Quinlan ME, Shaw MA, Corrie JE, Goldman YE, Three-dimensional structural dynamics of myosin V by single-molecule fluorescence polarization, *Nature*, 422 **2003**, 399-404.
39. Pinaud F, Clarke S, Sittner A, Dahan M, Probing cellular events, one quantum dot at a time, *Nature methods*, 7, **2010**, 275-285.
40. Ali MY, Kennedy GG, Safer D, Trybus KM, Sweeney HL, Warshaw DM, Myosin Va and myosin VI coordinate their steps while engaged in an in vitro tug of war during cargo transport, *PNAS*, 108, 34, **2011**, E535-E541.
41. Michaelet X, Pinaud FF, Bentolila LA, Tsay JM, Doose S, Li JJ, Sundaresan G, Wu AM, Gambhir SS, Weiss S, Quantum Dots for Live Cells, in Vivo Imaging, and Diagnostics, *Science*, 28, 307, **2005**, 538-544.
42. Meeusen RL, Cande WZ, N-ethylmalemide-modified heavy meromyosin. A probe for actomyosin interactions, *JCB*, 82, 1, **1979**, 57-65.
43. Selvin PR, Ha T, Single-molecule techniques: a laboratory manual, (Cold Spring Harbor Laboratory Press, 2008).
44. Caporizzo MA, Sun Y, Goldman YE, Composto RJ, Nanoscale topography mediates the adhesion of F-actin, *Langmuir,* 28, 33, **2012**, 12216-12224.
45. Vikhorev PG, Vikhoreva NN, Mansson A, Bending Flexibility of Actin Filaments during Motor-induced Sliding, *Biophysical Journal*, 95, **2008**, 5809-5819.
46. Nelson P, *Biological Physics: Energy, Information, Life;* W.H. Freeman and Co.: New York, **2008**; pp 341-385.
47. Decuzzi P, Ferarri M, The role of specific and non-specific interactions in receptor-mediated endocytosis of nanoparticles, *Biomaterials*, 28, **2007**,2915-2922.
48. Fleck CC, Netz RR, Electrostatic colloid-membrane binding, *Europhysics Letters*, 67, **2004**, 314-320.
49. Jiang W, Kim BS, Rutka JT, Chan WCW, Nanoparticle-mediated cellular response is size-dependent, *Nature Nanotechnology*, 3, **2008**, 145- 150.
50. Xia T, Kovochich M, Liong M, Zink JJ, Nel AE, Cationic polystyrene nanosphere toxicity depends on cell-specific endocytotic and mitochondrial injury pathways, *ACSNano*, 2, **2008**, 85-96.
51. Xia T, Kovochich M, Liong M, Madler L, Gilbert B, Shi H, Yeh JI, Zink JI, Nel AE, Comparison of the Mechanism of Toxicity of Zinc Oxide and Cerium Oxide Nanoparticles Based on Dissolution and Oxidative Stress Properties, *ACSNano*, 2, 10 , **2008**, 2121-2134.
52. Varkouhi AK, Scholte M, Storm G, Haisma HJ, Endosomal escape pathways for delivery of biologicals, *Journal of Controlled Release*, 151, **2011**, 220-228.
53. Goodman CM, McCusker CD, Yilmaz T, Rotello VM, Toxicity of gold nanoparticles functionalized with cationic and anionic side chains. *Bioconjugate Chemistry*, 15, **2004**, 897-900.

54. AshaRani PV, Mun GLK, Hande MP, Valiyaveettil S, Cytotoxicity and Genotoxicity of Silver Nanopaticles in Human Cells, *ACS Nano*, 3, 2, **2009**, 279-290.
55. Coll Ferrer MC, Sobolewski P, Composto RJ, Eckmann DM, *Journal of Nanotechnology in Engineering and Medicine,* 4, 1, **2013**, 011002.
56. Chithrani BD, Ghanzani AA, Chan WCW, Determining the Size and Shape Dependence of Gold Nanoparticle Uptake into Mamallian Cells, *Nano Letters*, **2006**, 6,4, 667-668.
57. Derfus AM, Chan WCW, Bhatia SN, Probing the Cytotoxicity of Semiconductor Quantum Dots, *Nano Letters,* **2004**, 4, 1, 11-18.
58. Rikans LE, Yamano T, Mechanisms of cadmium-mediated acute hepatotoxicity, *Journal of Biochemical and Molecular Toxicology*, **2000**, 14, 2, 110-117
59. Kepp O, Galluzzi L, Lipinski M, Yuan J, Kroemer G, Cell Death assays for drug discovery, *Nature Reviews Drug Discovery*, 10, **2011**, 221-237.
60. Imamura H, Nhat KPH, Togawa H, Saito K, Lino R, Kato-Yamada Y, Nagai T, Noji H, Visualization of ATP levels inside single living cells with fluorescence resonance energy transfer-based genetically encoded indicators, *PNAS,* **2009**, 106, 37, 15651-15656.
61. Radamacher M, Studying the mechanics of cellular process, by atomic force microscopy, in Cell Mechanics, Y-I Wang and DE discher, Editors. **2007**, Academic Press, 347-372.
62. Cross SE, Jin YS, Rao J, Gimzewski JK, Nanomechanical analysis of cells from cancer patients, *Nature Nanotechnology*, 2, **2007**, 780-783.
63. Cross SE, Jin YS, Tondre J, Wong R, Rao JY, Gimzewski JK, AFM-based analysis of human metastatic cancer cells, *Nanotechnology*, 19, **2008**, 384003.
64. Hertz H, On the contact of elastic solids, *J. reine angew. Math*, 92, **1881**, 156-171.
65. Shin D, Athanasiou K, Cytoindentation for obtaining cell biomechanical properties, *Journal of Orthopaedic Research*, 17, **1999**, 880-890.
66. Fischer RS, Myers KA, Gardel ML, Waterman CM, Stiffness-controlled three-dimensional extracellular matrices for high-resolution imaging of cell behavior, Nature Protocols, 7, 11, **2012**, 2056-2064.
67. Nawas S, Sanchez P, Bodensiek K, Li S, Simons M, Schaap IAT, Cell Visco-elasticity Measured with AFM and Optical Trapping at Sub-Micrometer Deformations, *PLOS One*, 7,9, **2012**, e45297.
68. Rebelo LM, de Sousa JS, Filho JM, Radmacher M, Comparison of the viscoelastic properties of cells from different kidney cancer phenotypes measured with atomic force microscopy. *Nanotechnology*, 24, **2013**, 055102.
69. Darling EM, Topel M, Zauscher S, Vail TP, Guilak F, Viscoelastic properties of human mesenchymally-derived step cells and primary osteoblasts, chondrocytes, and adipocytes, *Journal of Biomechanics*, 41, **2008**, 454-464.
70. Darling EM, Zauscher S, Block JA, Guilak F, A Thin-Layer Model for Viscoelastic, Stress-Relaxation Testing of Cells Using Atomic Force Microscopy: Do Cell Properties Reflect Metastatic Potential?, *Biophysical Journal*, 92, **2007**, 1784-1791.
71. Fritsch A, Hockel M, Kiessling T, Knetu KD, Wetzel F, Zink M, Kas JA, Are biomechanical changes necessary for tumor progression? *Nature Physics*, 6, **2010**, 730-733.
72. Rotsch C, Radmacher M, Drug-Induced Changes of Cytoskeletal Structure and Mecahanics in Fibroblasts: An Atomic Force Microscopy Study, *Biophysical Journal*, 78, **2000**, 520-535.
73. Ketene AN, Schmelz EM, Roberts PC Agah M, The effects of cancer progression on the viscoelasticity of ovarian cell cytoskeleton structures, *Nanotechnology*, 8, **2012**, 83-102.

74. Ketene AN, Roberts PC, Shea AA, Schmelz EM, Agah M, Actin filaments play a primary role for structural integrity and viscoelastic response in cells, *Integrative Biology*, 4, **2012**, 540-549.
75. Caporizzo MA, Roco CM, Coll-Ferrer CM, Eckmann DM, Composto RJ, The Atomic Force Microscope as a Diagnostic tool for Correlating Cellular Viscoelasticity with Metabolism, *in press.*
76. Fung Y C **1993** Biomechanics: Mechanical Properties of Living Tissues 2nd edn (New York: Springer).
77. Martens JC, Radmacher M, Softening of the actin cytoskeleton by inhibition of myosin II, *European Journal of Physiology*, 465, **2008**, 95-100.
78. Atkinson SJ, Hosford MA, Molitoris BA, Mechanism of Actin Polymerization in Cellular ATP Depletion, *Journal of Biological Chemistry*, 279, **2004**, 5194-5199.
79. Bate-Smith EC, Bendall JR, Rigor mortis and adenosinetriphosphate, *J. Physiol.*, 106, **1947**, 177-185.
80. Warburg O, On the origin of cancer cells, *Science*, 123, **1956**, 309-314.
81. Cairns RA, Harris IS, Mak TW, Regulation of cancer cell metabolism, *Nature Reviews Cancer,* 11, **2011**, 85-95.

Chapter 2: Experimental Methods

2.0 Introduction

Chapter 2 describes the methods of preparation and characterization of NP-SAA composite films and discusses the fundamentals underlying NP-SAA film interactions with biomolecules. Namely, details of film scattering, quartz-crystal microbalance, and atomic force microscope analysis of SAA and NP-SAA composites are discussed. Since the surface morphology dictates the attachment of anionic f-actin, a section is devoted to the novel surface topography that results from controlling nanoparticle embedding and sinking into a copolymer film. A derivation of the bending energy model is provided which quantifies the interaction of f-actin with the NP-SAA composite films based on their roughness in chapter 4. The electrostatic interaction between f-actin and these nano-textured surfaces is described in detail because the strength of f-actin attachment directly determines the velocity of myosin motors presented in chapter 5. Finally, methods for preparation of dextran-lysozyme hydrogels and poly-acrylamide gel surfaces are presented with the biological assays used to complement the viscoelastic studies of cells by variable indentation-rate rheometric analysis by Laplace transform in chapter 6. The aim of this section is to provide future researchers with a detailed discussion of the methods and experimental design to facilitate further studies in this area.

2.1 Amine functionalization of NPs

Silica nanoparticles were functionalized with amine groups to allow for their grafting into a copolymer film and attraction for f-actin. Anhydrous dimethyl sulfoxide (DMSO), ethanol (200 proof), toluene, reagent grade (3-aminopropyl)triethoxysilane (APTES), *N*-(3-Dimethylaminopropyl)-*N*'-ethylcarbodiimide hydrochloride (EDC >99%), and N-

hydroxysuccinimide (NHS >98%) were purchased from Sigma-Aldrich, USA. Poly(styrene-random-tert butyl acrylate) (StBA), 37 mol% tBA and weight average molecular weight of XXXX, was purchased from Polymer Source Inc. and used as received. Silica nanoparticles 30 wt% in isopropanol (IPA-ST-series) were obtained from Nissan Chemical, USA with average diameters of 12 nm, 20 nm 45 nm, and 85 nm as verified by dynamic light scattering.

Amine functionalized SiO_2 NPs are synthesized from colloidal silica particles obtained from Nissan Chemical (IPA-ST series). NPs are solvent exchanged from isopropanol to anhydrous dimethyl sulfoxide, DMSO, by iterative pelleting and dispersion. After 3x redispersion in DMSO, NPs are heated to 70 ^{o}C in a water bath under a flow of dry N_2. 5 volume percent 3-aminopropyltriethoxysilane, APTES, is added to the NP-DMSO solution and reacted for 8 h. The DMSO contains roughly 10 wt% SiO_2 NPs during functionalization. Following the 8 h grafting, the solution is cooled, and sonicated for 24 h to disperse NPs. Solvent exchanged into EtOH is then repeated 3x and NP solutions are stored in a desiccator until use.[1]

2.2 Polymer film preparation

To create atomically smooth optically transparent samples as fully characterized in chapter 4, freshly cleaved grade V-1 muscovite mica (SPI supplies) is attached to a cleaned No. 0 glass coverslip by high temperature optical adhesive (Opti-tec OPT 5001), refractive index 1.54, obtained from Intertronix, Inc.. After curing the epoxy at 65 ^{o}C for 1 h, the attached mica is freshly cleaved with tape. Poly(styrene-random-tert-butyl acrylate), StBA, is then dissolved in toluene (Sigma Aldrich) at concentrations ranging from 0.5 wt% to 5 wt%,. These solutions are spin cast on the freshly cleaved mica, yielding films from 39 ± 2 nm to 286 ± 8 nm thick as measured by ellipsometry.

To correlate the surface properties (e.g., roughness, wetting) with myosin V velocity on NP decorated surfaces (chapters 3 and 5), StBA films are spin cast onto glass coverslips (No. 1) and silicon wafers with 1 wt% StBA in toluene at 2000 RPM. Initial film thickness under these conditions is 100 nm measured by ellipsometry. Silicon and glass substrates are cleaned in piranha solution at 80^{o}C for 45 min and washed with deionized unfiltered (DIUF) water and dried under N_2. StBA films are converted to SAA by annealing for 15 h under N_2 gas at temperatures ranging from 135^{o}C to 200^{o}C which partially converts StBA to SAA. The film thickness is then recorded again after the anneal with ellipsometry and the thickness change is directly related to the fraction of tBA converted to AA by equation 3.1.

Covalent linking of the particles to the SAA films is accomplished by activating the hydroxide moieties on the substrate by incubation in an aqueous solution of 0.1 M 1-ethyl-3-(-3-dimethylaminopropyl)carbodiimide, EDC, and 0.2 M N-hydroxysuccinimide, NHS, (Sigma Aldrich) for one hour. NP solutions are sonicated for 15min and then cooled to room temperature before activated substrates are immersed in NP solutions face down to prevent sedimenting aggregates from sticking to the surface. To control surface roughness and NP morphology, substrates are incubated in NP solutions for times ranging from 5 minutes to 9 hours. cf. chapter 3. After incubation, substrates were rinsed thoroughly with ethanol, then immersed in an ethanol bath and sonicated for 5 min to remove any ungrafted particles from the surface. Films were rinsed again with ethanol and dried under a flow of N_2 before atomic force microscopy was used to characterize surface roughness in air.

2.3 Characterization of SAA films

The copolymer composition directly impacts the attachment and sinking of the amine functionalized nanoparticles. The fraction of conversion of tBA to AA was determined by

measuring the film thickness change before and after thermal annealing using ellipsometry as shown in equation 3.1**.** A Nicolet Nexus 860 attenuated total Internal reflection Fourier transform infrared spectrometer (ATR-FTIR) is used to determine the chemical composition of the films before and after annealing (figure 3.2).

The average optical transmission (transparency) in the visible spectrum is measured with a Cary 5000 UV-Vis-NIR spectrometer from 300 nm to 800 nm and shown in figure 3.7a. SAA film transparency correlates with the NP morphology. As feature size or NP aggregation increases, film transparency is expected to decrease due to Rayleigh scattering. For small scatterers, d << λ, the Rayleigh scattering intensity strongly depends on feature size, d. Equation 2.1 shows that the relative scattering intensity scales as d^6/λ^4.[2]

$$\frac{I}{I_o} = \frac{1}{2R^2}\left[\frac{n^2-1}{n^2+2}\right]^2\left[\frac{2\pi}{\lambda}\right]^4\left[\frac{d}{2}\right]^6 \qquad (2.1)$$

R and n are the separation between features and particle refractive index, respectively. Since the aggregate size can be relatively large and on the order of λ in our studies, equation 2.1 cannot reliably be correlated with aggregate size and more sophisticated modeling, such as Mie theory[3], is needed. Because a detailed scattering study is beyond the scope of chapter 3, the average scattering intensity or absorbance (I/I_o) is used to qualitatively correlate film transparency with the NP morphology.

NP attachment kinetics is measured by mass change using a Q-Sense E4 quartz crystal microbalance with dissipation monitoring and fitting the 5th overtone due to the viscoelasticity of the swollen SAA. As NPs attach to the copolymer film on the oscillating crystal, the harmonic frequency decreases in a way which can be related to the mass change by the Sauerbrey

approximation (equation 2.2).[4] The mass is given in units of ng/cm^2 where Δf is the harmonic frequency change of the quartz crystal in Hz and is the overtone number.

$$\Delta m = -\frac{17.7(\Delta f)}{\alpha} \qquad (2.2)$$

The surface topography of dry NP-SAA composite films is imaged with a Pico-Plus atomic force miscroscope (AFM), Agilent Technologies. Super sharp AFM tips of diameter < 2 nm and spring constant 15 N/m, are used to optimize resolution of NP surfaces (SSS-SEIH Nano And More, USA). Tip wear and breaking is a major problem when using such sharp tips. To avoid breaking the tip during approach, the set point is set to 95% of the free amplitude which false engages the feedback with the surface. The set point is then gradually reduced until the surface is engaged. A slow scan rate of 0.5 Hz is also employed to minimize tip wear.

Different thicknesses of polymer are important for controlling nanoparticle absorption kinetics yielding the desired morphological behavior at different nanoparticle diameters, cf. chapters 3 and 4. For example, the island morphology requires a film thickness that is less than the diameter of the NP, whereas the peak and valley (PAV) morphology is observed for thicker films. The thermal conversion process is necessary to obtain smooth homogeneous films as the amphiphilic SAA copolymer is not readily soluble in either polar or non-polar solvents. Figure 2.1a shows an AFM image of piranha cleaned glass where the RMS roughness, Z_{RMS}, is 2.6 ± 0.05 nm. The glass slide is rougher than a surface of 12nm diameter NPs grafted to a SAA film on a mica subsrate, figure 2.2b, where the Z_{RMS} equals 2.1 nm. The glass slide is rougher than StBA films converted to SAA on mica which yields a smooth film with a RMS roughness, $Z_{RMS,}$ of 0.27 ± 0.01 nm, Figure 2.1c.

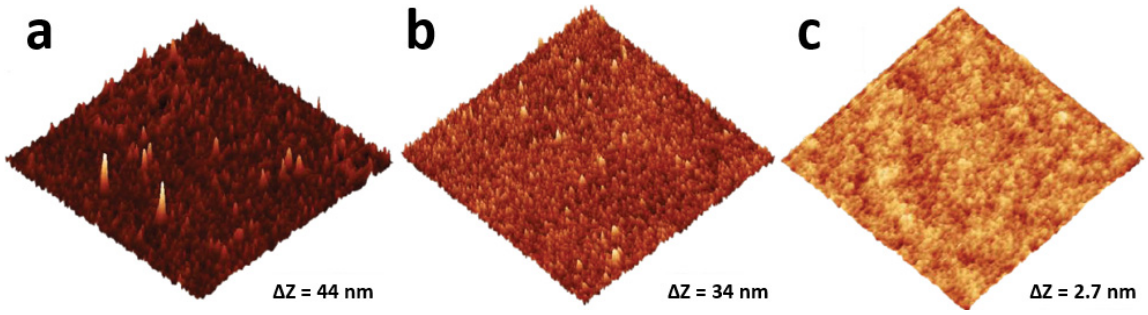

Figure 2.1: Topographic comparison of NP-SAA and SAA surface roughness on the mica. 5 µm x 5 µm AFM topography of, **a.**, a glass coverslip, **b.**, a bilayer of 12nm aminated silica nanoparticles covalently attached to a 40nm thick SAA film on mica, and **c.**, PS-r-PAA on mica after treatment with EDC-NHS and a 30min incubation in ethanol.

Because SAA films that are not cross-linked by NP grafting swell in water and ethanol,[1] continuous AFM of the NP-SAA composites for 8 h confirms the NP-grafted SAA films are stable in liquid. During 8 h of continuous AFM imaging of the same area in water, no changes in surface morphology are observed. This confirms that dry imaging of surfaces is adequate to characterize their morphology and validates that surfaces remain stable in motility assay buffer for the attachment of actin and the myosin V motility assays.

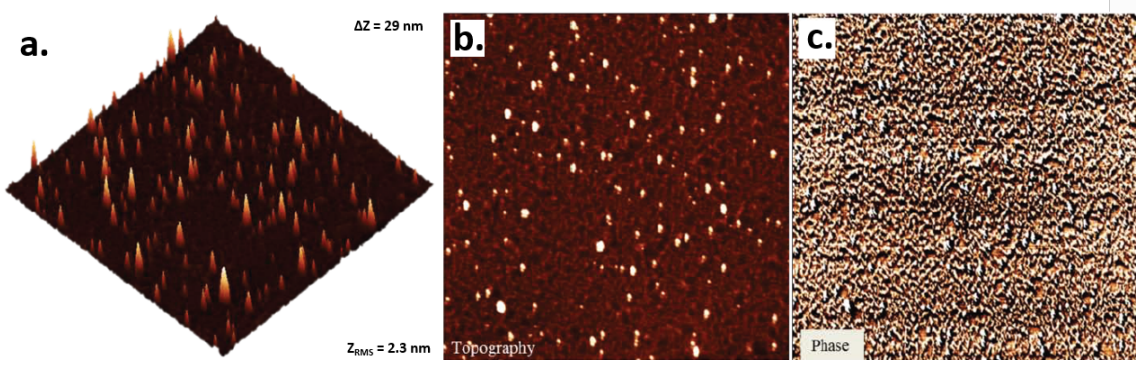

Figure 2.2: 5µm x 5µm AFM image of 20nm diameter particles grafted to a 37nm thick SAA film. a. 3D projection of topography of the island morphology, and **b.**, top-down view of the same data which exhibits a Z_{RMS} of 2.3 nm. **c.** AFM phase image for the same area. The similar contrast between lumps in the film and the particles on the surface in the phase image indicates that both areas have the same elastic modulus and surface chemistry consistent with the idea that the roughness in the lower region is due to particles that have sunken into the film.

Figure 2.2 shows that for the island morphology, the underlying basal plane consists of a partially sunken layer of NPs that provide the necessary amine groups and electrostatic attraction to immobilize f-actin. Figure 2.2 shows 20 nm particles attached to a 37 nm thick SAA film. The topography in figure 2.2a and 2.2b demonstrates that the individual particles bind to the top of the basal plane to create an island morphology with h_{avg} = 20 nm (= D_{NP}) and spacing 350 nm. From Figure 2.1c, the roughness of the polymer film without NPs is 0.27 nm and the RMS roughness of the basal plane (low region excluding protruding particles) in figure 2.2b is double, 0.49nm. Figure 2.2c shows the phase image of the same area. Phase images in AFM are sensitive to both the chemical interaction of the surface with the tip and the underlying modulus of the surface. With this phase image it is possible to identify the NPs which are imbedded in the basal plane and are not clearly visible in the topography. This evidence suggests that a layer of NPs are imbedded into the polymer film at the basal plane.

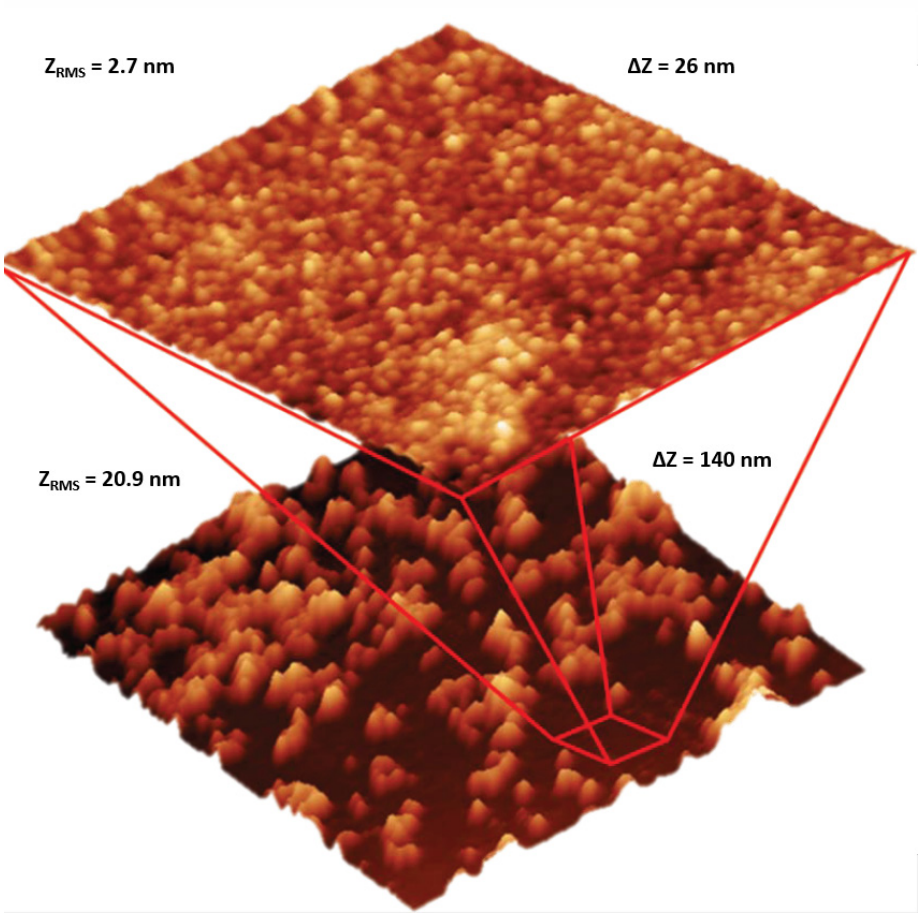

Figure 2.3: 45nm particles incubated on a 100nm thick SAA film shows NP sub-layer. Here, the bottom shows a 5 µm x 5 µm area and the zoomed area of 1 µm x 1 µm (top) shows the film on the bottom where nanoparticles are packed into the film.

Figure 2.3 shows the same effect for the 45 nm nanoparticles. The 5 µm x 5 µm scan on the bottom shows average feature height, h_{avg}, of 50 nm, and the surface exhibits a RMS roughness of 20.9 nm. A 1 μm^2 image was taken of the area between the particles revealing that the lower regions exhibit a RMS roughness of 2.7 nm, or roughly 10 fold that of the bare polymer film.

The inclusion of aminated nanoparticles in the film results in an electrostatic compensation at the surface attributable to the attraction of the basal plane to the actin filaments. This is supported by the immobilization of actin on the basal plane of surfaces where

the areal density of islands is extremely low, less than 0.2 features per μm^2. F-actin does not immobilize on untreated SAA surfaces.

2.4 Discussion of surface charge

The primary driving force for adhesion of actin to the nanoparticles is the electrostatic potential. Actin has a net charge of -4 electrons per nm, whereas typical measurements of APTES functionalized glass yields a zeta potential of greater than +30mV. Zeta potential measurements of NP-SAA composites are +5 to 10mV for the island morphology. Since the island morphology represents the lowest NP coverages, their positive Zeta potential confirms that all surfaces are electrostatically positive. For surfaces coated with a homogeneous charge density, the magnitude of the surface charge is less important for f-actin immobilization. F-actin attachment becomes favorable when the surface charge becomes positive and is insensitive to the magnitude of the surface potential.[5] At physiological salt concentrations, long distance interactions are screened, and actin must find the surface randomly to stick. Thus, the magnitude of the potential does not greatly influence the concentration of actin found on the surface. The magnitude of the potential can influence the structure of the absorbed actin. Increasing the local surface potential by increasing the NP diameter can alter f-actin structure, and affect myosin V velocity, as discussed in chapter 5.

2.5 Debye length in buffered media

The short Debye length, 1.7 nm, in a buffer medium, favors the control of f-actin binding strength by surface roughness parameters because when long distance interactions are screened, the probability of actin immobilization close to the coverslip is directly related to the likelihood of a bend in the filament matching a void in the surface features. Because of the exponential dependence of the electrostatic potential with distance, the electrostatic attraction

between f-actin and the surface becomes negligible at a distance of 8.5nm from the surface.[6] Thus, actin will only be attracted by the aminated NP if it is within 8.5 nm, or approximately f-actin's diameter, ~7 nm, from the NP surface. Actin adopts a side-on wobbly conformation on the island morphology (cf. figure 4.2b) when there are few tethering points (NPs) along the length of the filament. Furthermore, filaments bound to the peaks of NPs tend are more weakly attached to NPs with D_{NP} = 20 nm compared to larger NPs (i.e., D_{NP} = 85 nm). Wobbly filaments are occasionally observed jumping between attachments on the smaller NPs but are fixed on the larger NPs due to a larger electrostatic force associated with larger diameter particles. Filament immobilization occurs when the majority of a filament contour can be confined within this 8.5 nm layer, cf. figure 4.2. Whereas it takes time for filaments to bend around and immobilize on surface features, immobilization of actin is found to be permanent and irreversible.

2.6 The Bending energy model

Surface topography is characterized by AFM and then related to actin adhesion using the WLC model. AFM analysis is performed using the freely available software, Gwyddion. The average spacing, h_{avg}, of features is determined by counting the number of topographic features, N, using grain analysis and then converting this number into an average spacing, S, namely

$$S = 1.075\sqrt{\frac{A}{N}} \qquad (2.3)$$

where *A* represents the area of the AFM scan, which is 25um^2. The scaling factor reflects that the highest possible areal coverage is a close packed monolayer at 90.69%. Therefore, at 90.69% coverage, the spacing between the features converges to the diameter of the nanoparticle. The scaling factor of 1.075 accounts for the geometric difference for hexagonally packed spheres being counted in a square area to ensure that the appropriate surface coverage

of a monolayer converges to an average spacing of D_{NP}. If instead the spheres adopt a simple cubic lattice, this factor corresponds to a 78.54% packing density and equals unity.

As discussed in chapter 4, in-plane bending of f-actin parallel to the surface is more favorable than filaments contouring over features. Thus, the WLC formalism expresses the bending energy at a specific height above the surface. The energy of actin filaments is described in terms of filament length, L_o, bending radius, R, and persistence length, P, as follows:[7]

$$E_b = k_b T \frac{PL_o}{2R^2} \quad . \qquad (2.4)$$

Drawing an arc of actin as it conforms to the surface (Figure 4.3b) allows one to relate the geometric term R to the two surface parameters S and h by applying Pythagorean theorem, where

$$R = \frac{{h_{avg}}^2 + S(h)^2}{2h_{avg}} . \qquad (2.5)$$

By inserting equation 2.5 into 2.4, equation 4.1 in chapter 4 is determined. This relationship is important because it relates two key surface parameters, feature size and spacing, to the energetic penalty for attaching actin to the substrate.

2.7 Bending energy, E_b, of f-actin on polymer nano-composite surfaces

To directly compare experimental results with the bending energy model, the bending energy is plotted against the static variable in the evolution of the island and PAV morphologies in figures 2.4a and 2.4b, respectively. The data points represent S and h_{avg} values from AFM analysis of island and PAV morphologies. The lines show the predicted E_b values determined at constant average height (diameter of each NP for islands, (figure 2.4a) or spacing (mean spacing of all samples exhibiting for PAV, Figure 2.4b). Feature spacing is the primary changing variable

for the island morphology while growth of the hierarchial features of the PAV morphology complicate $E_b(h)$.

Figure 2.4a, shows a close correlation between isometric height contours as NP density increases on surfaces exhibiting the island morphology. Feature spacing is the only variable changing in the island morphology indicating that NPs are not sinking or clustering during the formation of this morphology. For the PAV morphology there is little correlation between the feature height and spacing observed as NP aggregates grow.

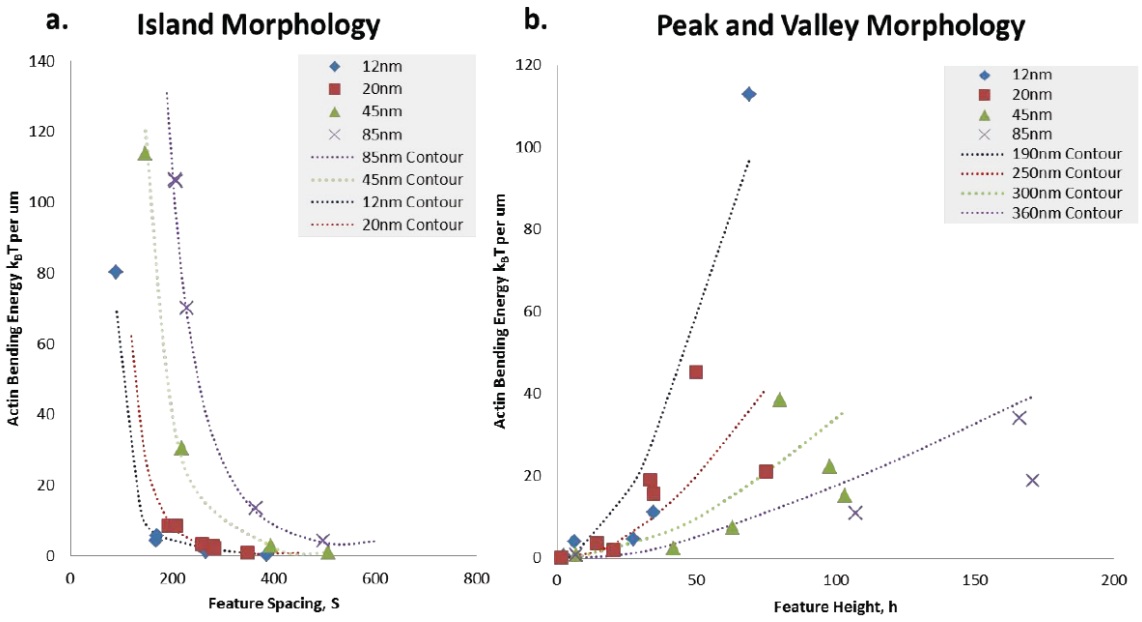

Figure 2.4: Evolution of bending energy as an function of feature height, or feature spacing. a. Data points show E_b for the island morphology plotted along isometric height curves indicate that in this regime feature spacing is the only parameter changing. **b.** Isometric spacing curves corresponding to the average spacing measured in the peak and valley morphology at each NP size are plotted agaisnt data where E_b is determiend from surfaces. The coarsening mechanism less closely follows a trend for the formation of the polydisperse features.

2.8 E_b as a function of height above the surface

To determine the bending energy as a function of height from the basal plane (figure 4.4b), AFM images are thresholded and analyzed by the number of features, N, as a function of height per 5µm x 5µm scan area. Statisically, it is imporant that the image quality is good

enough to resolve individual NPs, large enough to contain numerous features, and without scan lines or scars. Since small pits or imperfections in the surface can arise due to film swelling, the basal plane is found by thresholding and the corresponding height value subtracted off of the measured value in each threshold to obtain a height above the basal plane, h, at which the feature density was measured by grain analysis. The maximum number of grains at any slice was taken to be the total number of features, and the slices taken below that plane were discarded. A typical distribution of feature number versus height from the basal plane obtained from this method can be seen in figure 2.5a.

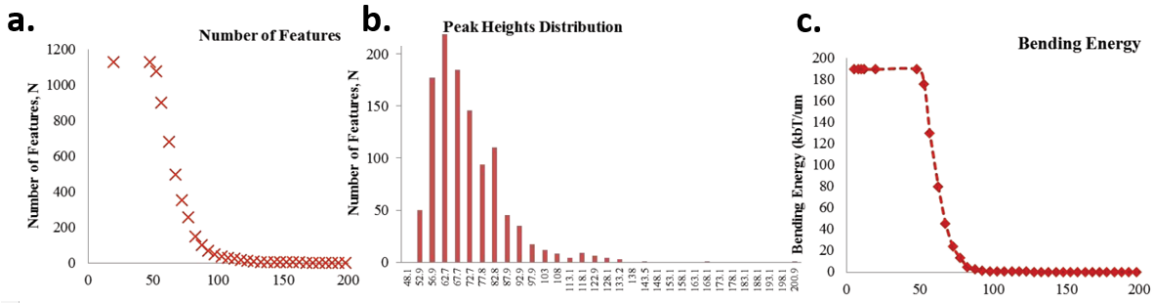

Figure 2.5: Feature size distribution as a function of height from the basal plane. Distributions come directly from AFM image analysis of a peak and valley morphology generated from 45nm diameter aminated NPs. **a.** The number of features counted at 5 nm increments from the basal plane. **b.** Corresponding peak heights distribution determined from binning the data in a. **c.** Bending energy, $E_b(h)$ comes from the bending energy equation where h is the average height determined from b. and the particle average spacing, S, is calculated from equation S1 where N(h) is shown in figure 2.5a.

As height increases, the number of features, N, decreases at a rate proportional to the polydispersity of the features. The difference in the number of features N counted at two adjacent heights gives the number of features whose size (maximum elevation) falls within that height range. Thus, a histogram is generated representing the distribution in feature heights for a given surface, figure 2.5b, which makes it possible to determine the mean feature height, h_{avg}. In figure 2.4, the mean feature height is 71.5 nm for the PAV morphology with D_{NP} = 45 nm and the RMS roughness is 22 nm. The average height is then plugged into equation 1, and the values

of N in figure 2.5a are used to calculate a mean spacing, S(h), at each slice height by using equation 2.3. This determines a value of E_b at each height , $E_b(h)$ shown in Figures 4.4 and 4.5 and further discussed in chapter 4.

To determine the thermodynamically favored state of actin conformation on each surface, $E_b(h)$ is compared to van der Waals attraction, and the electrostatic potential between actin and the surface as well as between actin and the features, figure 4.5. The van der Waals and electrostatic surface potential is calculated analogously to Park et al, whereby the van der Waals potential is determined from the Hamaker constant between actin and APTES which is taken to be approximately k_BT.[5,6]

$$W(h) = \frac{-A_{APTES-Actin}(2R_{Actin})^{1/2}}{h^{3/2}} \qquad (2.6)$$

Here, R_{Actin} is taken to be 3.5 nm, where actin is treated as a cylinder[8] and h is the height above the basal plane. The electrostatic potential depends upon the surface potentials, ψ, of both actin and the APTES functionalized NPs and the range over which the attractive interaction can be felt depends upon the Debye length, κ = 1.7 nm, for the buffer solution employed in this study.

$$V(h), P(h) = \frac{2(2\pi)^{1/2}\varepsilon_{Water}\varepsilon_o}{(\kappa R_{Actin})^{1/2}}\left[\psi_{APTES}\psi_{Actin}e^{-\kappa h} + 0.35{\psi_{APTES}}^2\left(\frac{1-2\varepsilon_{Actin}}{(\pi\kappa R_{Actin})^{1/2}}\right)e^{-2\kappa h}\right.$$
$$\left. + 0.35{\psi_{Actin}}^2\left(\frac{R_{Actin}}{R_{Actin}+h}\right)^{1/2}\left(\frac{1-2\varepsilon_{APTES}}{\varepsilon_{Water}\left(\pi\kappa(R_{Actin}+h)\right)^{1/2}}\right)e^{-2\kappa h}\right]$$

(2.7)

The value of ψ_{Actin} is -35 mV and the value of ψ_{APTES} depends on the charge density of amines per unit area on the surface,V(h), and generated by the features, P(h). The relationship from which the areal charge density determines the surface potential is shown in equation 2.8. The charge density σ is calculated as 0.2304 Cm^{-2} by assuming a grafting density of 1.5 APTES chains per nm^2. The corresponding surface potential is found to be 143 mV and this value is used in the plot of V(h). To determine P(h), the areal coverage of features is determined at the average height, h_{avg}. By multiplying the number of features per unit area at h_{avg} by the area occupied by a sphere of diameter h_{avg} a fraction of surface coverage at h_{avg} can be used to approximate σ at h_{avg} using the value of 0.2304 Cm^{-2} as the potential of a smooth APTES surface. The relative charge density obtained is an effective surface potential associated with the plane at h_{avg}. These values range from 2 mV to 25 mV in magnitude depending on the areal coverage of nanoparticulate features.

$$\sigma = \sqrt{8 n_o \varepsilon \varepsilon_o k_B T} \sinh\left(\frac{e\psi_{APTES}}{2k_B T}\right) \qquad (2.8)$$

The ionic strength, n_o, of the buffer employed in this study is 29 mM and *e* is the elementary charge. ε_{APTES} and ε_{Actin} are taken to be 15 in accordance with previous observations.[5,6]

2.9 F-actin preparation

Globular-actin (G-actin) was isolated and purified from rabbit muscle as described[9] and stored in G-actin buffer (2 mM Tris buffer (pH 8.0), 0.2 mM $CaCl_2$, 0.2 mM ATP and 0.5 mM dithiothreitol (DTT)). 1 µM rhodamine-phalloidin stabilized f-actin was prepared by mixing 1 µM G-actin gently with 4x F-actin buffer (300 mM KCl, 10 mM $MgCl_2$, 40 mM HEPES (pH 7.0)) and 1.1 µM rhodamine-phalloidin (Molecular Probes, R415). The mixture was incubated at room

temperature for 10 min, transferred onto ice, stored at 4 ^{o}C, and used within 1 month.[10] Stock M5 buffer solution (25 mM KCl, 20 mM HEPES (pH 7.6), 2 mM $MgCl_2$, 1 mM EGTA (Sigma, E4378)) was stored at 4 ^{o}C prior to each experiment and 100 μg ml^{-1} wild-type calmodulin (CaM) and 100 mM DTT were added to the M5 buffer (M5+ buffer) for both actin binding and motility assays consistent with previous work with myosin V.[11,12]

2.10 Myosin V motility assays

Flow cells were constructed creating ~10 μL channels by attaching the nano-composite coated coverslips to cleaned glass slides with strips of double-sided tape (3M). F-actin and quantum dot functionalized myosin V were imaged with both 488 nm and 532 nm solid-state laser (Coherent) under rotating TIRF excitation by oscillating a piezo-controlled mirror at 50 Hz with orthogonal sinusoids 180^{o} out of phase. This greatly reduced fringes and variable intensity in the imaging field which aids subsequent single particle tracking analysis. Movies were recorded at a 50 ms exposure time in 100s or 150s intervals using the *In Vivo* imaging software package, Thermo Fisher, and a Cascade-512B electron multiplier-CCD camera, Photometrics. Run-lengths and run velocities were obtained at super-resolution using the freely available FIESTA single particle tracking software.[13] The end-end distance of each run was used to determine the velocity, and the mean velocity and standard deviation was recorded for greater than 100 velocity measurements at each ATP concentration. To determine the average step size of the motor, myosin V position versus time was first obtained for individual motors using FIESTA. The position versus time data was then exported into Matlab and fit using a discrete step-finder algorithm previously developed.[14]

Constructs of myosin V, Myosin V dimeric HMM with biotinylated C-termini, were attached to streptavidin conjugated quantum dots, QD (Q10121MP, Invitrogen). QD functionalization was accomplished by incubating the myosin V, initial dimer concentration 0.6

μM diluted to 12 nM, with the QD, 1 μM, and 20 mg/mL BSA, in a 1:1:1 mixture. F-actin (250 nM) was allowed to react with the surfaces for 1 minute incubation time before the being washed out with M5+ buffer. The surface was then blocked for 10 min with 20mg/mL BSA. The functionalized motors were added to a solution of M5 buffer, 0.1 mg/mL CaM, 100 mM DTT, glucose, 10 μM ATP, 10 mg/mL BSA, and an oxygen scavenging system (glucose oxidase, catalase and glucose)[10] and wicked into flow cells. The final concentration of myosin V and QD655 was 0.038 nM and 3.3 nM respectively.

2.11 Nanogel Synthesis

Analytical grade reagents were used as received. Dextran with a M_w = 70 kDa and rhodamine B isothiocycyanate-dextran with M_w= 64-76 kDa from *Leuconostoc* ssp. Were obtained from Fluka Chemie (Buchs, Switzerland) and Sigma-Aldrich (St. Louis, MI, USA) respectively. Lysozyme and silver nitrate ($AgNO_3$) were purchased from Sigma-Aldrich. No. 1 glass coverslips (25 × 40 mm^2) and phosphate buffered saline (without Ca^{2+} and Mg^{2+}), were purchased from Fisher Scientific (Hampton, NH, USA).

Dextran-lysozyme conjugate hydrogels (Dex-Gel) are synthesized through a two-step heating process described previously.[15,16] Amino groups from lysozyme react with dextran's terminal carbonyl groups in a KBr saturated desiccator forming lysosome-dextran conjugates. Once conjugated, gelation is achieved by heating. The conjugate powder is dissolved in water (5 mg/mL) and the pH is raised to 10.7 (isoelectric point of lysozyme) and subsequently heated at 80 °C for 30 min to form a physically cross-linked hydrogel with hydrophobic residue (lysozyme) core and dextran shell.[17] Dex-Gels are then purified through ultracentrifugation and stored at 4°C.

Rd Dex-Gel

To prepare fluorescently labeled Dex-Gels, rhodamine B isothiocycyanate-and lysosome are mixed in buffer at a 1:1 ratio. The pH is titrated to 7-8 using 0.1M NaOH before the solution is lyophilized. The lyophilized powder is annealed for 24 h at 60 °C in a desiccator with a saturated KBr saturated atmosphere with 79% relative humidity. The gelation protocol described above is then followed yielding similar core-shell Dex-Gels with a rhodamine-B labeled shell.

Ag Dex-Gel

Silver nanoparticles (AgNPs) are grown in Dex-Gels through an additional step to the above procedure. Using 25 mM $AgNO_3$ as a precursor an solution of $AgNO_3$ and Dex-Gel is autoclaved to reduce Ag ions and nucleate AgNPs within the gel. Any outstanding AgNPs are separated from the NG solution through dialysis in deionized water. The subsequent Ag Dex-Gels are roughly 160 nm in diameter and contain 20.4 wt% silver composed of ~ 5 nm diameter AgNPs.

Polyacrylamide gels (PAGs) with defined elastic moduli are formulated using various mixtures of the monomer, acrylamide, and the cross-linker, bis-acrylamide, in accordance with two previously set forth protocols[18,19]. The PAGs are grafted onto an amino-silanated cover slip using a dialdehyde for modulus measurement in phosphate buffered saline (PBS) using an Asylum MFP 3D and on-board analysis software.

2.12 Polyacrylamide Gel Synthesis

Piranha cleaned cover slips are coated with 3-aminopropyltriethoxysilane (APTES) via physical vapor deposition (PVD). Cover slips are then placed in a 0.5% glutaraldehyde solution in PBS for at least 30 minutes. Any excess APTES or glutaraldehyde is rinsed off with PBS after their respective processes. Piranha cleaned slides are chloro-silanated through PVD by

dichlorodimethylsilane (DCDMS). Six solutions containing different percentages of acrylamide and bis-acrylamide in PBS are used to develop PAGs with elastic moduli ratings spanning from 70 Pa to 70 kPa. *N*,*N*,*N*',*N*'-tetramethylethylenediamine (TEMED) is added to initiate free radial polymerization while ammonium persulfate (APS) is added to catalyze the polymerization process. A concentration of 0.1 wt% TEMED and 0.1 wt% of APS are used for all solutions. Once TEMED and APS are thoroughly mixed, the solution is drop-casted onto a chloro-silanated slide. An amino-silanated cover slip is dropped onto the chloro-silanated slide, creating a "sandwich" effect with the gelling solution in the middle. When polymerization is complete, the chloro-silanated slide can be peeled off leaving a ~500 μm thick PAG covalently grafted to the coverslip. The amount of solution drop-casted will affect the thickness of the gel, but will not affect the modulus rating.

PAGs prepared for rheometry are drop cast ~10 mm thick by pouring 500 μL of polymerizing solution into a chloro-silanated glass boat. The gels are then removed from the boat and placed directly onto a RFS3 rheometer with PP25 chuck applying 200 g to the gel. Rheology is conducted at 5% strain and 24.1 C between 0.01 and 500 Hz in triplicate. Frequency sweeps at 1% or 3% strain return the same data as 5%.

2.13 THP-1 Cell Culture

THP-1 cells stably transduced with GFP-actin were maintained in suspension culture in RPMI media (Gibco, Grand Island, NY, USA), supplemented with 10% FBS (HyClone, Rockford, IL, USA), 1% penicillin streptomycin (Invitrogen, Carlsbad, CA, USA), and 0.05 mM 2-mercaptoethanol. For all experiments, cells (13,000 cells/cm^2) were plated on 35 mm polystyrene petri dishes (BD, Ashland, MA, USA) containing the glass slides. THP-1 cells were stimulated with the addition of 1 μg/mL of Phorbol 12-myristate 13-acetate (PMA) for 72 h.

2.14 Viability of PMA-stimulated THP-1 cells

Following stimulation, THP-1 cells were incubated with the different Dex-Gels (20 μg/mL) for 24 h. As a control, cells were incubated with media. After 24h incubation, the cells were washed with HBSS to remove any residual Dex-Gel. The viability of untreated THP-1 cells, Dex-Gel and Ag nanogels was determined by fluorescence microscopy. Live cells were stained with calcein violet (750 nM) and dead cells with ethidium homodimer (2 μM). The viability of cells incubated with rd Dex-Gels was determined by optical microscopy following trypan blue staining (0.4 %). For each condition, 5 images were collected using 10 x objective lens and viable cells were counted using Image J. This experiment was performed in triplicate.

Epifluorescence microscopy was performed using an Olympus IX70 microscope (Olympus, Melville, NY, USA) outfitted with a Chroma Photofluor metal halide light source (89 North, Burlington, VT, USA). Images were captured using a SensiCam QE camera (The Cooke Corp., Romulus, MI, USA) (2 × 2 binning, 688 × 520). IPLab software was used for image acquisition and to control the LUDL programmable filter wheels, shutters, and focus (Ludl Electronic Products, Hawthorne, NY, USA). ImageJ (NIH, Bethesda, MD, USA) was used for image analysis.

2.15 TIRF-AFM of THP-1 cells

Optical microscopy and AFM was performed using an MFP3D AFM (Asylum Research) combined with an inverted Nikon TE-2000U microscope equipped with a Nikon ×100, 1.49 NA objective. Rd Dex-Gel fluorescence was captured via 532 nm laser excitation (CrystaLaser) and a CCD camera (Cascade-512B, Photometrics) with 200 ms exposure time controlled through NIS Elements software package. All cells were observed with white light illumination from the MFP-3D during modulus characterization. Modulus characterization of cells was performed using 2

μm diameter SiO_2 microparticle functionalized SiN cantilevers with nominal spring constant 0.08 N/m (CP-PNPS-SiO-A, Nano And More, USA). Cantilever spring constants were manually calibrated in air using the MFP3D prior to each experiment using a clean glass substrate. Inverse optical lever sensitivity was determined in HBSS solution prior to each round of measurements. Elastic moduli were determined by fitting the indentation curve to the Hertz model adjusted for a spherical indenter using the Asylum Research built in analysis software. The deflection trigger for each indentation was adjusted prior to each round of measurements to obtain an indentation depth near 500 nm using 1-2 arbitrarily chosen cells.

2.16 Conclusion

In this chapter, the details regarding the preparation and characterization of NP-SAA composites are discussed in detail. Evidence for NPs sinking into SAA films is provided using AFM topography and phase imaging. Super-sharp atomic force microscope tips are used to maximize resolution of 12 nm to 85 nm diameter NPs in SAA thin films of thickness 30-200 nm which are crucial to enable accurate modelling of the surface topopgraphy for f-actin attachment by the bending energy model. A derivation of the bending energy as a function of distance from the substrate, E_b , is discussed in detail. Details of the surface electrostatics are discussed, namely a derivation of the surface potential, *P(h)*, is derived for the short Debye length, 1.7 nm, in buffer solution, using equation 2.7. A detailed discussion of the interaction between f-actin and nano-textured surfaces justifies how electrostatic attraction is the means of f-actin immobilization on NP-decorated SAA films even at high salt concentraions. Details of actin preparations and myosin V motility assays are provided including the mixing ratio of myosin V to QDs in which QDs are 100-fold excess to prevent multiple labelling of QDs by myosin. Finally, methods describe the synthesis of novel Dex-Gel drug carriers which are used to treat THP-1 cells with AgNPs and rhodamine B to assess their toxicity using viscoelasticity

measured by AFM. This section is intended provide future researchers with the necessary information to design future experiments.

2.17 References

1. McConnell, M. D.; Yang, S.; Composto, R. J. Covalent Nanoparticle Assembly onto Random Copolymer Films, *Macromolecules*, 42, **2009,** 517-523.
2. Strutt, J, On the transmission of light through and atmosphere containing small particles in suspension, and on the origin of the blue of the sky, *Philosophical Magizine*, 5, 47, **1899,** 375-394.
3. Mie G, Contributions on the Optics of Turbid Media, Particularly Colloidal Metal Solutions, *Annalen der Physik, IV*, 25, 3, **1908**, 377-445.
4. Sauerbrey G, Verwendung von Schwingquarzen zur Wägung dünner Schichten und zur Mikrowägung *Z. Phys.* 155**,** 2, **1959**, 206.
5. Park, J. H.; Sun, Y.; Goldman Y. E.; Composto, R. J. Self-assembled charged hydrogels control the alignment of filamentous actin, *Soft Matter*, 6, **2010,** 915-921.
6. Israelachvili, J. N. *Intermolecular & Surface Forces,* Academic Press., London, Second Edition, **1992**.
7. Nelson, P. *Biological Physics: Energy, Information, Life,* W.H. Freeman and Co., New York, **2008,** 341-385.
8. Cooper, G.M. *The Cell: A Molecular Approach,* 2nd Edition, Sinauer Associates, Sunderland, MA, **2000**.
9. Pardee, J.D.; Spudich, J.A. Purification of muscle actin. *Methods Cell Biol*. **1982,** 24, 271–289.
10. Beausang, J.F.; Sun, Y.; Quinlan, M.E.; Forkey, J.N.; Goldman, Y.E. *Single Molecule Fluorescence Polarization via Polarized Total Internal Reflection Fluorescent Microscopy*. In: Sialiano, I., *Laboratory Manual for Single Molecule Studies*, Cold Spring Harbor Laboratory, Cold Spring Harbor, NY. **2007.**
11. De La Cruz, E.M.; Wells, A. L.; Rosenfeld, S. S.; Ostap, E. M.; Sweeney, H. L. The kinetic mechanism of myosin V. *Proc. Natl Acad. Sci. USA* **1999,** 96, 13726**–**13731.
12. Harada, Y.; Sakurada, K.; Aoki, T.; Thomas, D.D.; Yanagida, T. Mechanochemical coupling in actomyosin energy transduction studied by in vitro movement assay. *J. Mol. Biol.* **1990,** 216, 49-68.
13. Ruhnow F, Zwicker D, Diez S, Tracking single particles and elongated filaments with nanometer precision, *Biophysical Journal*, , 100, 11, **2011,** 2820-2828.
14. Kerssemakers JWJ, Munteanu EL, Laan L, Noetzel TL, Janson ME, Dogterom M, Assembly dynamics in microtubules at molecular resolution, *Nature*, 442 **2006,** 709-712.
15. Coll Ferrer, Carme, Robert Ferrier, David Eckmann, and Russell Composto, A facile route to synthesize nanogels doped with silver nanoparticles, *J Nanopart Res,* 15, **2013,** 1323-1325 .
16. Coll Ferrer, Carme, Peter Sobolewski, Russell Composto, and David Eckmann, Cellular Uptake and Intracellular Cargo Release from Dextran Based Nanogel Drug Carriers, *Journal of Nanotechnology in Engineering and Medicine* 4 **2013,** 1-8.
17. Li, Juan, Shaoyong Yu, Ping Yao, and Ming Jiang, Lysozyme−Dextran Core−Shell Nanogels Prepared Via A Green Process, *Langmuir* 24, 7, **2008**, 3486-3492.

18. Tse, Justin, and Adam Engler. Preparation of Hydrogel Substrates with Tunable Mechanical Properties*, Current Protocols in Cell Biology,* 10, 16, **2010**, 1-16.
19. Fischer, Robert, Kenneth Myers, Margaret Gardel, and Clare Waterman, Stiffness-controlled three-dimensional extracellular matrices for high-resolution imaging of cell behavior, *Nature Protocols,* 7, 11, **2012**, 2056-2066.

Chapter 3: Hierarchical Nanoparticle Topography in Amphiphilic Copolymer Films Controlled by Thermodynamics and Dynamics

3.0 Introduction

Shark[1] and pilot whale skin, [2] the lotus leaf, [3] and the mollusk shell[4] are natural examples of low-friction, self-cleaning, non-fouling surfaces. The physical and chemical attributes of hierarchical topographic features, in particular the combination of micro and nano-periodic topographies[3,4], enable organisms to thrive in highly corrosive, dirty, and infectious environments[5]. Engineered surfaces that (bio)mimic these topographies, utilize fabrication techniques such as E-beam lithography, [6] dip coating, [7] photolithography,[1] stamping combined with thermal evaporation,[3] layer-by-layer deposition,[8] and electro-spinning.[9] All of these are high-cost, low throughput fabrication techniques. Here, polymer-nanoparticle composite films are proposed as low-cost biomimetic surfaces that lend themselves to self-assembly across large areas by simply immersing a random copolymer film in a solution of functionalized nanoparticles. Moreover, by varying copolymer reactivity, immersion time, film thickness, and particle size, hierarchical nanoparticle surface structures from the nano to microscale can be designed and utilized for control over biopolymer attachment.[10]

Polymer-nanoparticle composite films contain complementary components which enable parallel tuning of physical and chemical properties.[11] Namely, a polymer binder forms an adherent coating on the substrate, while a nanoparticle (NP) filler provides control over mechanical properties such as topography.[8] Polymers are an attractive binder because they are easy to process by spin coating or casting, and available in a wide variety of physical properties, from rigid plastics to thermoplastic elastomers.[12,13] Nanoparticles (NPs) are attractive fillers

because they are readily available in a wide variety of shapes, sizes, and compositions that result in improved mechanical, [14] electrical,[15,16] and optical properties.[17,18]

Polymer-NP composite properties depend on nanoparticle loading dispersion. The volume fraction and dispersion of NPs define how and how much NPs enhance properties.[19] The volume fraction of NPs encapsulated within the polymer matrix directly determines the magnitude of the property change, i.e., strength or conductivity, imparted to the film. In many cases film properties dramatically change near a specific volume fraction of NPs and are relatively insensitive NP concentration above or below this value. For example, around the percolation threshold, conducting NPs rapidly transition an insulating polymer film to a conductor, but conductivity does not change greatly with NP volume fraction above or below the threshold.[20] The dispersion of NPs within the polymer governs the amount of available interface and the effective NP size. [19,21] For example, if a specific size of gold NP is incorporated in a film to absorb a corresponding wavelength, aggregation of particles within the film undesirably shifts the absorption spectrum.[17] Nanocomposite films become natural anti-fouling coatings when the exhibit hierarchical roughness, since roughness is linked to super hydrophobicity and self cleaning properties.[22-24] High volume fractions[8] and aggregation[25] of NPs in polymer films generate hierarchical roughness through the creation of multi-particle topographic features. Herein, the ability to generate controllable hierarchical topography by precise control of NP incorporation and dispersion is systematically investigated.

Polymer nanocomposite films exhibiting hierarchical surface topography can be prepared by the self-assembly of NPs at high volume fractions where NPs may become jammed or aggregated in the film.[8] Tunable topography is analogous to tunable dispersion at high NP volume fraction. At a low volume fraction NP dispersion is well understood. When NPs neutrally interact with the polymer, NP dispersion is dominated by the entropic penalty

associated with inserting particles into a film.[21,26,27] NP mixing entropy is a weak interaction that favors the dispersion of smaller NPs over larger ones. [21,26,27] NPs that are too large to entropically disperse, can still do so when NP-polymer enthalpic interactions are favorable. [17,26] The enthalpic interaction can be changed by altering the surface chemistry of the NP, and is a common way of engineering dispersion for normally immiscible NP-polymer systems.[21] The dispersion of NPs within polymers, including the self-assembly of long range ordered bicontinuous structures,[28] may be a facile route to biomimetic topography.[29] Herein, the effect of systematic changes in the enthalpic interaction at high NP loading fractions is investigated by changing the fraction of AA in the SAA films.

In previous studies, amine-functionalized nanoparticles (D_{NP} = 15 nm) were grafted into SAA films via surface acrylic acid groups.[30] The mole fraction of AA, NP concentration in solution, and reaction time were varied to control NP coverage and spacing. A high surface coverage of 70% was achieved by increasing surface roughness due to the swelling of AA at the surface. These studies were expanded by partially embedding NPs and by varying NP diameters from 15 nm to 290 nm to control coverage and subsequently contact angle.[31] Upon swelling, the SAA surface exhibited periodic undulations that allowed smaller nanoparticles (15, 50 and 106 nm) to reach a maximum coverage of 70%. Depending on particle coverage and roughness, the contact angle ranged from 75^o to 117^o.[31] At NP coverage between 30% and 70%, a transition between Wenzel and Cassie Baxter wetting was reported linking high NP coverage to hydrophobicity. In the present paper, NP diffusion and jamming within the SAA films can be controlled to create hierarchical NP structures with contact angles from 70^o to 170^o. Expanding upon prior studies, this study varies AA content to control film swelling and increase the concentration of NPs that sink into SAA during grafting, which together promote the diffusion and dispersion of NPs into the polymer.

In this study, the diffusion and jamming of amine functionalized silica nanoparticles is controlled by varying the acrylic acid mole fraction in SAA films from 2% to 29%, SAA2 to SAA29. Polymer composition regulates the formation of hierarchical NP structures and thereby the wetting and optical properties of polymer nanocomposite films. A surface morphology map shows the buildup of surface roughness as a function of SAA immersion time in a nanoparticle solution. The rate of NP accumulation increases with increasing AA content. For the most hydrophilic SAA, SAA29, NP diffusion into the film is very rapid, and the high NP mobility leads to aggregation within the film. However, for films with less than 5 mole percent AA, NPs jam at the SAA surface because they are thermodynamically prevented from entering the hydrophobic film. For SAA4, NPs initially bind randomly at short times (i.e., 5min) and eventually organize into a smooth monolayer with a RMS roughness of ~ 10nm at longer times (i.e., 60 min). At 13 mole percent AA the optimum balance between mobility and thermodynamics is achieved whereby the NPs are able to diffuse into the film, and densely pack into bicontinuous structures. The resulting jammed structure exhibits a hierarchical roughness with maximum transmittance (>95 %), and super hydrophobicity (contact angles up to 170^{o}). These surfaces are ideal for TIRF imaging of biomolecules such as f-actin, because of the low scattering from these coatings on glass and the ability to regulate the electrostatic attachment of biofilaments.[10]

3.1 Fabrication of amphiphilic copolymer films containing nanoparticles.

Figure 3.1 outlines the reaction scheme for generating polymer nanocomposite films. As shown in figure 3.1a, poly(styrene-random-t-butyl acrylate), StBA, films are spun cast from toluene onto either a silicon wafer or glass coverslip to produce films with an initial thickness of h_o = 100 nm. After drying in vacuum, StBA films are annealed at 135 ^{o}C, 155 ^{o}C, 170 ^{o}C, 185 ^{o}C and 200 ^{o}C under a flow of N_2 gas for 15h. Upon annealing at low temperatures (135, 155 and 170 ^{o}C), StBA partially converts to acrylic acid, AA, resulting in a random copolymer of S, tBA and

AA, whereas upon annealing at higher temperatures, (185 °C and 200 °C) StBA completely converts to AA. In both cases, the film thickness, h, decreases by an amount that depends on the percentage of tBA conversion (figure 3.1b). As illustrated in figure 3.1c, the partially or completely converted StBA films are then immersed in an EDC/NHS solution for up to an hour to react the acrylic acid groups (COOH) from the film with NHS. Figure 3.1d shows the partial and fully converted StBA films immersed in a 66 nM solution of amine functionalized silica nanoparticles (diameter = 45nm) which react with exposed NHS groups on the film surface. To control the attachment of nanoparticles, the films are immersed in the NP solution for 5 to 70 mins. Note that even the fully converted films have a majority of styrene (71 mole percent). The hydrophobic styrene prevents these films from dissolving (PAA is soluble in water) and/or detaching from the substrate during immersion of films to attach the NPs.

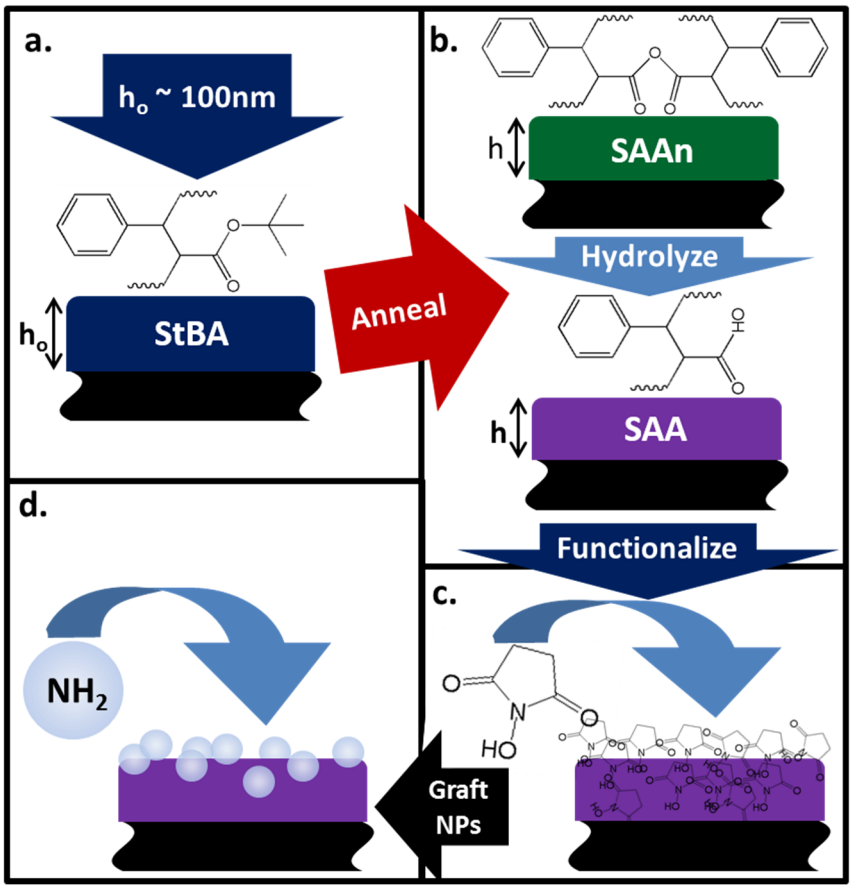

Figure 3.1: Process for preparing SAA-NP composite films. a. Spin casting of StBA from toluene onto Si wafers or glass yields a film of thickness h_o~100 nm. **b.** The surface is annealed at 15h at temperatures ranging from 135 ^{o}C to 200 ^{o}C. The film thickness decreases from h_o to h by an amount dependent on the anneal temperature due to tBA domains converting into AA by thermal deprotection. At temperatures greater than 170^{o}C the formation of the acrylic anhydride, AAn, (TOP) by coordination of AA is observed requiring an additional step (hydrolysis) of the film before functionalization. **c.** Functionalization of the AA domains with NHS primes the COOH groups on the SAA for covalent attachment of NPs. **d.** The covalent attachment of amine functionalized silica nanoparticles to the surface. Incubation time of SAA films in nanoparticles is varied to create diverse topography.

3.2 Conversion and characterization of copolymer films.

For a film supported by a rigid substrate, the volume change upon mass loss is directly related to the change in thickness. Assuming a uniform conversion throughout the film, the percent thickness change for the partial conversion of tBA to AA can be calculated from the monomer density, σ_x, monomer mass, M_x, and mole fraction of monomer, X_x, as shown in equation 3.1.

$$\Delta V/_{V_o} = (h_o - h_f)/_{h_o} = \frac{M_S X_S + M_{tBA} X_{tBA}}{\sigma_S X_S + \sigma_{tBA} X_{tBA}} - \frac{M_S X_S + M_{AA} X_{AA} + M_{tBA} X_{tBA}}{\sigma_S X_S + \sigma_{AA} X_{AA} + \sigma_{tBA} X_{tBA}} \Bigg/ \frac{M_S X_S + M_{tBA} X_{tBA}}{\sigma_S X_S + \sigma_{tBA} X_{tBA}} \qquad (3.1)$$

The molecular weights and densities of S, tBA, and AA are 104.15, 128.17, and 72.06 g/mol, and 1.06, 1.05, and 1.22 g/cm^3 , respectively.[32] The density of poly (sec-butyl acrylate) was used for the tBA density. For 100% conversion of tBA to AA, X_{AA} = 0.37, the theoretical decrease in copolymer film thickness is 23%.

The conversion of tBA to AA is controlled by the annealing temperature of the StBA film as represented by figures 3.1a-b. For films with an initial thickness h_o ~ 100 nm, Table 1 shows the percent thickness change after annealing at 135,155, 170, 185 and 200 °C. At the lowest temperature, 135 ^{o}C, film thickness decreases by 2.4 ± 0.9 %, whereas at 170 ^{o}C, the decrease is

11.7 ± 1.7%. However, at the highest temperatures, 185 and 200 °C, the thickness decreases by ~25%. To ensure that the thickness decrease was not due to solvent evaporation and/or PS degradation, a PS (M_n = 100kDa) film with initial thickness 91.1 ± 1.3 nm was prepared using the same procedure as the copolymer films. The PS film showed no measurable decrease in thickness after annealing at 200 °C for 15 h (not shown) indicating that the thickness decrease in the StBA films was mainly due to the conversion of tBA to AA.

T (°C)	$(h_o-h_f)/h_o$ (%)	X_{tBA} to AA (mol%)	Copolymer Composition (wt %)
135	2.4 ± 0.9	10.0	S_{59}-tBA_{39}-AA_2 (SAA2)
155	4.3 ±1.2	17.8	S_{60}-$tBA_{35.7}$-$AA_{4.3}$ (SAA4)
170	11.7 ±1.7	49.5	S_{64}-tBA_{23}-AA_{13} (SAA13)
185	24.6 ±2.1	107.5	S_{71}-AA_{29} (SAA29)
200	25.1 ±1.8	110	S_{71}-AA_{29} (SAA29)

Table 3.1: Conversion of tBA to AA as a function of temperature. Column 1 is the anneal temperature. Column 2 is the percent thickness change before and after annealing. Column 3 is the calculated molecular percent of tBA to AA using the thickness change and equation 1. At 185 and 200 °C, theoretical conversions greater than 100% are attributed to the formation of anhydride groups.

After annealing at 135, 155, and 170 °C, the decrease in thickness corresponds to converting 9, 18, and 50 mol% of tBA to AA. For the fully converted films, the experimental values for the change in thicknesses at 185 °C and 200 °C are in good agreement with the theoretical relative thickness change of 23% for complete conversion. From equation 3.1, the relative thickness changes for films annealed at 185 and 200 °C indicate greater than 100% conversion of tBA due to some formation of acrylic anhydride, AAn. Prior experiments show that acrylic acid can reversibly dehydrate by a condensation reaction with a neighboring acrylic acid under dry conditions to form (AAn) as illustrated in the top of figure 3.1b.[33] From equation 3.1, 100% conversion of tBA to AAn results in a thickness decrease of 33%. Thus, the greater than 23 % decrease in film thicknesses may reflect partial conversion of AA groups to AAn. Because the

EDC/NHS reaction takes place in water, the AAn groups will convert back to AA and preserve the 100% conversion expected at 185 ^{o}C and 200 ^{o}C.

Attenuated total reflectance Fourier transform infrared spectroscopy (ATR-FTIR) was used to determine the composition of films as a function of annealing temperature and these results agree with compositions determined by changes in film thickness given in table 3.1. Figure 3.2 shows FTIR spectra for as-cast StBA (bottom, no anneal) and annealed films corresponding to the film thickness studies in table 1. In the spectra, tert-butyl acrylate is characterized by the C=O stretching peak at 1730 cm^{-1} , CH_3 bending modes at 1394 and 1368 cm^{-1}, and a C-O stretching mode at 1160 cm^{-1}. These peaks appear for films annealed at 135 ^{o}C and 155 ^{o}C. The wavenumbers of the four peaks attributed to tBA are labeled by red arrows and either decrease or disappear at higher temperatures (i.e., above 170 ^{o}C). Denoted by the black arrows, the peaks at 1500 cm^{-1} and 1452 cm^{-1} are associated with phenyl ring bending from the styrene monomer in the copolymer.[34] The styrene peak at 1452 cm^{-1} is used to normalize the spectra.

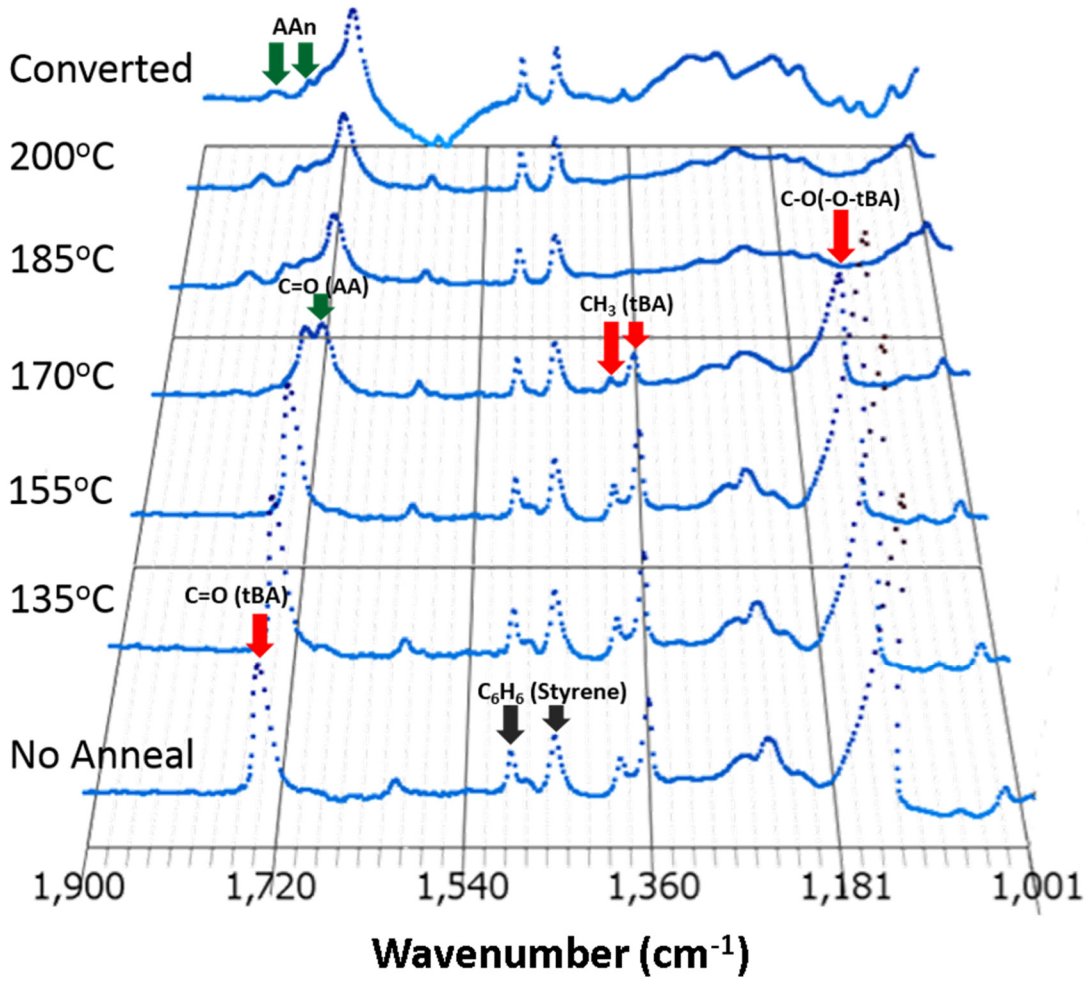

Figure 3.2: Fourier transform infrared absorption spectra of SAA film annealed at various temperatures. Absorbance (au) vs. wavelength as annealing temperature increases (bottom to top) confirms the gradual conversion of tBA domains to AA and AAn. The spectrum marked "converted" represents a sample annealed at 200 °C and incubated 1h in H_2O. Characteristic peak positions are marked with arrows, green arrows indicate a peak which appears during anneal and red arrow indicates a peak which disappear at high temperature. The polystyrene peaks (gray arrows) remain at all temperatures. All data are normalized to the polystyrene peaks observed at 1452 cm^{-1}.

The conversion of tBA to AA is mainly characterized by a red shift, from 1730 cm^{-1} to about 1700 cm^{-1}, due to a change in the local bonding for the carbonyl (C=O) group. As annealing temperature increases to 170 °C, a distinct AA carbonyl peak at 1700 cm^{-1} (green arrow) appears as shown in figure 3.2 (4th line from bottom). Note that the amplitude of the AA carbonyl peak increases as the temperature increases from 170 °C to 185 °C and 200 °C,

consistent with an increase in mole percent of AA. Correspondingly, upon increasing the temperature from 170°C to 185 °C, the amplitude of the tBA carbonyl peak (1730 cm^{-1}) decreases and eventually disappears along with the other characteristic tBA absorption peaks. Thus, the FTIR studies indicate that annealing StBA films at 185 °C for 15h is sufficient to completely convert tBA to AA. Examining the spectra at 170 °C, the relative intensities of the ester peaks associated with tBA and AA are nearly equal, further indicating that the conversion of tBA to AA from FTIR is consistent with the 50% conversion determined by film thickness measurements (table 3.1).

The FTIR spectra of films annealed at 185 °C and 200 °C exhibit a doublet with characteristic peaks near 1800 cm^{-1} and 1760 cm^{-1} (figure 3.2), consistent with the formation of acrylic anhydride. The two peaks associated with AAn are associated with the symmetric and asymmetric stretching modes of the anhydride linkage yielding the unique doublet shown by the two green arrows in figure 3.2. The expected absorption modes are 1806 cm^{-1} and 1762 cm^{-1}, in good agreement with experimental results. Furthermore, previous work shows the appearance of the AAn double after the conversion of tBA to AAn. [33] Thus, films annealed for 15h above 185 °C show a complete conversion of tBA into two species: acrylic acid and acrylic anhydride. For films that contain AAn, the AAn groups can be partially converted back to AA by hydration. To test this hypothesis, a film initially annealed at 200 °C is incubated in DI water for 1h at 50 °C and then dried. Figure 3.2 (top line, converted) shows that the peaks at 1760 cm^{-1} and 1800 cm^{-1} are reduced, consistent with partial rehydration of AAn to form AA.

Whereas S and tBA are both hydrophobic, the conversion of tBA to the hydrophilic AA results in a strong driving force for nanoscale phase separation of the minority hydrophilic AA domains. Evidence for the formation of these domains is the appearance of an AAn preak in films that underwent complete conversion at 185 °C and 200 °C. If all AA groups paired up to

form AAn, the doublet peaks at 1760 cm^{-1} and 1800 cm^{-1} would be larger and the AA carbonyl peak at 1700 cm^{-1} would disappear.[33] The observation of both AA and AAn groups indicate that partial phase separation may occur. The formation of AA domains also explains the previously observed honeycomb-like surface features that appear in SAA29 films swollen in polar solvents.[31]

3.3 NHS activation of AA groups and nanoparticle uptake by SAA13 films

The SAA films contain surface hydroxyl groups that can react with amine groups on the surface of the silica nanoparticles. The swelling of SAA in water and ethanol enhances the hydroxyl group concentration and mobility at the surface. Figure 3.1c shows the processing step where films are exposed to NHS to activate the AA groups so they can form an amide bond with the NPs. During immersion, the SAA films are swollen by ethanol and the degree of swelling determines the ability of NPs to embed and diffuse into the film. As demonstrated later (cf., figure 3.9), NP loading onto or into the film ceases after the NPs jam in the near surface region which blocks further attachment of NPs.

The activation of SAA by NHS and the subsequent attachment of NPs to SAA films is quantified by quartz crystal microbalance with dissipation (QCM). For a SAA13 film with an initial dry thickness of ~80nm, figure 3.3a shows the mass increase during a 4 min exposure to NHS in EtOH. The mass change was fit to an exponential (dashed line) described by $M = M_o\exp(-t/\tau)$. With a χ^2 of 4.2, the fit captures the mass increase with time constant, $\tau = 49 \pm 3.6$ s, and mass saturation, $M_o = 1182$ ng (table 3.2). If NHS forms a monolayer on a smooth SAA film, M_o converts to an NHS areal density of 62 molecules/nm^2. An areal density of 62 molecules/nm^2 is unrealistic because if the AA groups are homogeneous across the surface, the SAA13 film presents only 2.3 COOH groups per nm^2, or roughly 30x less than the monolayer calculation for

the NHS areal density. Thus, a "monolayer" of NHS is not supported by the large mass change. Rather, NHS molecules likely penetrate into the swollen SAA13 film and react with AA groups throughout the film. Using the dry thickness of 80 nm and M_o = 1182 ng, the "bulk" density is 0.8 NHS/nm^3. For comparison, the density of COOH groups in SAA13 is about 3 COOH/nm^3, which suggests that NHS reacts with about 25% of the carboxylic acid groups. As described later, the presence of activated COOH groups below the surface allows for NPs that penetrate into the film to become grafted with SAA chains which can bridge between neighboring NPs to form effective cross-links that arrest diffusion and stop grafting of new NPs.

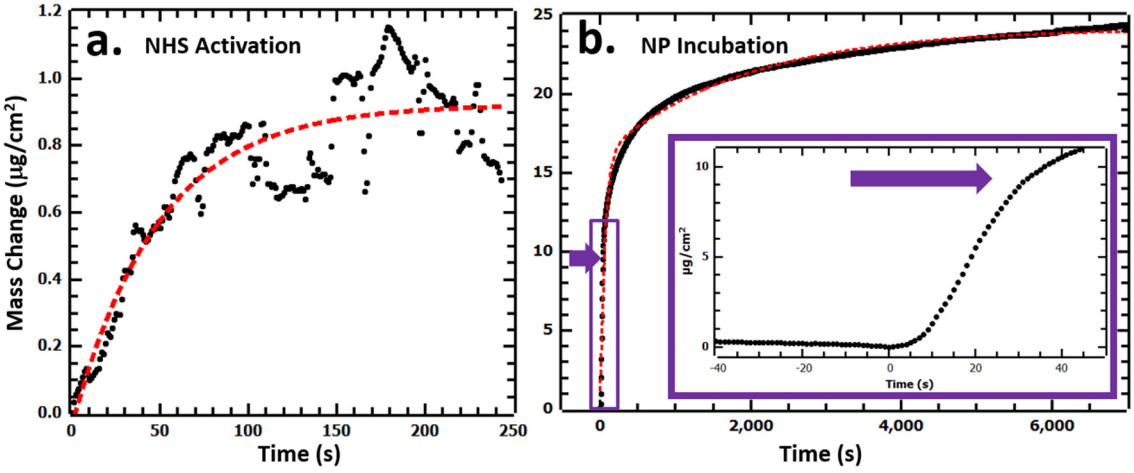

Figure 3.3: QCM data for NHS activation of SAA13 and NP grafting to SAA13 film. a. Mass increase occurs for NHS activation of the SAA_{13} copolymer, Inset: Offset of mass increase is fit well by a single exponential of K = 49±3.6n s^{-1}, and ΔM = 1181.83 ng. **b.** Mass increase shown for NP attachment for a 2h period of time. Inset: zoom of the point of inflection where the NPs enter the QCM chamber and begin to react with the surface. The purple arrow indicates the mass change corresponding to a monolayer of close-packed NPs where the reaction rate becomes limited by NP diffusion.

After activating with NHS, the SAA13 film is exposed to an ethanol solution containing 66 nM of amine functionalized silica NPs. Figure 3.3b shows the mass increase associated with the attachment of the NPs onto/into the SAA13 film. Before measuring the mass due to NP attachment, the SAA13 film is exposed to EtOH for 40 min to equilibrate the swollen film and

normalize the instrument. At t = 0, a solution of NPs in ethanol is introduced into the chamber and within 10 s the NPs begin to attach, as shown in the inset. After 30 s (inset), the rate of attachment slows down as noted by the point of inflection. The arrow denotes the calculated mass of one close packed monolayer of NPs, about 9.5 $\mu g/cm^2$, and corresponds to a reduction in the NP attachment rate (inset, point of inflection). This correlation between the slowing down of the mass change and monolayer formation suggests that subsequent attachment of NPs (> 30s) is inhibited by this initial monolayer of NPs. Further NP attachment (beyond a monolayer) requires NPs of the initial monolayer to sink into the film exposing an active site. Figure 3.3b shows that NP attachment continues to rapidly increase over the next 300 s, suggesting that NP diffusion into the film continues after the initial monolayer formation and that a multilayer structure of NPs forms on/in the film. After about 1000 s, the mass increase slows down and approaches a constant value of about 25.0 $\mu g/cm^2$ at 7000 s (~2h). This mass increase corresponds to an areal density of 1987 NPs/μm^2 (table 3.2), or about 3 close packed monolayers of NPs. For multilayers to form, NPs must diffuse into SAA13 to expose fresh activated sites for NP attachment. However, the packing of the NPs is limited to about 3 equivalent monolayers. QCM studies of NP attachment kinetics suggest that NPs attach to SAA13 films by three stages: (1) an initial stage where NPs rapidly attach to the surface and form a monolayer, (2) a slower middle stage limited by NP diffusion into SAA13, and (3) a late, saturated stage where NPs jam within the SAA film and prevent further attachment of NPs.

The mass increase due to the NPs is fit with a double exponential function (figure 3.3b, dashed red line) with time constants reflecting the initial rapid attachment and slower diffusive stage, namely 60.5 ± 0.5 s and 1865.4 ± 1.1 s, respectively. The initial stage reflects rapid NP grafting via an NHS amine reaction until a monolayer of NPs forms. As the NPs diffuse into the swollen film, NHS activated carboxylic acid groups are exposed at the surface allowing for

subsequent attachment of NPs and an increase in mass as a NP multilayer builds up. The double exponential fit captures the curve much better, $R^2 = 0.98$, than a single exponent, $R^2 = 0.98$. Although the fit is very good, the two-rate constant model does not fully capture the dynamics of NP attachment because other effects such as NP jamming and bridging of NPs by grafted SAA chains likely decrease the diffusivity of NPs non-linearly as loading increases.

	ΔF (Hz)	**ΔM (ng/cm^2)**	**Areal Density**	**τ (s)**
NHS Activation	66.8	1181.8	61.84 /nm^2	49.0 ± 3.6
NP Attachment	1407.9	24919.2	1978 NP/um^2	1865.4 ± 1.1 ; 60.5±0.5

Table 3.2: The frequency change, mass change, areal density, and relaxation time for NHS activation and NP attachment in SAA13 films.

3.4 Hierarchical NP morphology on SAA4, SAA13 and SAA29 Films.

The morphology evolution of NP films is determined by AFM. Figure 3.4 shows the NP surface morphology on SAA4 (top row), SAA13 (middle row), and SAA29 (bottom row) films after 5, 10, 20, 30, 40 and 50 minutes of NP incubation. For SAA4, the NPs form a relatively smooth, uniform layer on the surface of the film. Individual NPs are observed as noted in the insets in the top row. The morphology after 50 min (top row, far right) can be seen more clearly in the expanded image (inset). These particles form a random close packed layer, are partially embedded into the smooth SAA4 film, and have a spacing of about 95 nm. The late-stage morphology of SAA4 films are also shown in Figure 3.5, top row. For the SAA4 film, NP morphology develops by rapid attachment of NPs followed by partial rearrangement on the film surface. Thus, during the late-stage, NPs arrange into a nearly complete monolayer on the SAA4 surface. Because SAA4 contains 96 mole percent of S, the penetration of NPs into the film is likely inhibited by an unfavorable free energy of mixing.

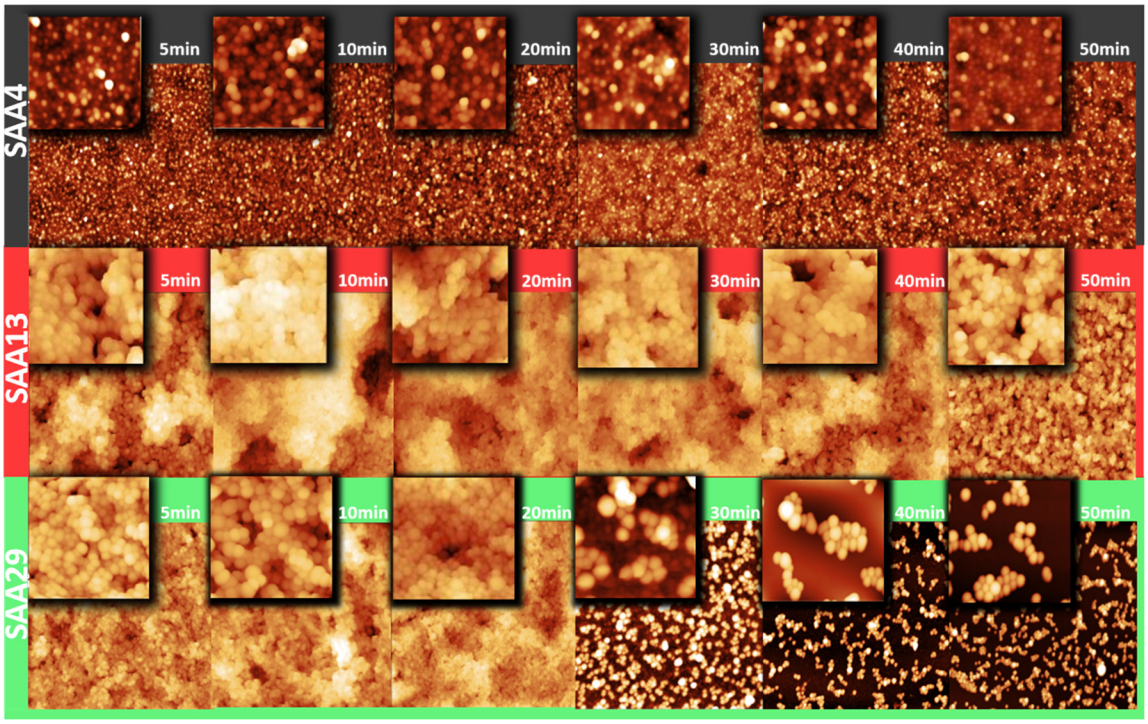

Figure 3.4: Map of surface morphologies with changing AA% and NP incubation time. The rows show three SAA compositions, SAA4, SAA13, and SAA29, while the columns show incubation time of SAA in NH_2-functionalized silica nanospheres in ethanol. Dry AFM images obtained are 5 µm x 5 µm and 1 µm x 1 µm (closeup). Z scales are adjusted to optimize contrast, corresponding roughness values can be seen in figure 3.6.

For the SAA13 films, the surface morphologies are shown in the middle row of figure 3.4. Similar to SAA4, the NPs rapidly attach to the SAA13 film within 5 min. However, compared to SAA4, the NP coverage on SAA13 is much greater because the NPs assemble into a rough multilayered structure. Between 10 min and 40 min, the highly roughened surface persists although the feature size decreases. After 50 min, a porous structure (far right) represents the late-stage morphology of the NP-SAA13 film. This morphological evolution of NPs is consistent with the QCMD results (figure 3.3b), which show an initial rapid attachment, followed by surface reorganization and saturation after 5-10 min, and finally the formation of an approximately 3 monolayer (QCM), multilayer film at long times (> 50 min.). The NP morphology on SAA13

after 50 min (cf. figure 3.4, middle row, far right) is quite similar to the morphology of the NPs on the QCM crystal after removing the film at 2 h. (not shown).

The surface morphologies of SAA29 films are shown across the bottom row of figure 3.4. For SAA29, tBA has been completely converted to AA and therefore SAA29 has the highest acrylic acid content and is more hydrophilic than SAA4 and SAA13 films. Initially, NP attachment is rapid and the morphology is similar to the SAA13 system, where the surface roughness reaches a maximum at 10 min before decreasing at longer times (c.f., Fig. 6). The decrease in surface roughness is more rapid for SAA29 than SAA13, and stops after 40 min. The late stage morphology (far right) shows clusters of NPs on the surface of a relatively smooth SAA29 film. These aggregates are elongated, homogeneously spaced, and contain on the order of 10 NPs. Determined from surfaces corresponding to 40, 50 and 70 min, the average surface coverage of clusters is 26.64 ± 1.2 %.

Figure 3.5 shows the AFM topography images (1 μm x 1 μm) of the late-stage morphology for the SAA4, SAA13, and SAA29 films (right column) and their corresponding line scans (left column) after 70 min. For the SAA4 film, the terminal morphology is a sub-monolayer of NPs. The NPs are uniformly distributed with a spacing of about 95.3 ± 3.8 nm which was determined by a fast Fourier transform of the topography. The arrangement of NPs suggests that the surface between NPs is hydrophobic or NPs are prevented from forming a complete monolayer due to excluded volume. The line scan shows feature heights on the order of 25 nm, roughly the radius of the NP, indicating that the NPs are partially embedded into the SAA4 film. For the SAA13 film, the NPs form a porous multilayer with features up to ~ 100 nm indicative of multiple layers of NPs. For the SAA29 film, discrete aggregates are observed on the surface of the film and likely extend below the surfaces. The line scan is consistent with a discrete “pile” of

NPs with a height on the order of a few NPs. By comparing this morphology at 70 min with figure 3.4 at t = 40 and 50 min, the aggregates appear to be stable.

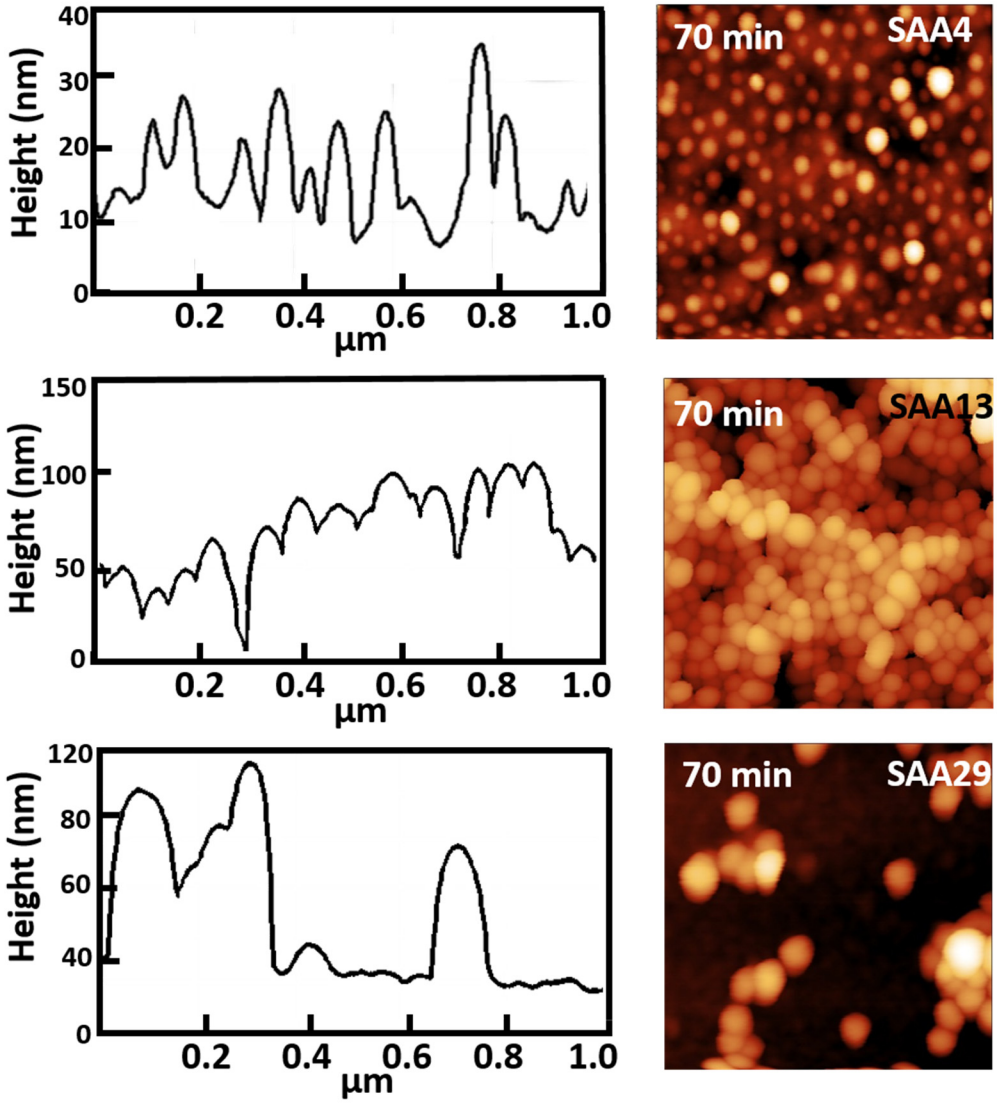

Figure 3.5: Late-stage morphology of SAA4 (top), SAA13 (middle), and SAA29 (bottom) films. On the right 1µm x 1µm AFM topographic images show representative morphology of films incubated for 70 min in NP solutions. At 70 min the morphology is no longer changing, i.e. "late-stage". On the left cross sections of the film show a representative Z-scale (height) for each film indicating SAA4 is a monolayer, SAA13 is a porous multilayer, and SAA29 shows aggregates of NPs.

Figure 3.6 shows the RMS roughness for the SAA4, SAA13, and SAA29 films for immersion times up to 70 min. The roughness values are determined from 25 AFM images (1

μm x 1 μm) such as those in figure 3.4. The roughness of the SAA4 film (black circles) is consistently lower than that of the SAA13 and SAA29 films. Initially, the roughness increases to a maximum value of 30 nm between 10 and 20 min, decreases slightly after 20 min and then approaches a constant value of 10 nm after 70 min. The roughness versus time is consistent with AFM topography images (1um x 1 um) showing that the terminal morphology of SAA4 is relatively smooth because the NPs partially embed into the film (cf., figure 3.5). As shown inset in figure 3.6, Fourier transforms of AFM images of SAA4 and SAA13 films at 10 min and 70 min demonstrate that planar hexagonal-like packing of NPs is unique to the SAA4 at 70 min. For SAA4, the circular and hexagonal patterns at 10 min and 70 min suggest that NPs are randomly organized at 10 min, reorganize during intermediate times, and become ordered by 70 min. This behavior is mirrored by the roughness, which reaches a maximum at 10 min before slowly decreasing towards its lowest value, consistent with a smooth monolayer. Thus, the hexagonal packing of NPs at 70 min is consistent with the slow kinetics of NP rearrangement in the SAA4 film compared to the SAA13 and SAA29 films and the particle spacing of 95 nm suggests that NPs repel one another.

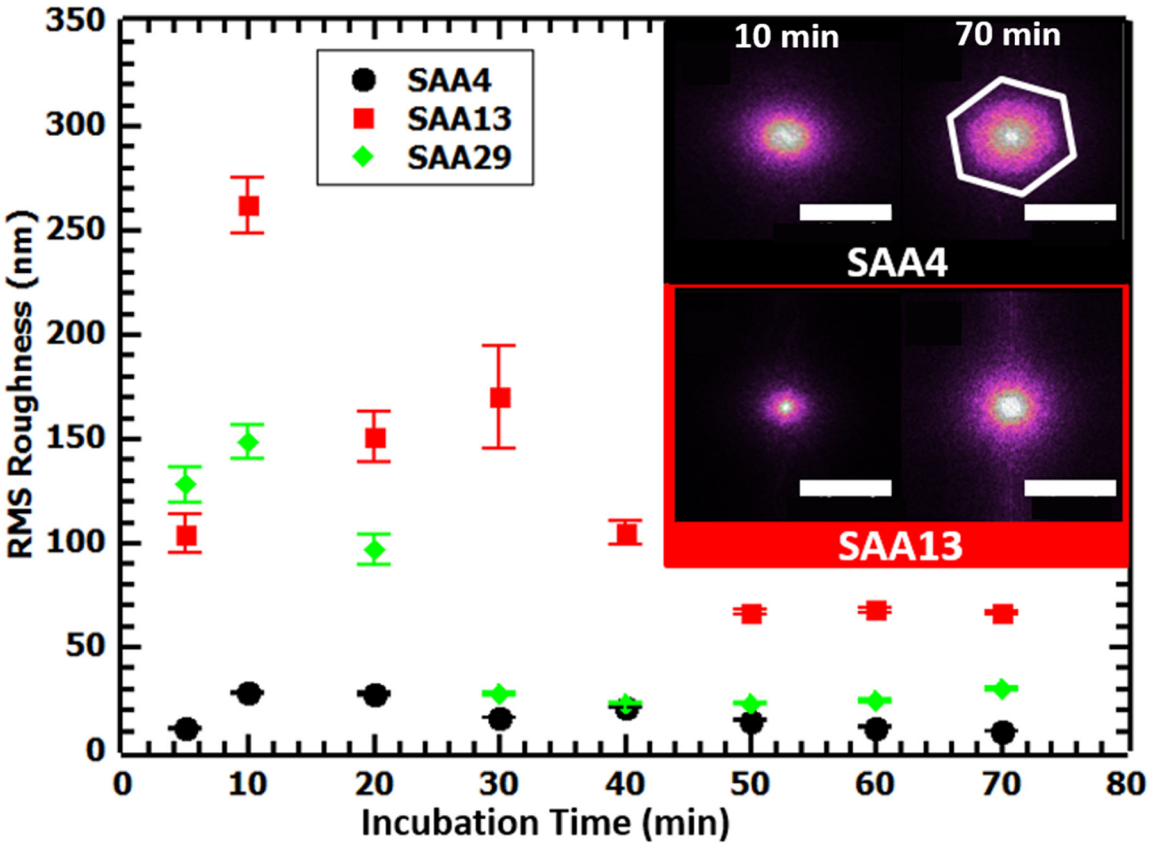

Figure 3.6: RMS roughness of SAA4, SAA13, and SAA29 films. Route mean square of AFM image height distribution (roughness) of nanocomposite topographies (figure 3.4) at film compositions SAA4, SAA13, SAA29. RMS roughness and standard deviation comes from 25 individual 1um x 1um panels in a single 5um x 5um image. **Inset:** Fast-Fourier transforms of 1um x 1um AFM topographic images of SAA4 and SAA13 surfaces at early (10 min) and late (70 min) incubation times. The NPs grafted to SAA4 develop hexagonal symmetry visible after 70 min leading to the appearance of the hexagon in the transform(outlined). Order is not observed in the SAA13 or SAA29 composites. FFT scale bars are 40 mm^{-1}

The roughness (red squares) of the SAA13 film is consistently larger than the SAA4 and SAA29 films and reaches a maximum value of 265 nm at 10 min. Between 10 and 50 min, voids on the surface are filled in by NPs resulting in a decrease in roughness to 70 nm consistent with the porous morphology which persists thereafter. Similarly, the RMS roughness of the SAA29 film reaches a maximum value of 150 nm at 10 min and then decreases towards a constant value of 25 nm by 30 min. This trend is consistent with the "aggregate" morphology shown in figure 3.4 (bottom right). In summary, for all films, the roughness initially increases, reaches a

maximum value, and then decreases towards a constant value. The roughness approaches a constant value most rapidly for SAA29 and most slowly for SAA4 and the order of roughness is: SA13 > SA29 > SAA4.

3.5 Contact angle and transparency of SAA films.

The hierarchical morphologies are expected to dictate the contact angles and optical properties of the SAA4, SAA13 and SAA29 films. Figure 3.7a shows the water contact angles as a function of incubation time. SAA29 and SAA4 are the most hydrophilic and hydrophobic films and therefore water contact angles on these surfaces should be lowest and highest, respectively. However, figure 3.7a shows that SAA4 exhibits a similar contact angle, 111^{o}, as SAA29, 112^{o}, at 10 min. The similar wetting is due to roughness differences between the surfaces. Whereas SAA4 films are relatively smooth (roughness ~ 30nm), the SAA29 films are relatively rough (150 nm) and high contact angles result from Cassie-Baxter type hydrophobicity resulting from air entrapment. Furthermore, the contact angle of SAA13 is greater than SAA29 which exhibits values intermediate between SAA13 and SAA4. This trend is attributed to the multi-scale roughness of SAA13 films (cf. figure 3.4, middle row). Note that the contact angles follow the same trend as the RMS roughness shown in figure 3.6 with the exception of an increase in contact angle after 50 min for SAA13 and SAA29 films, suggesting an apparent recovery of hydrophobicity. SAA13 films can exhibit superhydrophobicity (c.a. > ~160^{o}) whereby water droplets are nearly spherical as shown in the inset (red box). For times greater than 30min, SAA4 films exhibit a contact angle less than that of neat PS (ca ~ 90^{o}) which is a potential indicator of Wenzel type wetting whereby the contact angle is determined by surface composition without air entrapment. These contact angle studies are consistent with prior reports in which NP decorated surfaces undergo a wetting transition between Wenzel and

Cassie-Baxter type wetting.[31] In the present study, high contact angles are achieved by exploiting the length scale of the porous NP structure on SAA13 films.

For SAA4, SAA13, and SAA29 films, figure 3.7b shows the average absorbance across the IR and visible spectrum, namely between 350 nm and 800 nm. The standard deviation reflects the difference between the lowest and highest absorbance values in each individual spectrum. A dramatic difference in transparency is observed between the opaque SAA13 and clear SAA4 films as illustrated by the photographs in the inset of figure 3.7b. A comparison between RMS roughness (figure 3.6) and absorbance (figure 3.7b) in the context of the morphology (figure 3.4) at late times ($t > 40$ min) indicates that film transparency is mainly determined by large scale nanoparticle aggregation within the film. The clustering of NPs into large (μm scale) aggregates is evident for SAA13 at $t < 50$ min and SAA29 films at all times. Since SAA13 films (red squares) exhibit the greatest roughness (figure 3.6), SAA13 films should also exhibit the highest absorbance. However, SAA13 absorbs the most only between 10 and 40 mins. At 50 min, the absorbance of SAA29 films (green diamonds) becomes greater than SAA13. Because the surface roughness of SAA13 is proportionally larger than SAA29, the greater absorbance by SAA29 is attributed to NP aggregation within SAA29 leading to strong scattering. In contrast, the NPs in SAA4 and SAA13 are densely packed; however these NPs are isolated (either individually or in a bicontinuous structure) and scatter visible light less than films consisting of an aggregate morphology. Scattering studies demonstrate the importance of controlling NP aggregation within the films and the bicontinuous structure (figure 3.4, middle, 50 min) is the best candidate for generating non-wetting, non-scattering surfaces.

The low scattering by SAA4 films (black circles) at all times indicates that NPs neither aggregate on the surface nor within the film. Although the morphology at early times ($t < 30$ min, figure 3.4) is rougher than that of SAA29 at later times ($t > 30$ min), the low absorption

values of SAA4 compared to SAA29 suggest that NP aggregation is limited in SAA4 films. Although SAA4 and SAA29 are equally rough at 40 min, SAA29 has higher absorbance due to the NP aggregates embedded in the film. At late times, the hexagonally packed monolayer on SAA4 has an average center-to-center NP spacing of 95.3 ± 3.8 nm (cf. figure 3.5) consistent with isolated particles. In contrast to SAA13 and SAA29 films, the low optical scattering from SAA4 films indicates a thermodynamically stable monolayer of NPs.

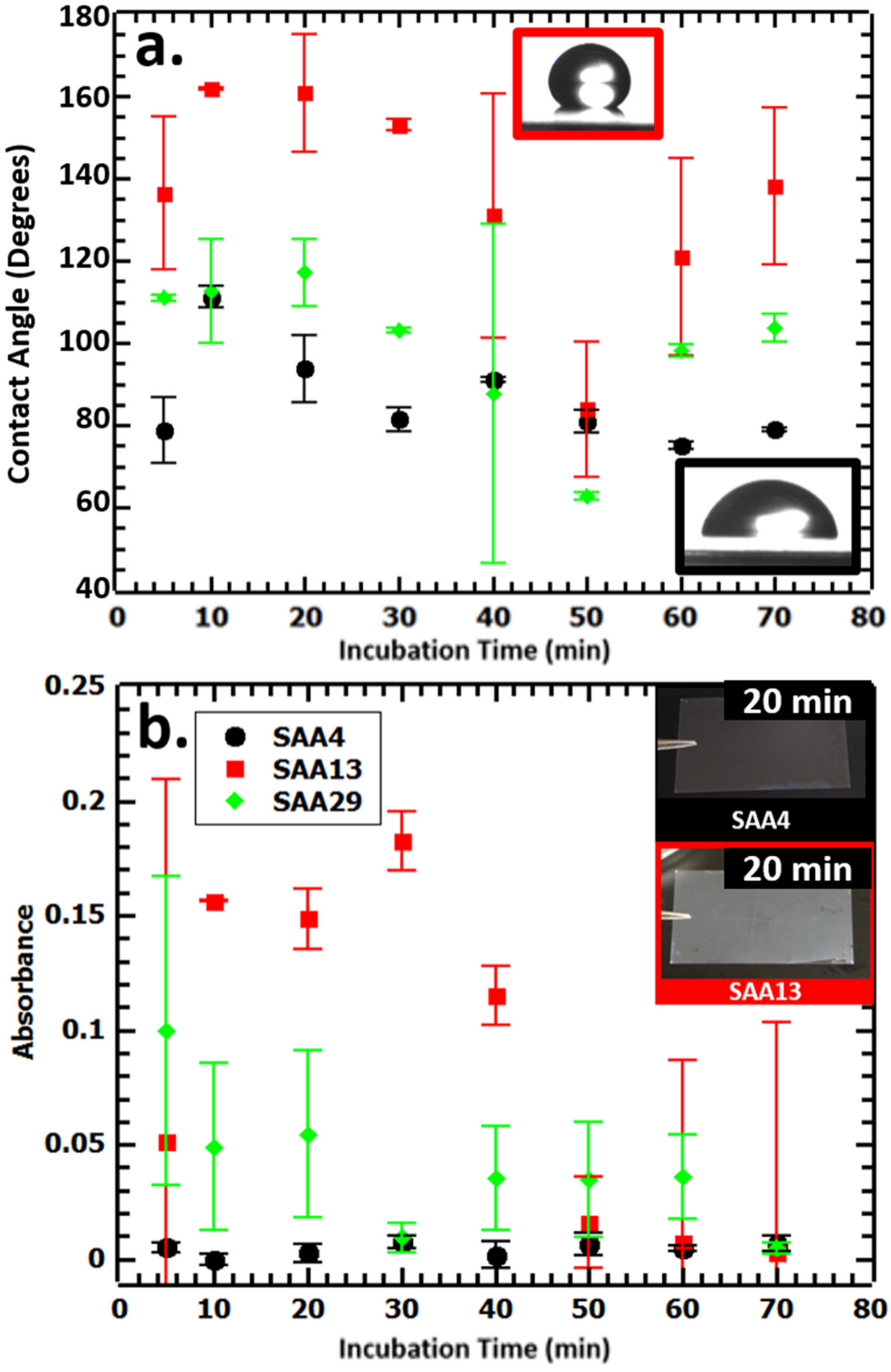

Figure 3.7: Contact angle and absorbance of SAA4, SAA13, and SAA29 films. a. Average contact angle of water on the films and standard deviation determined from at least two different areas on the film. **Inset:** Water atop SAA13 treated for 20 min (red) and SAA4 treated for 70 min

(black) highlights dramatic difference in wettability observed due to roughness differences. **b.** Average absorbance over the visible and UV spectrum (wavelengths 300 nm – 800 nm) is plotted as an indicator of the transparency of the films. **Inset:** Photographs showing significance of 15% absorbance vs 1%.

3.6 Mechanism of NP attachment and diffusion into SAA.

The observation that NPs can penetrate into SAA13 films but remain on the surface of SAA4 films implies that the thermodynamics of NP sinking in SAA4 is unfavorable. NP loading into a film is governed by the interaction energy between NP and polymer matrix. As described by equation 3.2, NP sinking is determined by a balance between an entropic penalty associated with polymer chain stretching upon incorporation of NPs, which pushes NPs out of the film, and an enthalpic term governed by NP-polymer interactions.[26] The second term is energetically favorable if the interaction parameter, χ, is negative indicating a favorable heat of mixing between polymer and NP. For the NH_2-grafted NPs, the interaction parameter between polymer and NP can be approximated from the average composition of SAA4, SAA13 and SAA29 (S, tBA, and AA) that interacts with the NP (i.e.χ_{NH_2-SAA}). Whereas the interaction between the NP and styrene or tBA is unfavorable, the interaction between NP and AA (COOH) is favorable. Therefore, χ decreases as the fraction of AA increases in SAA. Thus, from a purely enthalpic prospective, the sinking and incorporation of NPs into the copolymer film is least favorable for SAA4 and most favorable for SAA29.

The interaction energy per k_bT per unit volume, F_{int}, depends on the number of nanoparticles, n_p, volume fraction of NPs, φ_{NP}, the NP radius, R_p, degree of polymerization of SAA, N, and statistical segment length of SAA, l.

$$F_{int} \cong n_p(1-\varphi_{NP})\left(\frac{R_p}{l}\right)\frac{3{R_p}^2}{2Nl^2} + \chi\varphi_{NP}\left[\frac{l}{R_p}\right](1-\varphi_{NP}) \quad (3.2)$$

The effect of SAA swelling can be incorporated into F_{int} through entropic (first term equation 3.2) changes associated with increases in radius of gyration, $r_g = N^{1/2}l$, of SAA associated with swelling of the SAA during exposure of the film to ethanol during the NP grafting reaction. The entropic term of F_{int} represents the thermodynamic resistance of the polymer to NP sinking associated with polymer chain stretching. The entry of NPs is promoted by solvation of SAA during the grafting reaction because the entropic penalty for NP incorporation is reduced. Namely, the entropic penalty decreases during swelling (solvation) by ethanol because chains swell and r_g increases. For a sollen polymer (i.e., good solvent), entropy depends on the volume fraction of solvent, φ_s.[35] Equation 3.3 shows that r_g increases as solvent concentration,

$$r_g \cong lN^{1/2}(1-\varphi_s)^{-(2\nu-1)/(6\nu-2)} \qquad (3.3)$$

increases, promoting NP embedding as the mol% of AA increases in the SAA films. [36] The Flory exponent, ν, is 0.588 for a good solvent.[32] Relative to their collapsed size (i.e., dry), end-grafted AA brushes can swell by five times their size in low ionic strength solutions at pH 4.[37] However, this relatively large swelling only reduces the entropic penalty by about 1.5x suggesting that polymer solvation alone cannot be responsible for the transition between a thermodynamically stable interfacial monolayer of NPs on SAA4 and the diffusion of NPs into SAA13 and SAA29.

The diffusion of NPs into films will depend on the amount of swelling and therefore the acrylic acid content. As SAA films swell and chain mobility increases, the viscosity, η, of the film decreases, which leads to enhanced diffusion of NPs into the film. For a simple viscous medium, the diffusivity of a sphere with radius R_p is given by the Stokes-Einstein diffusion equation, 4a.[38-40]

$$D \cong \frac{k_B T}{6\pi\eta_s R_p} \qquad (3.4a)$$

$$D(\varphi_s) \cong \frac{k_B T}{6\pi\eta_s R_p}\left(\frac{{N_e}^2}{N^3}\right)(1-\varphi_s)^{-3.93} \qquad (3.4b)$$

When $R_p > R_g$, as is this study, the Stokes-Einstein relation accurately captures NP diffusion in a polymer melt.[38] In addition the the molecular weight of SAA, the viscosity also depends on the swelling of the SAA by ethanol or water.[30,37] By combining equation 3.3 with equation 3.4a for a good solvent, NP diffusion is related to the volume fraction of solvent in SAA.[35,36] As shown in equation 4b, NP diffusion also depends on the entanglement degree of polymerization, N_e, which determines network size, as well as the viscosity of the medium, η_s. For a PS melt, $N_e \cong 130$ and the network size is about 8nm.[41]

Nanoparticle diffusion increases as the volume fraction of solvent in the film increases. For the most hydrophilic case, namely pure AA, the film will contain 80 vol% of solvent, assuming 5x swelling.[37] Using equation 3.4b, figures 3.8a, b, and c show NP diffusion coefficients in SAA films as a function of mole percent AA, SAA molecular weight increase (M_W/M_W^o), and radius of diffusing particle (or aggregate), respectively. Calculations assume that SAA swelling is proportional to the mole percent of AA, for example φ_s = 0.232 for SAA29. Figure 3.8a shows that the diffusion coefficient increases as the mol% of AA increases. The black dashed line is the plot of equation 3.4b where φ_s is directly proportional to %AA. The colored circles in figure 3.8a show where SAA2, SAA4, SAA13, and SAA29 fall on the curve. The diffusion coefficient increases by about 3x as the mole percent of AA increases from 4 to 29. The three fold faster diffusion in SAA29 than SAA13 and SAA4 fits the relative time the roughness of the SAA4, SAA13, and SAA29 films reach their respective late-stage morphologies. (cf. figure 3.6). Indicating that SAA swelling impacts the rate of morphology evolution in the SAA films.

Figure 3.8b simulates the reduction in NP diffusion coefficient resulting from the grafting of SAA chains to the nanoparticles. Attachment of SAA chains to the surface of the NP

(illustrated in figure 3.8b, inset) dramatically increases the average molecular weight of the SAA chains by cross-linking them together. This leads to an increase of the number of entanglements per chain proportional to the increase of the average molecular weight, M_w, of SAA chains linked together in the film. The molecular weight increase raises the viscosity and reduces the diffusion coefficient by increasing N in equation 3.4b. In figure 3.8b, the diffusion coefficient is plotted versus the reduced molecular weight (M_W/ M_W^o) where M_W^o is 98300 g/mol. At this SAA molecular weight, nanoparticle diffusion is governed by polymer mobility (i.e. polymers diffuse faster than NPs). Consequently, increasing entanglements reduces polymer and NP diffusivity within the film. A 2x increase in chain length yields a ~10x reduction in NP diffusion coefficient and the effect scales with AA%. The diffusion reduction changes more rapidly for the SAA29, and less rapidly for the SAA4 (slopes figure 3.8b).

Figure 3.8c shows how the diffusion coefficient decreases as the nanoparticle (or aggregate) size increases. Although $2*R_p$ is 45 nm for NPs grafted with SAA chains (inset middle), SAA chains can graft to neighboring NPs within the film and cross-link two NPs together (bridging). Bridging increases R_P as NPs cluster together and slows down due to an increase of R_P in equation 3.4b. Upon bridging, the diffusivity decreases by a factor of 2 for a 2 fold increase in R_P. Furthermore, for the effective NP cluster size to double, NPs must bridge with roughly 4 neighbors (inset right). Grafting of the SAA chains to the surface of the NP has little effect on its size (i.e. $r_g << R_P$). Bridging is therefore significantly less effective in reducing NP diffusion than the viscosity changes associated with polymer-NP grafting (figure 3.8b). The more solvated the film, the greater the magnitude of the reduction of the diffusion coefficient as noted by the steeper slope of the SAA29 (green curve) compared to the SAA13, SAA4, and SAA2 films.

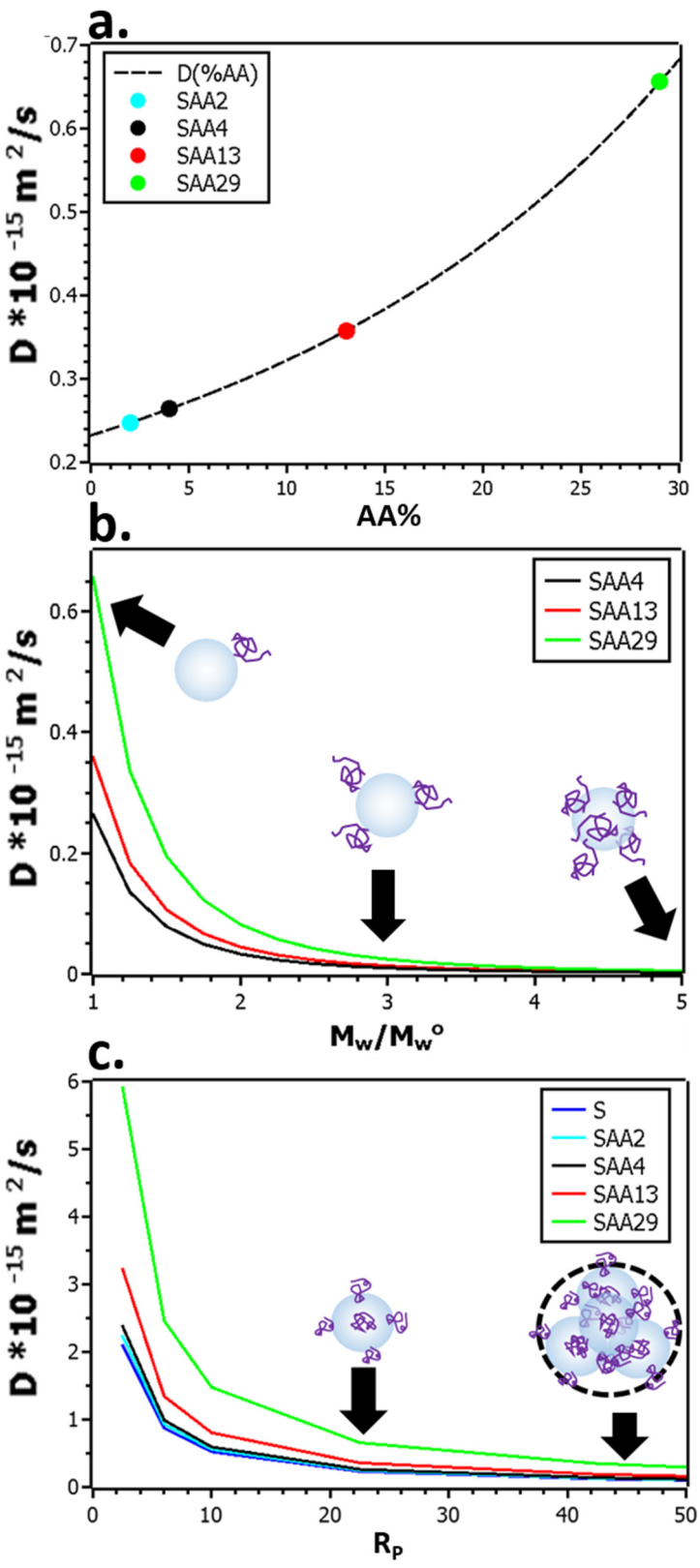
a.
D(%AA)
SAA2
SAA4
SAA13
SAA29
D *10 -15 m 2/s
AA%
b.
SAA4
SAA13
SAA29
D *10 -15 m 2/s
Mw/Mw°
c.
S
SAA2
SAA4
SAA13
SAA29
D *10 -15 m 2/s
Rp

Figure 3.8: Diffusion Enhancement by Solvation of SAA Films. a. The predicted diffusion coefficient of D = 45 nm diameter NPs within SAA is plotted assuming films swelling scales proportional to AA%. Data points indicate AA% used in this study, SAA2 – SAA29. Black dotted line is equation 3.4b for generalized AA%. **b.** Effect of increasing the average molecular weight of the polymer on the diffusivity of 45 nm NPs. This simulates the slowing down in diffusivity by SAA chains grafting to NPs during incubation leading to an effectively larger entanglement molecular weight. Inset illustrates that polymer mobility dictates NP diffusivity as shown by diffusion constant before NPs are grafted to polymer and after an average of 5 SAAs are grafted to each particle on the NP mobility. Arrows point to equivalent calculated diffusivity and predict dramatic changes. **c.** Effect of NP size on diffusivity showing effect of polymer bridging on NP diffusion. Inset illustrates clustering of 5 NPs is required to effectively double diffusing size and halve diffusivity. Calculations are made for M_w^o = 98300, and D_{NP} = 45 nm using equation 3.4b as a basis. Illustrations not to scale.

3.7 Mechanism of morphology evolution in SAA-NP composite films: discussion.

Figure 3.9 summarizes the mechanisms governing NP attachment onto and incorporation into SAA films by highlighting the late-stage morphologies for SAA-NP composites. After 70 min the SAA4-NP film morphology is characterized by a monolayer of partially embedded nanoparticles as shown in figure 3.9a. The schematic shows that the SAA4 film is minimally swollen because the polymer is very hydrophobic and EtOH solubility is very low. Because of the unfavorable interaction between the NP and SAA4, namely χ_{NH_2-SAA4}, NPs are thermodynamically limited to embed in the surface of the SAA4 film. A NP monolayer at the polymer-liquid interface minimizes the unfavorable interaction between SAA4 and the solvent. Furthermore, NP dynamics within the film are slow because the low solubility of SAA4 in EtOH imparts a high viscosity of SAA4. Thus, even if thermodynamically favored, penetration of the NPs into the film is slow and the interface becomes jammed. The morphology shown in 3.9a represents the near-equilibrium morphology for SAA4.

Figure 3.9b illustrates the late stage morphology of SAA13-NP composites which form a porous near-surface, multilayer of NPs. Relative to SAA4-NP, the mole fraction of AA is larger resulting in greater solvation of SAA13 by EtOH and more favorable interactions, namely, $\chi_{NH_2-SAA13} < \chi_{NH_2-SAA4}$. Consequently, NP diffusion is faster and NPs can penetrate into

SAA13. A highly roughened multilayer of NP appears within minutes (figure 3.4 middle and the late-stage morphology that appears after 50 min is a porous multilayer approximately 3NPs thick as determined by QCM (figure 3.3b). These highly roughened structures exhibit super hydrophobic as previously described (cf. figure 3.7a).

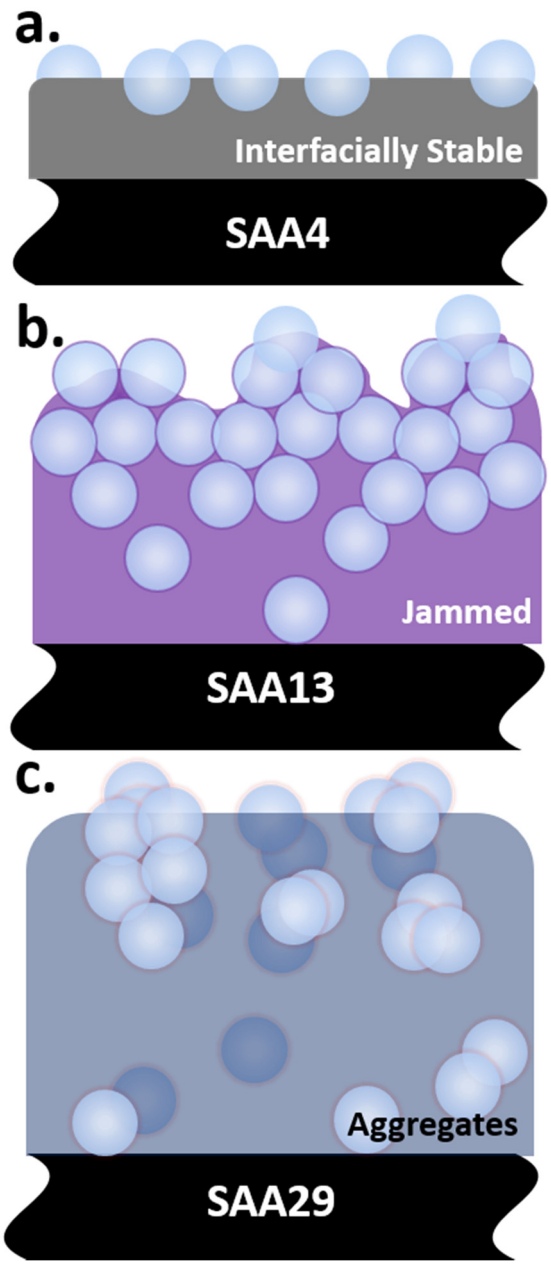

Figure 3.9: Schematic of late-stage morphologies observed in SAA films of varying composition. a. SAA4 shows an interfacially stable monolayer of NPs which pack in a roughly hexagonal fashion on the surface. **b.** SAA13 shows a porous highly roughened jammed multilayer of NPs at long incubation times. **c.** SAA29 shows embedded aggregates of NPs.

Figure 3.9c shows SAA29-NP composites which form an "aggregated" morphology at incubation times longer than 40 min. Aggregation of NPs is attributed to the relatively fast kinetics of NPs in highly swollen, lower viscosity, SAA29. Multilayers of NPs initially incorporated into SAA29 (figure 3.4 bottom row) evolve into domain-like clusters of NPs at late times. These clusters are located within the SAA29 because the high AA fraction allows NPs readily penetrate into the SAA29, i.e., $\chi_{NH_2-SAA29} < \chi_{NH_2-SAA13}$. Due to the high mole percent of AA, SAA29 chains can bridge between NPs and nucleate aggregates of NPs as illustrated in figure 3.9c.

3.8 Conclusion

In this chapter, the morphology and dynamics of NP attachment to SAA random copolymer films are interrogated. Control over the fraction of AA in the random copolymer from 2 to 29% enables the creation of diverse hierarchical roughness morphologies. QCM shows that NP attachment follows a multi-step reaction pathway involving both NP grafting and film reorganization in a multi-rate process. When submersed in EtOH prior to NP incubation, SAA films swelling increases as the percent of AA increases. As the swelling of SAA chains increases the entropic cost of NP incorporation into the SAA film decreases. The reduction in entropic penalty in combination with a more favorable enthalpic attraction between NPs and SAA leads to the entry of NPs into the SAA film at AA compositions greater than 4%. The diffusion of NPs into the polymer becomes faster with polymer solvation as the effective viscosity of the polymer decreases by as much as ~7000 fold. Consequently, at higher fractions of AA, nanoparticle grafting densities rapidly exceed a monolayer and the surface roughness of the films approaches a constant value faster at larger fractions of AA where dynamics are faster.

Between SAA4 films and SAA29 films, the surface topography exhibits a large range of roughness values increasing from less than 10 nm to 300 nm. Control over NP aggregation in SAA films is achieved at SAA13, where a balance between maximum surface roughness and minimum surface scattering leads to the creation of super hydrophobic, bicontinuous SAA13-NP composite films. A range of contact angles between 70^{o} and 170^{o} is achieved for the different morphologies shown in figure 4 and tunable hydrophobicity may facilitate using of these surfaces as non-fouling coatings in a wide array of applications.

3.9 References

1. Schumacher JF, Aldred N, Callow ME, Finlay JA, Callow JA, Clare AS, Brennan AB, Species-specific engineered antifouling topographies: correlations between the settlement of algal zoospores and barnacle cyprids, *Biofouling*, **2007**; 1-11.
2. Baum C, Meyer W, Stelzer R, Fleischer L-G, Siebers D, Average nanorough skin surface of the pilot whale: considerations on the self-cleaning abilities based on nanoroughness, *Marine Biology* **2002** 140: 653-657. N
3. Koch K, Bhushan B, Jung YC, and Barthlott W, Fabrication of artificial Lotus leaves and significance of hierarchial structure for superhydrophobicity and low adhesion, *Soft Matter*, **2009**, 5, 1386-1393.
4. Scardino AJ, Hudleston D, Peng Z, Paul NA, de Nys R, Biomimetic characterization of key surface parameters for the development of fouling resistant materials, *Biofouling*, 25, 1, 2009, 83-93.
5. Bixler GD, Bhushan B, 2012. Biomimetics: lessons from nature—an overview. *Philos. Trans. R. Soc. A* 370:2381-2417
6. Milijkovic N, Enright R, Wang EN, Dynamics and Heat Transfer during Condensation on Superhydrophobic Nanostructured Surfaces, *ACS Nano*, 6,2, **2012**, 1776-1785.
7. Xu QF, Wang JN, Sanderson KD, Organic-Inorganic Composite Nanocoatings with Superhydrophobicity, Good Transparency, and Thermal Stability, *ACS Nano*, **2010**, 4, 4; 2201-2209.
8. Bravo, J, Zhai L, Wu Z, Cohen RE, Rubner MF, Transparent Superhydrophobic Films Based on Silica Nanoparticles, *Langmuir* , 23, **2007**, 7293-7298.
9. Asmatulu R, Ceylan M, Nuraje N, Study of Superhydrophobic Electrospun Nanocomposite Fibers for Energy Systems, *Langmuir*, 27, 2, **2011**, 504-507.
10. Caporizzo MA, Sun Y, Goldman YE, Composto RJ, Nanoscale topography mediates the adhesion of F-actin, *Langmuir*, 28,33, **2012**, 12216-12224.
11. Schmidt G, Malwitz MM, Properties of polymer-nanoparticle composites, *Current Opinion in Colloid and Interface Science,* 8, 1, **2003**, 103-108.
12. Galvin CJ, Genzer J, Applications of surface-grafted macromolecules derived from post-polymerization modification reactions, *Progress in Polymer Science* 37, 7, **2012**, 871-906.

13. Stuart MAC, Huck WTS, Genzer J, Muller M, Ober C, Stamm M, Sukhorukov GB, Szleifer I, Tsukruk VV, Urban M, Winnik F, Zauscher S, Luzinov I, Minko S, Emerging applications of stimuli-responsive polymer materials, *Nature Materials*, 9, **2010**, 101-113.
14. Giesa T, Buhler MJ, Nanoconfinement and the Strength of Biopolymers, *Annual Review of Biophysics*, 42, **2013**, 651-673.
15. Moniruzzaman M, Winey KI, Polymer nanocomposites containing carbon nanotubes. *Macromolecules*, 39, **2006**, 5194-5205.
16. Stankovich S, Dikin DA, Dommett GHB, Kohlaas KM, Zimney EJ, Stach EA, Piner RD, Nguyen ST, Ruoff RS, Graphene-based composite materials, *Nature*, 442, **2006**, 282-286.
17. Hore, MJA, Frischknecht, AL, Composto, RJ, Nanorod Assemblies in Polymer Films and Their Dispersion Dependent Optical Properties, ACS Macro Letters, **2012**, 1, 115-121.
18. Clapham PB, Hutley MC, Reduction of lens reflexion by the 'Moth Eye' principle. *Nature* 244, **1973**, 281-282.
19. Rittigstein P, Priestley RD, Broadbelt LJ, Torkelson JM, Model polymer nanocomposites provide an understanding of confinement effects in real nanocomposites, *Nature Materials*, 6, **2007**, 278-282.
20. White SI, Mutiso RM, Vora PM, Jahnke D, Hsu S, Kikkawa JM, Li J, Fischer JE, Winey KI, Electrical Percolation Behavior in Silver Nanowire-Polystyrene Composites: Simulation and Experiment, *Advanced Functional Materials*, 20, 16, **2010**, 2709-2716.
21. Balazs AC, Emrick T, Russell TP, Nanoparticle Polymer Composites: Where Two Small Worlds Meet, *Science*, 314, **2006**, 1107-1110.
22. Wenzel RN, Resistance of solid surfaces to wetting by water, *Ind Eng Chem,* **1936**, 28: 988-994.
23. Cassie ABD, Baxter S, Wettability of porous surfaces, *Transactions of the Faraday Society,* **1944**, 40: 546-551.
24. Quere D, Wetting and roughness, *Annual Reviews of Materials Research,* **2008**, 38; 71-99.
25. Natarajan B, Li Y, Deng H, Brinson LC, Shadler LS, Effect of Interfacial Energetics on Dispersion and Glass Transition Temperature in Polymer Nanocomposites, *Macromolecules*, 46, **2013**, 2833-2841.
26. Ginzburg, V.V., Influence of Nanoparticles on Miscibility of Polymer Blends. A Simple Theory, Macromolecules **2005**, 38, 2362-2367.
27. Thompson, RB, Ginzburg, VV, Matsen, MW, Balazs, AC, Predicting the Mesophases of Copolymer-Nanoparticle Composites, Science, **2001**, 292, 2469-2472.
28. Jang SG, Kim BJ, Hawker CJ, Kramer EJ, Bicontinuous Block Copolymer Morphologies Produced by Interfacially Active, Thermally Stable Nanoparticles, *Macromolecules*, 44,**2011**, 9366-9873.
29. Roach P, Shirtcliffe NJ, Newton MI, Progress in superhydrophobic surface development, *Soft Matter*, 4, **2008**, 224-240.
30. McConnell, M. D.; Yang, S.; Composto, R. J. Covalent Nanoparticle Assembly onto Random Copolymer Films, *Macromolecules* **2009**, 42, 517-523.
31. McConnell, M. D.; Yang, S.; Composto, R. J. Tunable Wetting of Nanoparticle-Decorated Polymer Films, *Langmuir* **2009**, 25(18), 11014-11020.
32. Brandrup, J.; Immergut, E. H. *Polymer Handbook*, 3rd ed.; John Wiley & Sons: New York, **1989**.
33. La HY, Stoykovich MP, Park SM, Nealey PF, Directed Assembly of Cylinder-Forming Block Copolymers into Patterned Structures to Fabricate Arrays of Spherical Domains and Nanoparticles, *Chem. Mater.***2007**, 19, 4538-4544.

34. Liang CY, Krimm S, Infrared Spectra of High Polymers. VI. Polystyrene, *Journal of Polymer Science,* XXVII, **1958**, 241-254.
35. Cai, LH, Panyukov, S, Rubinstein, M, Mobility of Nonsticky Nanoparticles in Polymer Liquids, Macromolecules, **2011**, 44, 7853-7863.
36. Rubinstein, M, Colby, RH, Polymer Physics; Oxford University Press: New York, **2003**.
37. Wu T, Gong P, Szleifer I, Vlcek P, Subr V, Genzer J, Behavior of Surface-Anchored Poly(acrylic acid) Brushes with Grafting Density Gradients of Solid Substrates: 1. Experiment, *Macromolecules,* 40, **2007**, 8756-8764.
38. Liu, J, Dapeng, C, Liqun, Z, Molecular Dynamics Study on Nanoparticle Diffusion in Polymer Melts: A Test of the Stokes-Einstein Law, *J. Phys. Chem. C* **2008**, 112, 6653-6661.
39. Einstein, A, Uber die von der molekularkinetischen Theorie der Warme geforderte Bewegung von in ruhenden Flussigkeiten suspendierten Teilchen; von A. Einstein, *Annalen der Physik*, [4], 17, 549-560 (**1905**)
40. Stokes, G, Trans Cambridge Phil Soc., 9. 5 (**1856**)
41. Chen, HY, Stepanov, EV, Chum, SP, Hiltner, A, Baer, E, Linear Stress Relaxation Behavior of Amorphous Ethylene-Styrene Interpolymers, Macromolecules **2000**, 33, 8870-8877.
42. Zeinab H, Van de Ven TGM, Tufenkji N, Bacterial Capture Efficiency and Antimicrobial Activity of Phage-Functionalized Model Surfaces, *Langmuir*, **2011**, 27,5472-5480.

Chapter 4: Nanoscale Topography Mediates the Adhesion of F-Actin

Reprinted with permission from, Caporizzo MA, Sun Y, Goldman YE, Composto RJ, Nanoscale Topography Mediates the Adhesion of F-Actin, *Langmuir*, 2012, 28, 12216-12224.

4.0 Introduction

Controlling the attachment of biological molecules to surfaces is of widespread importance for applications ranging from DNA microarrays to nanodevices based on the nanometer-scale operation of biomolecular motors.[1] Directing the location and binding of filamentous cytoskeletal proteins, such as actin and microtubules, on nanoengineered surfaces is a necessary step in engineering functional nanomachines driven by molecular motors.[2] Actin contributes to both dynamic and structural functions inside cells including mechanical strength, communication between transmembrane and cytoplasmic proteins, as well as locomotion in cells.[3-5] Compared to the microtubule, actin is more flexible, with a persistence length of about 10 μm, and can therefore make tighter turns to accommodate smaller surface features without denaturing or rupturing,[6] making it a good candidate to investigate the interplay between nanoscale surface roughness and cytoskeletal protein adhesion. By investigating the behavior of actin on surfaces of varying roughness we aimed to test whether nanoscale roughness is capable of modulating f-actin adhesion independent of molecular properties of the surface, such as chemistry and charge. The effects of substrate roughness on actin adhesion may also indicate

the topological length scales which perturb actin filament structure impacting transport velocity and thus device efficiency.

Over the past decade, devices based on the ex-vivo function of nanomachines have been designed using expertise from the nanotechnology and biophysical communities.[7-10] A majority of this work is based on "top-down" lithography of micro-channels, which direct filamentous proteins during active gliding on surface-immobilized molecular motors powered by ATP.[1] Cargoes are selectively attached to biofilaments, guided by the surface microtopography or chemistry, and deposited in targeted areas.[8,9] Compared to myosin-actin, the kinesin-microtubule system has received more attention because it is more robust, and the stiffer microtubules can be directed by microscale channels which are relatively large and easy to fabricate.[11,12] Because of their relative flexibility, actin filaments should be able to make U-turns in channels an order of magnitude smaller than those used for microtubules; therefore, tracks for acto-mysoin based molecular shuttles must be narrower, allowing for patterning at higher density.[12] Guiding of actin filaments requires channels to be both chemically and topographically defined with widths not exceeding 200nm.[12] Thus, the interaction between nanoscale topography and f-actin is important for designing devices based on transport by myosin molecular motors.

The speed of a molecular motor based device is limited by the maximal velocity of translocation at saturating ATP concentration. Transport velocity can be reduced by the characteristics of the surface.[13-17] For example, thermoresponsive polymers can be used to control the binding and velocity of microtubules on kinesin coated surfaces suggesting that physical barriers, such as cargoes or surface features, have a significant effect on the speed of translocation.[13,14] When muscle heavy meromyosin was bound to glass or various polymer surfaces, filament gliding exhibited a wide range of velocities, and highly hydrophilic and highly

hydrophobic surfaces both suppressed motility.[15,16] Measurements of surface hydrophobicity depend on both the surface chemistry and underlying surface topography.[18] Thus a systematic study on the effect of surface roughness on biofilament-surface interactions should provide insight for understanding the substrate properties directly affecting transport velocity.

In this chapter textured surfaces with nanometer scale roughness are fabricated to examine the relevant length scale for controlling the attachment and dynamics of actin filaments. F-actin is attracted towards the nano-bio interface by the amine functionalized nanoparticles that partially embed into a random copolymer film attached to a mica substrate. By varying nanoparticle diameter and coverage, island, bilayer, and peak-and-valley morphologies are prepared with feature sizes, h_{avg}, ranging from ~10nm to ~350nm and spacing from several nm's to about a μm. Correspondingly, f-actin displays immobilized, side-on-wobbly, or end-on attachment. The attachment of f-actin on these surfaces is modeled by examining the f-actin bending energy as a function of feature size and spacing. Myosin-V processive motility assays are used to test whether the filaments attached to these nanoengineered surfaces retain their native support of active motility. Moreover, the tunabilty of filament attachment in conjunction with a predictive model suggests that NP decorated surfaces may have the potential to sort cytoskeletal filaments by persistence length.

4.1 Polymer nanocomposite surface

Nanoengineered surfaces are fabricated by grafting silica nanoparticles on smooth, optically transparent substrates. A thin sheet of mica, coupled via optical epoxy to a glass coverslip, is coated with a poly(styrene-random-acrylic acid), SAA, film . The dry SAA films are 39 ± 2 nm and 286 ± 8 nm thick as measured by ellipsometry, and have a RMS roughness of 0.27 ± 0.01 nm as determined by AFM. The surface of SAA provides the carboxylic acid groups for covalent attachment of amine functionalized silica NPs with diameters, d, of 12 nm, 20 nm, 45

nm, and 85 nm. Figure 4.1 shows a gallery of AFM images of the surface morphology as NP diameter (columns) and coverage (rows) increases. At fixed d and increasing coverage, the surface morphology evolves from islands of individual NPs (column 1) to a smooth bilayer (column 2) after the NPs saturate the SAA layer. As coverage increases, the NPs form aggregates that exhibit a peak and valley (PAV) morphology of intermediate (column 3) and high (column 4) roughness on the thicker SAA films. Correspondingly, at similar NP coverage, increasing d leads to self-similar morphologies (*i.e.*, the morphology is dependent only on NP coverage, not NP size) although the overall roughness of a particular morphology increases as NP diameter increases. These surfaces provide a unique platform with tunable features for investigating interactions between biopolymers and nanoengineered surfaces. First, for the island morphology, the spacing and height of monodisperse features can be independently varied. Such control was not possible in prior studies with PAA films cross-linked with amine terminated silanes.[19] Second, the bilayer morphology exhibits a smooth, uniform surface that should strongly attract f-actin. Third, the peak and valley morphology exhibits aggregates with a large variation in height that modulate the interaction with actin. Thus, by varying NP size and coverage, surfaces with island, bilayer, and peak and valley morphologies are prepared with controlled roughness ranging from 2 nm to 54 nm.

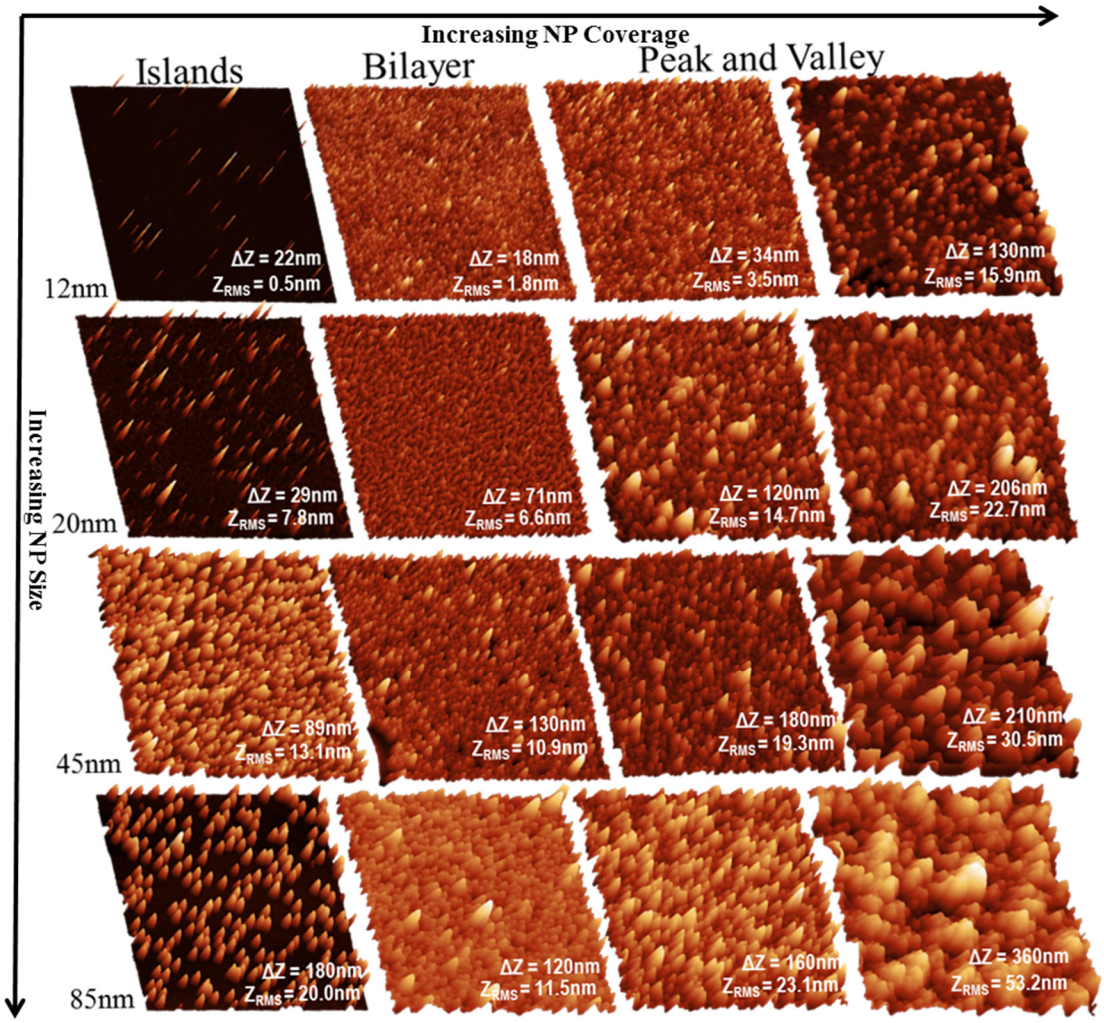

Figure 4.1: AFM topographic images show substrate morphology changes with nanoparticle size and coverage. The rows (top to bottom) correspond to NP diameters of 12 nm, 20 nm, 45 nm, and 85 nm, respectively. The RMS roughness, Z_{RMS}, represent the entire 5 x 5 μm^2 image area. The Z-scale, ΔZ, ranges from 18 nm to 360 nm and indicates the difference between the minimum and maximum height in each image. Column 1 shows representative surfaces of the island morphology at different NP coverages for each NP size. The coverage of islands can be controlled for all NP sizes. Column 2 shows the bilayer morphology which exhibits a minimum in RMS roughness for each morphology marking the transition from island to a peak and valley (PAV) morphology. Columns 3 and 4 show the PAV morphology as it evolves from low (column 3) to high (column 4) roughness.

The surface morphology (figure 4.1) depends on the diameter and coverage of NPs. Coverage is controlled by varying the incubation time of the SAA coated substrate in a solution containing amine terminated NPs (details in supplementary information). The mechanism of

attachment begins with the collision of NPs with the SAA film, followed by their penetration into swollen AA rich domains. As the SAA film becomes saturated with embedded NPs, additional NPs bind covalently to the outer surface resulting in topographic features having an average height, h_{avg}, corresponding to the NP diameter. This "island" morphology is characterized by NPs separated by an average spacing, S, ranging from about 100 nm to 1 µm. A smooth "bilayer" develops when a 2-D randomly packed over-layer coating the surface of the SAA film develops where the surface just below is saturated with imbedded NPs. This over-layer initially prevents the attachment of additional NPs, however, NP binding will continue if the film is thick enough (thickness greater than d) to enable the sinking of the over-layer and simultaneous swelling of the film. This leads to the exposure of new AA domains and aggregates evolve causing the height distribution to broaden with increasing h_{avg} (the peak and valley morphology), shown in Columns 3 and 4 of figure 4.1. As described later, this large variance in peak height is one mechanism by which f-actin is inhibited from attaching parallel to the substrate. Table 4.1 summarizes the substrate parameters for the island, bilayer, and peak and valley morphologies. Higher roughness values indicate larger features and/or smaller spacing.

	Observed RMS Roughness		
Diameter	**Island**	**Bilayer**	**Peak And valley**
12nm	0.5 - 7.6 nm	1.0 - 2.1 nm	3.2 - 20.1 nm
20nm	2.1 - 8.3 nm	7.3 - 8.5 nm	11.4 - 22.7 nm
45nm	8.0 - 13.1 nm	9.9 - 11.1 nm	14.2 - 30.5 nm
85nm	16.2 - 38.8 nm	11.5 - 12.1 nm	19.1 - 53.2 nm

Table 4.1: Summary of RMS roughness values for the nano-engineered surfaces. The range of roughness values corresponding to the island, bilayer, and peak and valley morphologies is given for each NP diameter. Values are determined from AFM images of individual surfaces over a 5 x 5 μm^2 area. The number of surfaces used in the study was ~200 corresponding to ~ 15 samples per entry.

4.2 Controlling f-actin adhesion

F-actin adsorption on nanoengineered substrates depends on an interplay between electrostatic attraction and surface topography, characterized by feature spacing and height of the NPs (NP aggregates) grafted to the substrate. Figure 4.2 shows TIRF images of f-actin after 1 minute incubation in M5 buffer. The electrostatic attraction decays over ~1.7 nm, the Debye length. Depending on surface topography, the f-actin behavior in Figure 4.2 can be characterized as immobilized (2a, 2c), side-on wobbly (2b) or end-on (2d). If NPs are isolated, f-actin absorbs at low coverage and forms immobilized rings around the islands of small NPs (d = 20 nm, 2a). However, on islands of larger NPs (d = 85 nm) f-actin absorbs at a higher coverage and remains relatively straight, but wobbles (weakly attached, Fig. 2b). The NP to NP lateral separations are similar in 2a and 2b, 350 nm and 365 nm, while the difference in h_{avg} of the NPs, 13 nm and 89 nm respectively, distinguishes these surfaces. Thus, in 2b f-actin is elevated atop the NPs resulting in a low interfacial area between NPs and filaments. As a result, f-actin is weakly bound and undergoes lateral fluctuations (i.e., “side-on wobbly”). When the spacing between NPs is reduced from 350 nm to 209 nm at fixed NP diameter (d = 20 nm), f-actin absorption changes from immobilized rings (2a) to a side-on wobbly conformation (not shown but similar to 2b).

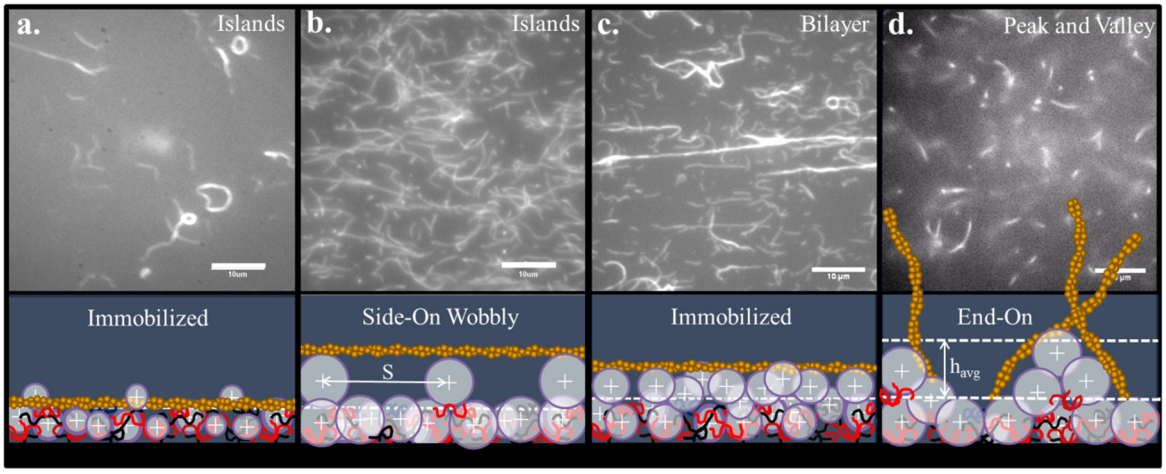

Figure 4.2: TIRFM images of rhodamine-phalloidin stabilized f-actin. Adsorption on selected surfaces is shown after 1 minute of incubation of 50 nM actin. Below each image is a representative cross-sectional schematic of actin binding. **a.** Island morphology (d = 20 nm), f-actin is immobilized forming rings with radii roughly 5 µm. Feature spacing, S = 350 nm; h_{avg} = 12.85 nm **b.** Island morphology (d = 85 nm) with a similar interparticle spacing as 2a exhibits high actin coverage and straight filaments which are not immobilized on the basal plane but are bound parallel to the substrate plane and wobble. S = 365 nm; h_{avg} = 89 nm **c.** Bilayer morphology (d = 45 nm) on which filaments immobilize; S = 213 nm; h_{avg} = 6.7 nm. **d.** Peak and valley morphology (d = 85 nm) where filaments end-on attach and wobble. S = 488 nm; h_{avg} = 171.1 nm Scale bars are 10 µm.

For the bilayer, f-actin is immobilized for all NP diameters. Figure 4.2c shows f-actin on a bilayer of 45 nm NPs with an RMS roughness is 11 nm. Both straight and ring-like filaments are observed. For the bilayer, the adhesion of f-actin is strong because the smooth surface allows actin to make a large number of attachment points near the apex of the NPs. f-actin is elevated in the same manner as in the island morphology (4.2b) but due to the larger number of attachment points (high interfacial area) the filaments are immobile.

The peak and valley morphology is dominated by large (tall) aggregates of NPs that limit how closely f-actin can approach the substrate. This behavior is analogous to the interaction between f-actin on the island morphologies consisting of large, individual NPs (4.2b). Figure 4.2d shows f-actin attaching at one point to the aggregates that make up the peak and valley morphology. Although both of these morphologies are prepared with the same NP size (d = 85

nm) and are relatively rough, f-actin attachment is different, side-on wobbly versus end-on respectively, indicating that RMS roughness is not the only determinant of the nature of filament attachment to the surface.

To determine whether filaments immobilized on the NP surfaces could support myosin-based motility, translocation of quantum dot labeled myosin V was tested. Motility was observed on all of the surfaces. At 10 μM ATP, filaments immobilized on a bilayer (d = 85 nm, S = 195 nm), exhibited a mean velocity of 154 ± 35 nm/s. This value is slightly lower than earlier measurements using rhodamine-or YFP-labeled myosin V translocating on actin filaments attached via biotin-streptavidin[20,21] presumably due to an effect of the NP surface on either the myosin or the actin.

4.3 Modeling actin assembly

F-actin attachment to nanoengineered surfaces exhibits two main trends. First, as NP (or aggregate) spacing, S, decreases, f-actin is observed to fluctuate as side-on or end-on (4.2b and 4.2d). Namely, substrates with large, closely spaced features frustrate f-actin from strongly adhering to the surface. Second, surfaces that display a large polydispersity in the feature size attract f-actin end-on, whereas those with monodisperse features allow for side-on attachment. This behavior suggests that the filament interaction at the interface is modulated by the ability of actin to bend and conform to topographic features presented by the substrate. A model which relates these surface parameters directly to the bending energy of f-actin incorporates the energetic penalty for actin to conform to the topographic features described above. The actin attachment behavior shown in figure 4.2 is attributed to the relative strengths of the energetic gain due to electrostatic attraction and the energetic cost of actin binding on the nanoengineered surface.

To interpret experimental results, f-actin is modeled as a semi-rigid biofilament brought into contact with a NP decorated surface shown in the first column of figure 4.1. For simplicity, we assume that f-actin immobilizes by attachment near the top of the NPs bending normal to the sample plane to reach the basal plane or binds directly to the surface by weaving in-plane around NPs as depicted in Figures 3a and 3b, respectively. In this study, the filaments are relatively stiff and straight for microns (persistence length of f-actin, P ~ 17 μm)[22], whereas the NP spacing, S, and height, h_{avg}, are less than 1 μm.

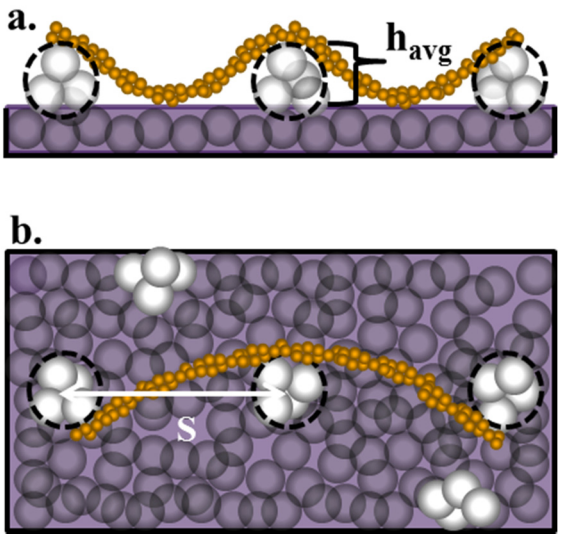

Figure 4.3: Possible binding geometries for actin immobilization. a. (Side-view) Out-of-plane bending (i.e. perpendicular to the surface) where actin bending over the top of features is required for immobilization on the substrate. The height of the features, h_{avg}, and their spacing, S, define a bending radius for the actin filament, R. **b.** (Top view) In-plane bending (i.e. parallel to the surface). F-actin is constrained to lie in the substrate plane and curve around features. Whereas h_{avg} and S are the same in both 3a and 3b, 3b gives rise to a larger bending radius and thus the conformation in 3b is more energetically favorable.

TIRF images of f-actin on the island morphology (figure 4.2) indicate that filaments do not kink or break upon attaching to the NPs. Therefore a worm-like chain model is used to express the bending energy in terms of filament length, L_o, and persistence length, P = 17 μm:

$$E_b(h) = k_B T \frac{PL_o}{2\left[\frac{{h_{avg}}^2 + S(h)^2}{2h_{avg}}\right]^2} \qquad (4.1)$$

In equation 4.1, the bending radius, is represented by the expression in brackets, and S(h) is the average feature spacing measured at a height, h, from the basal plane by thresholding topographic images; h_{avg} is the average feature size measured for each surface.[23] Normalizing E_b by L_o = 1 µm, equation 4.1 yields an expression for the bending energy of f-actin as a function of surface topography, S(h) and h_{avg}. By comparing the values of the bending energies for S >> h_{avg}, f-actin is predicted to immobilize via in-plane bending (figure 4.3b) because E_b in-plane is 16 fold less than the out-of-plane bending energy (figure 4.3a). This prediction is consistent with our experimental results (figure 4.2a) as well as others,[19] where f-actin is found to form rings and bends not predicted by the worm-like chain model. For actin, bends of radii smaller than 10 µm are rarely observed for unattached actin filaments. Their frequent appearance in filaments immobilized on substrates indicates that another factor such as conformation to topography plays an important role in filament attachment. Using feature height and spacing as variables, the bending energy model agrees with experimentally observed bending of f-actin.

Figure 4.4a shows how the bending energy of f-actin increases as feature spacing decreases and height increases according to equation 4.1 for the experimental range of parameters. For the island morphology, the values of S and h_{avg} that produce immobilized filaments correspond to the dark blue region in 4.4a indicating that a bending energy penalty below ~2 k_BT per µm (dotted line) allows f-actin to bend around the individual, randomly distributed NPs as shown in figure 4.3a . At low S, the bending energy strongly increases as h_{avg} increases, while at large h_{avg},the bending energy is most sensitive to changes in spacing. The range of feature height and spacing that lead to the countour plot of E_b shown in figure 4.4a

correlates to the experimentally obtained range of these parameters. The model is applicable for $h_{avg} < S$, since at $h_{avg} = S$ clusters contact each other.

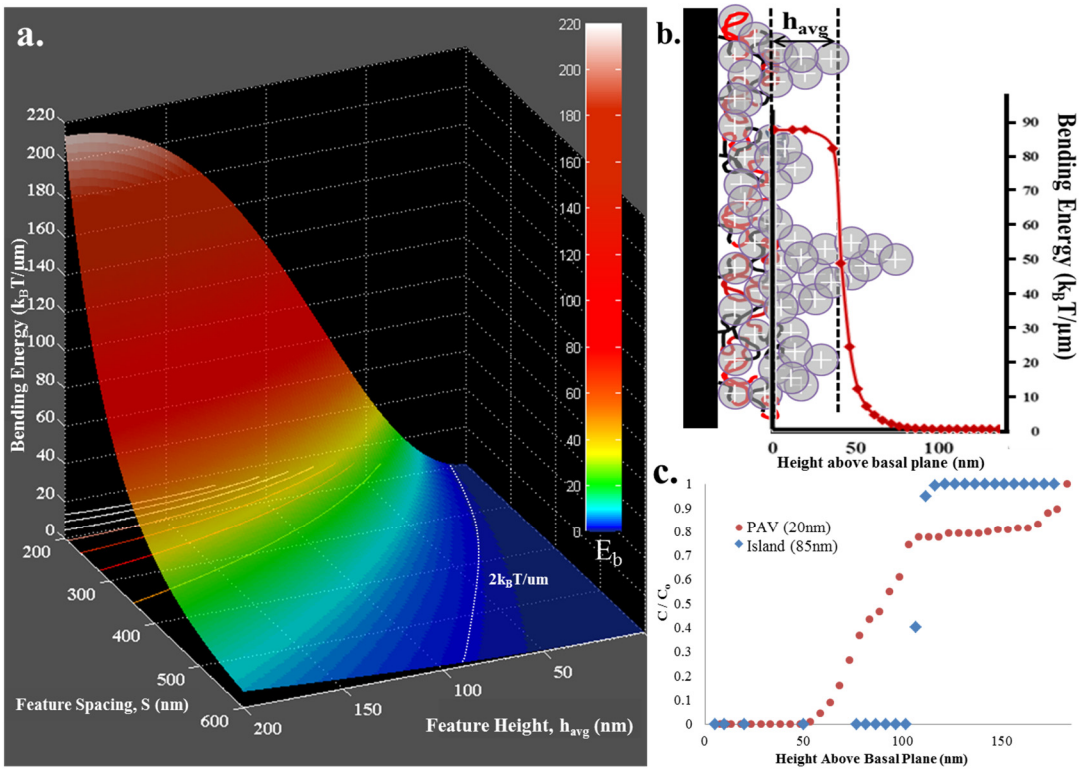

Figure 4.4: Bending energy penalty for actin filaments as a function of topography a. Surface map of bending energy in units of k_BT per µm as a function of feature height (h_{avg}) and spacing (S). The dotted line indicates the experimentally observed threshold for actin immobilization, 2 k_BT per µm. Regions of higher energy (Cyan through White) indicate S and h_{avg} combinations which frustrate actin immobilization, while the area below the threshold (Dark Blue) indicates height a spacing combinations leading to immobilized filaments. **b.** shows how the bending energy evolves with height above the basal plane, h, on the X-axis. $E_b(h)$ is overlaid on a schematic of the peak and valley morphology to illustrate how it is determined, h_{avg}=44 nm. **c.** The normalized probability of a filament to overcome the energetic barrier associated with the NPs and reach a height, h, from the basal plane is calculated using the Arrhenius equation and represented by relative concentration (Y-Axis). Blue data points are taken from an island morphology with d = 85 nm and h_{avg} = 102 nm, The red data represents a peak and valley morphology with d = 20 nm and h_{avg} = 53 nm. $E_b(h)$ is the only energetic contribution considered in this plot, and therefore the plot represents the effect of the topography alone on the likelihood of finding actin at a distance, h, from the surface

The bending energy penalty (figure 4.4a) is determined by the interplay between the height and spacing of features. Figure 4.4b shows how E_b varies as a function of height from the

basal plane for the PAV morphology fabricated from 45 nm NPs. Near the surface, E_b is ~85 $k_BT/\mu m$ and then decreases to 0 near the apex of the features. The polydispersity of surface features defines the slope of the decay of $E_b(h)$. For example, for the PAV morphology with 20 nm NPs, E_b decays slover over a distance of 60 nm, whereas for the island morphology with 85 nm NPs, E_b decays more rapidly over 25 nm (Figures 4.4c and S5). The sharpness of this decay determines whether the adhesion of f-actin will be side-on or end-on (cf. 4.2b and 4.2d). E_b is large (~70 $k_BT/\mu m$) for both morphologies, and surface immobilization is inhibited; however only the PAV morphology (large height dispersity) inhibits f-actin from attaching to the surface in a side-on conformation.

The effect of topography alone on the density of actin filaments adopting a side-on conformation at a height, h, from the basal plane can be determine from the Arrhenius equation, $C/C_o = e^{-E_b(h)}$, figure 4.4c. The normalized concentration, C/C_o, reflects the probability of a 1µm filament contour fitting between the surface features due to thermal motions allowing for side-on attachment to the nanocomposite at a given height. The 85 nm island morphology (Blue) and the 20 nm PAV morphology (Red) both inhibit actin from reaching the basal plane (C/C_o ~0 at h = 0). The likelihood that actin will approach a distance of h_{avg} from the surface where it can electrostatically attach to the particles is high for the island morphology, C/C_o ~1 at h_{avg}= 102 nm, and low for the PAV morphology, C/C_o <0.01 at h_{avg} = 52 nm. Subsequently, actin binding to the monodisperse islands is dominated by side-on attachment while the inability for filaments to adopt a side-on conformation near the surface of the PAV morphology leads to a majority of end-on attachments.

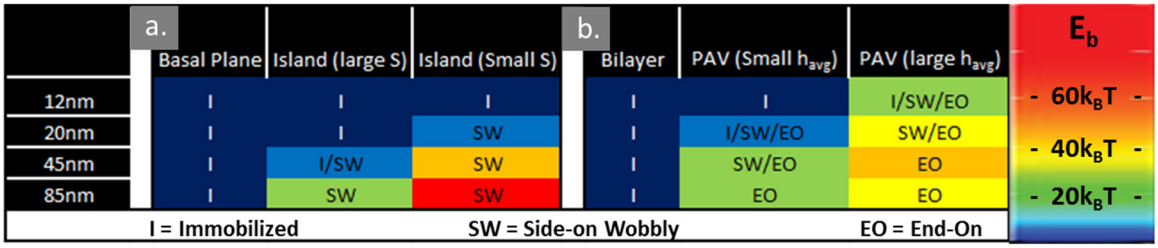

Figure 4.5: Binding state diagram for f-actin. At each nanoparticle diameter the mode of f-actin binding is shown on the various types of surfaces. **a.** F-actin binding is indicated for the low coverage regime where NP coverage adopts an island morphology. **b.** F-actin binding is characterized in the high NP coverage regime where actin adopts the peak and valley morphology. Colors correspond to an average value of E_b experimentally determined in each region. The scale of E_b seen on the right is the same scale as figure 4.4a.

In order to compare experimental results with the model, a binding state diagram can be seen in figure 4.5. This diagram shows the correlation between actin attachment modes (e.g. immobilized, side-on wobbly, end-on) for the various surface morphologies and E_b calculated for those surfaces. The color of each box corresponds to the average value of E_b using the same scale as in figure 4.4a. Near the transition value of $2k_BT$ per µm, morphologies can support a mixture of different filament attachment modes. However, in most cases, filament binding on a single surface is characterized by one attachment mode. When the gradient of E_b along a given contour is small, the transition between attachment modes is more gradual. Figure 2.4 provides more information about how the bending energy varies as the feature height and spacing evolve for the island and PAV morphologies.

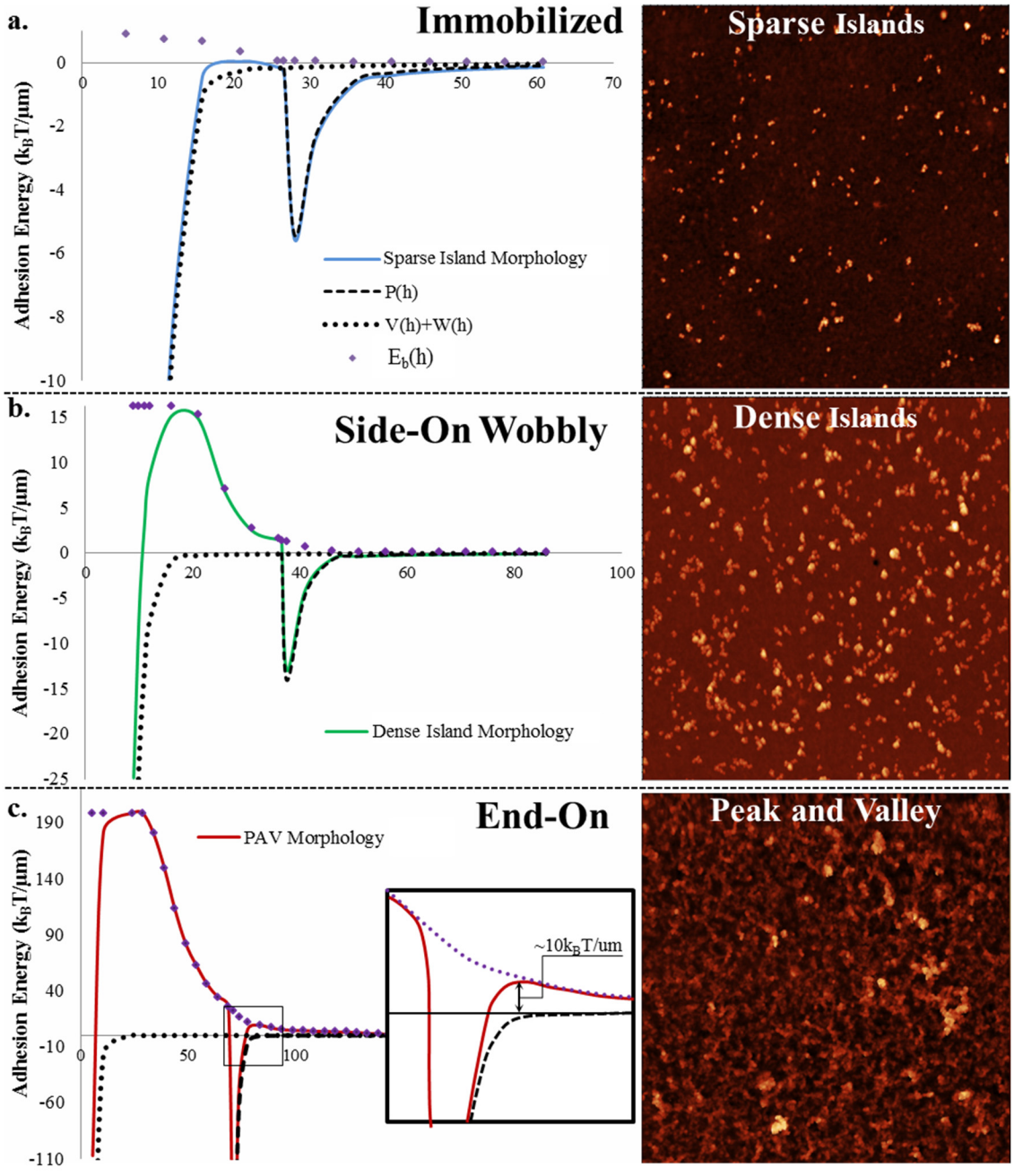

Figure 4.6: F-actin interaction energy for side-on attachment as a function of height above the basal plane (nm). These individual traces; Van der Waals potential, W(h), surface electrostatic potential, V(h), the NP feature electrostatic potential, P(h), and the bending energy term, $E_B(h)$, are plotted in 4.5a through 4.5c. The sum of the interactions is shown by the solid colored lines. AFM topographic images (5 x 5 μm^2) are shown to the right of their corresponding interaction energies. **a.** Potentials plotted for the sparse island morphology (d = 20 nm) is shown in which the average spacing at the surface, S = 388 nm and h_{avg} = 24 nm. AFM topography exhibits Z_{RMS}=

2.8 nm and ΔZ = 47 nm. **b**. Potentials plotted for the dense island morphology (d = 20 nm) in which S = 222 nm and h_{avg} = 35 nm. AFM topography exhibits Z_{RMS} = 7.8 nm and ΔZ = 100 nm. **c.** Potentials plotted for the peak and valley morphology (d = 12 nm) where S = 154 nm and h_{avg} = 69 nm. AFM topography exhibits Z_{RMS} = 20.1 nm and ΔZ = 220 nm. The inset shows a barrier of ~10 $k_BT/\mu m$ that inhibits the side-on attachment of actin.

To understand the energetic contributions associated with f-actin binding to the surface, the surface electrostatic potential, V(h), the electrostatic potential generated by the NP features, P(h), the Van der Waals potential, W(h), and the bending energy, $E_b(h)$, are plotted for morphologies that lead to immobilized, side-on wobbly, and end-on attached f-actin filaments. Figure 4.6 shows the individual and total interaction energies as a function of distance from the basal plane for island (4.6a and 4.6b) and PAV morphologies (4.6c) for a filament to attach parallel to the substrate. For the island morphology, f-actin is either immobilized directly onto the basal plane (4.6a) or suspended atop the NPs (4.6b), whereas for the PAV, F-actin is end-on attached (4.6c). The surface and NP electrostatic potentials are calculated using surface charge and Debye length described in the supplement. The bending energy for actin attachment $E_b(h)$ is calculated from equation 1 and represents a repulsive interaction, while the electrostatic interaction between the f-actin and the nanoparticles, P(h), leads to a secondary minimum near the average feature height.

The interaction energy for the island morphology (e.g. 4.6a) displays a secondary minimum of roughly -5 k_BT per μm near 30 nm. Because few small particles protrude from the surface (e.g. small h_{avg} and large S), the bending energy penalty is small and f-actin can bind parallel to the surface and immobilize. However at higher coverage (figure 4.6b), the potential barrier is larger, ~15 $k_BT/\mu m$, inhibiting F-actin attachment at the basal plane. As a result, f-actin is trapped in the secondary minimum elevated above the surface and binding is characterized as side-on wobbly. For the PAV morphology, the bending penalty is large, ~190 $k_BT/\mu m$, and a strong secondary minimum is observed because of the high density of NP aggregates. The

polydispersity of features extends the bending energy penalty further from the surface than in 4.6a and 4.6b which results in an activation energy of ~10 $k_BT/\mu m$ near h = 75 nm. Thus the rate of side-on attachment is extremely low and the majority of filaments attach end-on. These calculations of the interaction energy between f-actin and nano-engineered surfaces demonstrate that feature height, spacing, and height distribution can dictate the assembly of f-actin at the interface.

4.4 Conclusions

In this study, the electrostatic binding of actin to surfaces was found to be modulated by the presence of nano-scale topographic features. By controlling the size, areal density, and polydispersity of features, actin attachment could be either immobilized, side-on wobbly, or end-on. Modeling filaments as worm-like chains, actin is expected to preferentially bend in-plane (cf. figure 4.3) leading to an expression for the energetic penalty of actin binding side-on to topographically diverse surfaces. This energetic penalty was directly compared with the electrostatic potential for actin to bind to the surface in buffer to analyze observed filament behavior. Plotting the sum of the potentials (cf. gigure 4.6) demonstrates how actin binding can be controlled by topographic features to yield elevated and end-on attached filaments on roughened surfaces despite an electrostatic affinity favoring filament immobilization. Our results support the idea that filamentous proteins respond to topography and provides a scale over which actin filaments in particular are sensitive to topographic features. Electrostatically immobilized actin filaments support myosin V translocation, which is significant because it will allow these surfaces to be used in future studies where the height or degree of actin binding is important. For example engineering the intersection between cytoskeletal filaments by controlling the distance between filaments will allow for a precise investigation of switching of multiple motor labeled cargos between microtubules and actin filaments.

4.5 References

1. Hess, H. Engineering Applications of Biomolecular Motors, *Annu Rev Biomed Eng.* **2011,** 13, 429-450.
2. Mansson, A.; Balaz, M.; Albet-Torres, N.; Rosengren, K. J. In vitro assays of molecular motors – impact of motor-surface interactions, *Frontiers in Bioscience*, **2008** 13, 5732-5754.
3. *Actin-based Motility : cellular, molecular and physical aspects* ; Marie-France Carlier, editor. Springer: New York, 2010.
4. Mitchinson, T.J.; Cramer, L.P. Actin-Based Cell Motility and Cell Locomotion, *Cell* **1996**, 84, 371-379.
5. Hirokawa, N. Kinesin and dynein superfamily proteins and the mechanism of organelle transport, *Science* **1998**, 279, 519-526.
6. Agarwal, A.; Hess, H. Biomolecular motors at the intersection of nanotechnology and polymer science, *Prog. Polym. Sci.,* **2010,** 23, 252-277.
7. Vikhorev, P. G.; Vikhoreva, N. N. Månsson, A., Bending Flexibility of Actin Filaments during Motor-induced Sliding, *Biophysical Journal* **2008**, 95, 5809-581
8. Kim, T.; Meyhofer, E. Nanofluidic concentration of selectively extracted biomolecule analytes by microtubules, *Anal Chem.* **2008**, 80(14), 5383-5390.
9. Kim, T.; Cheng, L.-J.; Kao, T.-M.; Hasselbrink, E.F.; Guo, L.J.; Meyhofer, E. Biomolecular motor-driven molecular sorter, *Lab Chip* **2009**, 9, 1282-1285.
10. Byun, K-E.; Choi D.S.; Kim, E.; Seo, D.H.; Yang, H.; Hong, S. Graphene-Polymer Hybrid Nanostructure-Based Bioenergy Storage Device for Real-Time Control of Biological Motor Activity, *ACS Nano* **2011**, 5(11) 8656-8664.
11. Lin T.-C.; Meyhofer, E.; Kurabayashi, K. Predicting the stochastic guiding of kinesin-driven microtubules in microfabricated tracks: A statistical-mechanics-based modeling approach, *Phys. Rev. E* **2010**, 81, 011919.
12. Sundberg, M.; Bunk, R.; Albet-Torres, N.; Kvennefores, A.; Persson, F.; Montelius, L.; Nicholls, I.A.; Ghatnekar-Nilsson, S.; Omling, P.; Tagerud, S.; Mansson, A. Actin Filament Guidance on a Chip: Toward High-Throughput Assays and Lab-on-a-Chip Applications, *Langmuir*, **2006**, 22, 7286-7295.
13. Korten, T.; Birnbaum, W.; Kuckling, D.; Diez, S. Selective Control of Gliding Microtubule Populations, *Nano Lett.* **2012**, 12, 348-353.
14. Ionov, L.; Stamm, M.; Diez, S. Reversible switching of microtubule motility using thermoresponsive polymer surfaces, *Nano Lett.* **2006**, 6, 1982-1987.
15. Nicolau, D.V.; Solana, G.; Kekic, M.; Fulga, F.; Mahanivong, C.; Wright, J.; dos Remedios, C.G. Surface Hydrophobicity Modulates the Operation of Actomyosin-Based Dynamic Nanodevices, *Langmuir*, 2007, 23, 10846-10854.
16. Albet-Torres, N.; O'Mahony, J.; Charlton, C.; Balaz, M.; Lisboa, P.; Aastrup, T.; Mansson, A.; Nicholls, I.A. Mode of Heavy Meromyosin Adsorption and Motor Function Correlated with Surface Hydrophobicity and Charge, *Langmuir*, **2007**, 23, 11147-11156.
17. Kumar, N.; Parajuli, O.; Dorfman, A.; Kipp, D.; Hahm, J.I. Activity study of self-assembled proteins on nanoscale diblock copolymer templates, *Langmuir* **2007,** 23(14) 7416-7422.

18. Marmur. A. Wetting of Hydrophobic Rough Surfaces: To be heterogeneous or not to be, *Langmuir* **2003** 19 (20): 8343–8348.
19. Park, J. H.; Sun, Y.; Goldman, Y. E.; Composto, R. J. Self-assembled charged hydrogels control the alignment of filamentous actin, *Soft Matter* **2010**, 6, 915-921.
20. Forkey, J. N.; Quinlan, M. E.; Shaw, M. A.; Corrie, J. E. T.; Goldman, Y. E. Three Dimensional structural dynamics of myosin V by single molecule fluorescence polarization, *Nature* **2003**, 422: 399–404.
21. Baker, J. E.; Krementsova, E. B.; Kennedy, G. G.; Armstrong, A.; Trybus, K. M.; Warshaw, D. M. Myosin V processivity: Multiple kinetic pathways for head-to-head coordination, *PNAS* **2004**, 101: 5542-5546.
22. Vikhorev, P. G.; Vikhoreva, N. N. Månsson, A., Bending Flexibility of Actin Filaments during Motor-induced Sliding, *Biophysical Journal* **2008**, 95, 5809-5819.
23. Nelson, P. *Biological Physics: Energy, Information, Life,* W.H. Freeman and Co., New York, **2008,** 341-385.
24. Israelachvili, J. N. *Intermolecular & Surface Forces,* Academic Press, London, Second Edition, **1992**.
25. McConnell, M. D.; Yang, S.; Composto, R. J. Covalent Nanoparticle Assembly onto Random Copolymer Films, *Macromolecules* **2009**, 42, 517-523.
26. Pardee, J.D.; Spudich, J.A. Purification of muscle actin. *Methods Cell Biol*. **1982,** 24, 271–289.
27. Beausang, J.F.; Sun, Y.; Quinlan, M.E.; Forkey, J.N.; Goldman, Y.E. *Single Molecule Fluorescence Polarization via Polarized Total Internal Reflection Fluorescent Microscopy*. In: Sialiano, I., *Laboratory Manual for Single Molecule Studies*, Cold Spring Harbor Laboratory, Cold Spring Harbor, NY. **2007.**
28. De La Cruz, E.M.; Wells, A. L.; Rosenfeld, S. S.; Ostap, E. M.; Sweeney, H. L. The kinetic mechanism of myosin V. *Proc. Natl Acad. Sci. USA* **1999,** 96, 13726–13731.
29. Harada, Y.; Sakurada, K.; Aoki, T.; Thomas, D.D.; Yanagida, T. Mechanochemical coupling in actomyosin energy transduction studied by in vitro movement assay. *J. Mol. Biol.* **1990,** 216, 49-68.

Chapter 5: Enhanced Backward Stepping of Myosin V on Electrostatically Immobilized Actin Filaments

5.0 Introduction

Class-V myosins are dimeric actin-associated molecular motors necessary for cytoplasmic organelle transport.[1] The catalytic heads of the myosin V dimer process along actin in an alternating hand-over-hand fashion leading to consecutive 36 nm center of mass translocation events in the direction of the barbed end of the actin filament.[2-4] The rarity with which myosin V missteps or takes backwards steps (translocation event towards the pointed end of the actin filament) optimizes its utility as a transporter and distinguishes class V myosins from other members of the myosin superfamily.[5] Strain-dependent control of nucleotide byproduct release, strain-gating, is the mechanism for inter-head coordination and high processivity in myosin.[6] In strain-gating, the development of tension between the leading and trailing heads causes asymmetry in head biochemical rate constants, leading to consistent detachment of the trailing head and forward procession of the molecular motor. The rigidity of the lever-arm domain likely regulates inter-head strain through the presence of 6 calmodulin binding, IQ, motifs which mediate lever-arm stiffness through their interaction with Ca^{2+}.[7] Herein it is demonstrated that tunable nanoscale roughness, which has been previously shown to immobilize actin filaments in a fashion which reduces filament persistence length[8,9], can disrupt coordination between the leading and trailing heads of myosin V leading to an enhancement of backwards steps.

Indirect evidence for the biochemical regulation of ATP hydrolysis rate, K_{ATPase}, by strain on myosin V occurs by applying assisting and opposing force to single and double headed

constructs to produce a strong strain magnitude and direction dependence of K_{ATPase}.[10] In particular, a few pN of opposing force significantly reduces the ADP release rate of a single headed construct leading to shower dissociation of the head from actin.[11] Similar optical trapping data shows that the rigid 6 IQ-motif lever arm is necessary for strain dependent ATPase biochemistry because single headed constructs lacking the native myosin V lever arm domain do not exhibit as great of a strain dependence on K_{ATPase}.[12] Opposing forces exceeding the stall force of myosin V (> 5 pN) leads to backwards stepping and spontaneous dissociation from acitn.[13,14] These elegant biochemical assays indirectly support the theory of strain-gating by providing evidence that biochemical rate control can occur by application of load to the myosin V monomer, and that existing strain in the dimer leads to less regulation by external load. Herein, the ability for a native myosin V dimer to generate internal strain between heads is disrupted by compromising the strong binding state of actomyosin. Strong binding between actin and myosin is crucial for biochemical rate regulation and inter-head strain generation through the conformation changes of the power stroke. The loss of inter-head coordination of myosin V on f-actin electrostatically immobilized to NPs suggests disruption of the strong binding complex of actomyosin due to NP-induced changes in f-actin structure.

F-actin persistence length reduction has been reported on surfaces upon which filaments are non-specifically, electrostatically bound. In particular f-actin binding to surfaces dramatically increases as the surface electrostatic potential becomes positive (attractive to actin) and tight rings and bends are observed on surfaces as electrostatic potential increases even under high ionic strength (25 mM KCl). [8] Absorption of enzymes to nanoparticles (NPs) of size ranging from 10nm to 100nm has been shown to cause destabilization of secondary structures in protein which scales with electrostatic surface potential.[15] Structural changes reduce the activity of lysozyme non-specifically absorbed to the surface of oppositely charged

nanoparticles.[15] Similarly, an interplay between filament persistence and electrostatic binding potential on topographically enhanced surfaces, leads to controllable actin binding, and surface bound filaments exhibit regular bends much tighter than the persistence length of f-actin.[8,9] Perturbations to f-actin persistence imply that the filament structure is altered by non-specific absorption to NP decorated surfaces consistent with the established denaturing of small proteins bound to particles.[15-17] Unlike the observed decrease in lysozyme activity, where the degradation of the enzyme directly correlates to a decrease in activity, actin filaments serve as biochemical tracks which catalyze the ATP hydrolysis of myosin mechano-enzymes.[18] Thus, partial degradation of actin may not affect myosin V motility or the binding of other proteins to actin depending on the domains compromised (i.e. if they are at the active site) by electrostatic absorption. Because of its highly regular processivity, myosin V is an ideal candidate for testing perturbations in f-actin associated with NP-induced structural changes as changes in myosin V kinetics can be correlated to changes induced by NPs on the underlying actin filaments.

Competition between actin rigidity and the electrostatic attraction can be modulated by nanoscale roughness.[9] In particular, a highly-roughened hierarchical surface topography requires f-actin to bend tightly, less than 1 μm in radius, to bind strongly on the surface (c.f. figure 4.2). Tight bending of actin is energetically unfavorable and actin filaments will bind weakly to highly roughened surfaces to retain its native persistence of 17 μm.[19] On surfaces with intermediate roughness, actin binds strongly by making regular sub-persistence length bends (persistence-length is compromised) of 1-5 μm, indicating a compromise in filament structure through decreased flexural rigidity.[9] The lack of identifiable breaks in surface immobilized filaments suggests a competition between filament rigidity and electrostatic binding to the surface. Myosin V to binds to bent actin filaments indicating that the f-actin structure remains at least partially intact. In this chapter, myosin kinetics are investigated on

actin filaments non-specifically adsorbed to positively charged NP-decorated surfaces. Electrostatic binding of f-actin to these surfaces disrupts actin structure and reduces myosin V velocity. The effect of NPs on molecular motor activity may disrupt intra-cellular transport when cationic NPs are absorbed into the cytoplasm of cells.

Herein, myosin V motility assays are conducted on persistence-length compromised f-actin strongly immobilized on amine-functionalized nanoparticle – polymer composite surfaces. The ability to change NP size and RMS roughness permits independent tuning of the local (NP-actin interaction strength) and global (f-actin surface proximity) force exerted on the actin filament by NP size and RMS roughness, respectively. Myosin V velocity and run length are found to be reduced on NP functionalized surfaces. This reduction in velocity scales with the NP-surface interaction strength. NP surfaces do not increase the number of stops or stalls in processive runs, indicating myosin velocity is reduced homogeneously along the length of the actin filament. By direct characterization of myosin V step-size, single isolated backwards steps are observed which increase in frequency as nanoparticle diameter (D_{NP}) increases from 12nm – 85nm. The average dwell time at 500 nM ATP is independent of D_{NP} indicating that the ATP binding rate is not altered in myosin V. Modelling shows that backward steps accounts for the reduction in velocity at low [ATP]; however at saturating [ATP] the maximal velocity is reduced by a reduction of K_{ATPase} on NP decorated surfaces. A modified Michaelis-Menten equation shows that velocity vs [ATP] is well captured by a reduction in the ADP released rate, k_{ADP-}. Thus, the appearance of backwards steps (loss of strain-gating) couples with a decrease in k_{ADP-}. The coupling between a reduced k_{ADP-} and inter-head strain supports previous hypotheses that motions in the lever-arm are strongly coupled to motions in the nucleotide binding pocket. More specifically precise coordination of actin with myosin in the strong binding state of actomyosin accelerates ADP release and induces the pre-power-stroke strained conformation.

The inter-head strain is necessary for myosin V to be highly processive, and therefore myosin rarely takes a backward step.[20]

5.1 Diverse nanoparticle decorated surfaces for f-actin immobilization

The surface roughness of NP-decorated surfaces is varied by changing NP size and/or the grafting time of NPs to the surface. Using poly(styrene-random acrylic acid), SAA, films on glass coverslips, NH_2-functionalized nanoparticles of varying diameter are covalently grafted at high densities to the polymer yielding surfaces with homogeneous topographic features and amine functionality. Figure 5.1 shows atomic force micrographs of NP-decorated surfaces capable of immobilizing f-actin. The nano-composites are designed to be transparent to enable the fluorescent imaging of myosin V. Figure 5.1a demonstrates that similar surface morphologies of NPs can be generated with D_{NP} = 20 nm, 45 nm, and 85 nm (left to right) so that the root-mean-squared surface roughness (Z_{RMS}) is approximately the diameter of the NP. F-actin can create attachment points with these surfaces at a periodicity of about $2D_{NP}$ without bending tighter than its persistence-length. Figure 5.1b shows that the surface roughness increases with increasing NP attachment at a fixed D_{NP} = 20 nm. When $Z_{RMS} < D_{NP}$ (figure 5.1b, left), the density of surface features increases as Z_{RMS} increases resulting in an increase of contact between NPs and actin. When $Z_{RMS} > D_{NP}$ (figure 5.1b, middle), Z_{RMS} increases by the growth of hierarchical features, which leads to fewer contacts between f-actin and the surface. For $Z_{RMS} >> D_{NP}$ (figure 5.1b, right) peak-like aggregates appear in the surface morphology and actin filaments must bend tightly ($R_{Bend} < 10\ \mu m$) to bind strongly to the surface. The highly roughened morphologies have shown a weaker association with actin. In particular, for $Z_{RMS} >> D_{NP}$, actin only attaches by one end to the surface despite the strong electrostatic affinity.[9]

To accurately measure biochemical rate changes in myosin and correlate them with structural changes in f-actin induced by NP-decorated surfaces, surfaces must be heterogeneous such that all actin filaments experience similar electrostatic binding potential. Figure 5.2 shows fluorescent images of f-actin bound to surfaces of different D_{NP} and Z_{RMS}, where the bright white dots are quantum dots (QDs) attached to myosin V. Figure 5.2 a-c represents D_{NP} = 20 nm, 45 nm, and 85 nm, respectively, and the Z_{RMS} of each surface is shown in the inset. For comparison, figure 5.2d shows f-actin immobilized on control surfaces where tail-grafted N-ethyl maleimide treated myosin II was used to graft f-actin to the surface. Generally, for $Z_{RMS} < 3D_{NP}$, surfaces well coated with NPs bind strongly to f-actin. Qualitatively, actin binding appears similar on surfaces of varying D_{NP}, as is illustrated by the top row of fluorescent images (figure 5.2a-c). On surfaces where Z_{RMS} was modulated at constant D_{NP}, slight differences in actin coverage are observed. For example, in figure 5.2a actin coverage is greater on the top image where the surface is smoother. Actin coverage being inversely proportion to roughness is consistent with actin affinity being lower on more roughened surfaces.

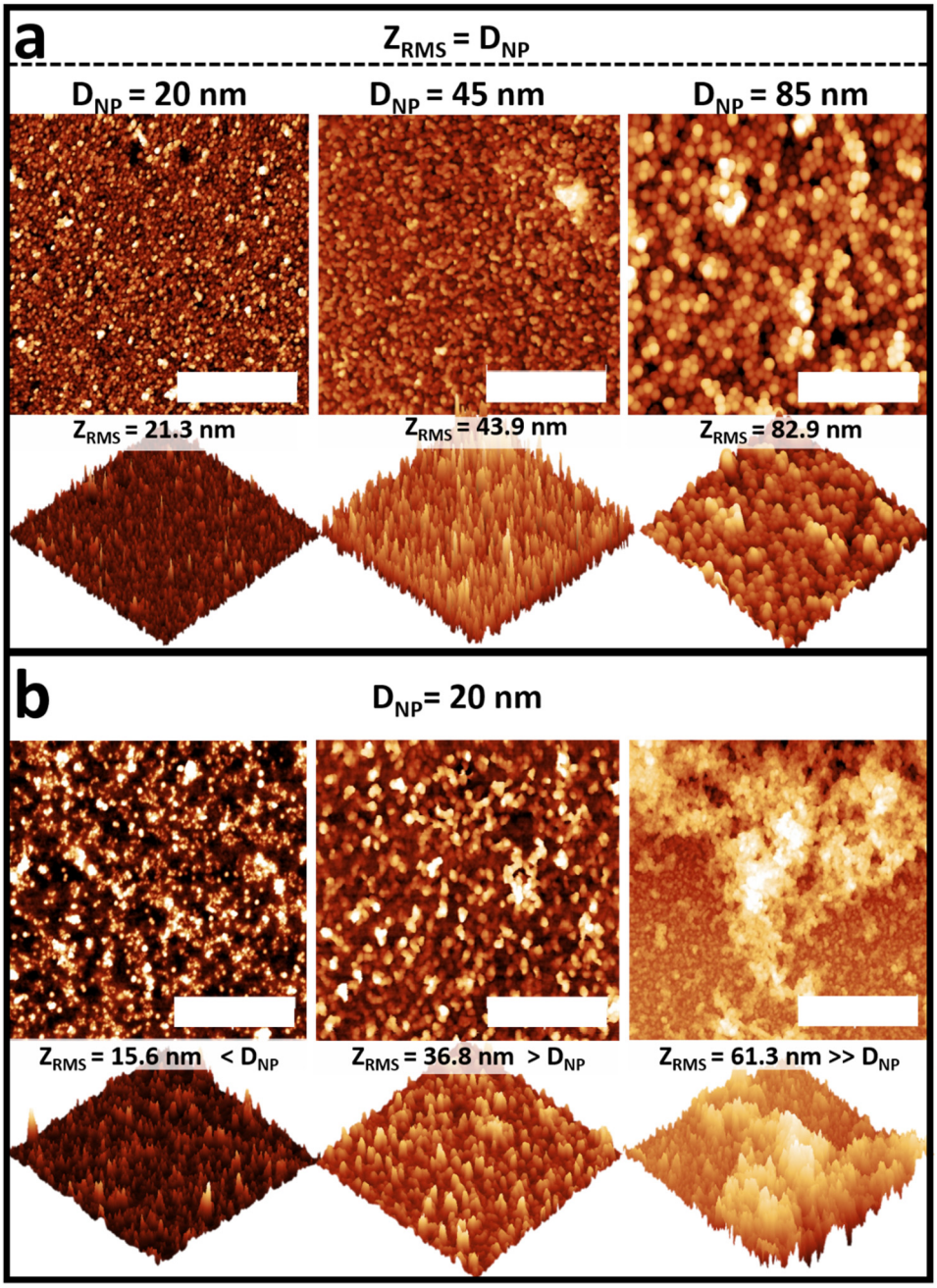

Figure 5.1. Amine-functionalized NP-decorated surfaces provide independent control of electrostatic binding strength and surface roughness. **a**. Atomic force microscopy (AFM) topographic images of self-similar surface morphologies for NPs with D_{NP} = 20 nm, 45 nm , and 85 nm (left to right). **b**. AFM topographies illustrating morphology changes as RMS roughness, Z_{RMS}, increases on surfaces composed with D_{NP} = 20 nm. As the RMS roughness increases the proximity of f-actin to the surface decreases and the mean electrostatic interaction strength between f-actin and the surface decreases. (Images are 5mm x 5mm, Z scale is adjusted for optimal contrast and is about Z_{RMS}) Scale bars are 2mm.

A transition from weak to strong binding between myosin V and actin is thought to induce structural changes in myosin which regulate nucleotide affinity and K_{ATPase}. For myosin V to be processive, the motor must maintain a high duty ratio, i.e., spend the majority of its time strongly attached to actin. To ensure that myosin V spends most of its cycle attached to actin, phosphate release and the structural change from the weakly to strongly bound state must be rapid, whereas ADP release is slow.[1] Figure 5.2e illustrates how NP-induced binding of f-actin may change the native f-actin structure, and alter the ability of myosin to strongly associate with actin to reduce K_{ATPase}. Region I illustrates tight bends in filaments that change the monomer-monomer orientation, and alter the geometry of the myosin binding cleft to impact myosin V processivity. Region II shows local areas of high potential gradient in association with NP-actin attachment sites (inset) which cause changes in the f-actin secondary structure and reduce the activity of actin as a catalyst of myosin ATP hydrolysis. The two states should be distinguishable by identifying the length and velocity of processive runs. Actin curvature induces monomer-monomer cleft changes that propagate the length of the actin filament and homogeneously reduce myosin velocity, while local denaturing of actin will lead to stops and stalls of processive runs.

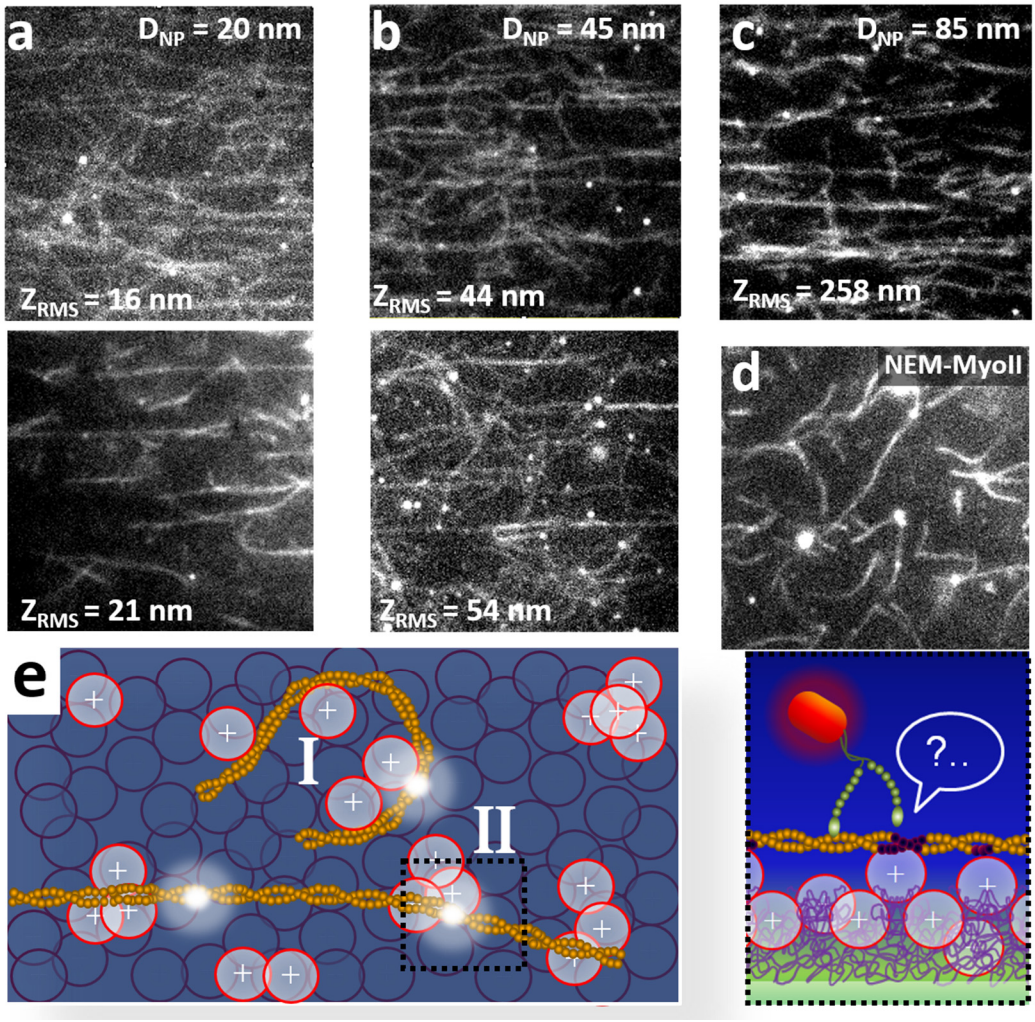

Figure 5.2: Fluorescent images of f-actin show similar filament absorption independent of nanoparticle size. a. Fluorescent (rhodamine-phalloidin) actin on D_{NP} = 20 nm nanoparticles corresponding to the left-most AFM topographies of figure 5.1a and figure 5.1b. **b.** Actin on D_{NP} = 45 nm nanoparticles with Z_{RMS} =D_{NP} (top) and Z_{RMS} > D_{NP} bottom. The top image corresponds to the middle image in figure 5.1a. **c.** Actin on D_{NP} = 85 nm nanoparticles where Z_{RMS} > D_{NP}. **d.** Images of actin on PMMA NEM-Myosin II immobilized f-actin. **e.** Schematic showing the process by which tight bends are created on surfaces of NP-immobilized f-actin. Fluorescent images are 20 mm x 20 mm. White spots are quantum dots (655 nm emission) attached to myosin V cargo domain as illustrated by figure 5.2e right.

5.2 Myosin V velocity is reduced on NP decorated surfaces

Figure 5.3a shows distance versus time plots (processive runs) of myosin V translocation on NP surfaces (D_{NP} = 20 nm, red and D_{NP} = 45 nm, black) compared to the control (green) at 200 μM [ATP]. Myosin V velocity is reduced on NP immobilized actin compared with the control.

Additionally, stops/stalls (black arrows) in translocation are equally as prevalent in runs on NP surfaces compared with the control. A homogeneous velocity reduction is consistent with structural changes in f-actin which propagate the length of the filament as opposed to localized denaturing at surface attachment sites which stop, slow, or terminate runs. High processivity of myosin V on NP surfaces, consistent with the control, indicates that the velocity reduction occurs without markedly disrupting the duty ratio of myosin V. Thus, myosin V spends the majority of its ATPase cycle strongly bound to actin indicating that the kinetics of transition from the initial weakly bound ($ADP*P_i$) state to the strongly bound (ADP) state are not greatly altered. Thus, the consistent processivity of the reduced velocity runs eliminates a reduction in phosphate release rate as a potential mechanism for the slower velocity of myosin V.

5.3 NPs enhance backwards stepping of myosin V

Since a high duty-ratio (long run length) is observed on NP immobilized f-actin, the velocity reduction may be attributed to a reduced affinity for ATP, an increased affinity for ADP, or both. Fluorescent imaging at one nanometer accuracy, FIONA, determines the distance versus time traces with sensitivity to individual steps so that the average step-size (36 nm for native myosin V) and ATP binding rate (0.9 $\mu M^{-1}s^{-1}$ for native myosin V) can be measured. Figure 5.3b shows an exemplary trace collected for myosin V translocation along f-actin immobilized on D_{NP} = 45 nm NPs at 500 nM [ATP]. Regular 36 nm translocation events and occasional backwards steps are observed. Because backwards stepping of myosin V is extremely rare on normal filaments, $p < 10^{-2}$, the observation of backwards stepping is a unique feature of NP-immobilized f-actin surfaces which induce backwards steps in the absence of external load. Backward steps indicate that the mechanism of strain-gating of the motor is disrupted by NP surfaces.

It is possible that backwards steps alone are the source of the velocity reduction, which would mean that the overall stepping rate, $k_{stepping} = k_{forward} + k_{backward}$, remains the same. The schematic in figure 5.3c illustrates how backwards stepping reduces the velocity based on the fraction of backwards steps, f_{BS}. For the label (quantum dot) on the tail domain of the motor, forward steps are measured as 36 nm displacements (figure 5.3b-c). In the event of a single backwards step the motor must take 5 forward steps to translocate a distance of 108 nm. Thus, for the illustration in figure 5.3c, the reduced velocity, $v_{Reduced}$, is 60% of the unperturbed myosin V velocity when $k_{stepping} = k_{forward}$. This scenario is sufficient to explain the observed homogeneous reduction in the velocity at 200 μM [ATP] shown in figure 5.3a, and predicts that reductions in myosin velocity on NP-immobilized f-actin occur independent of [ATP] as described by;

$$v_{Reduced} = v_o(1 - 2f_{BS}) . \qquad (5.1)$$

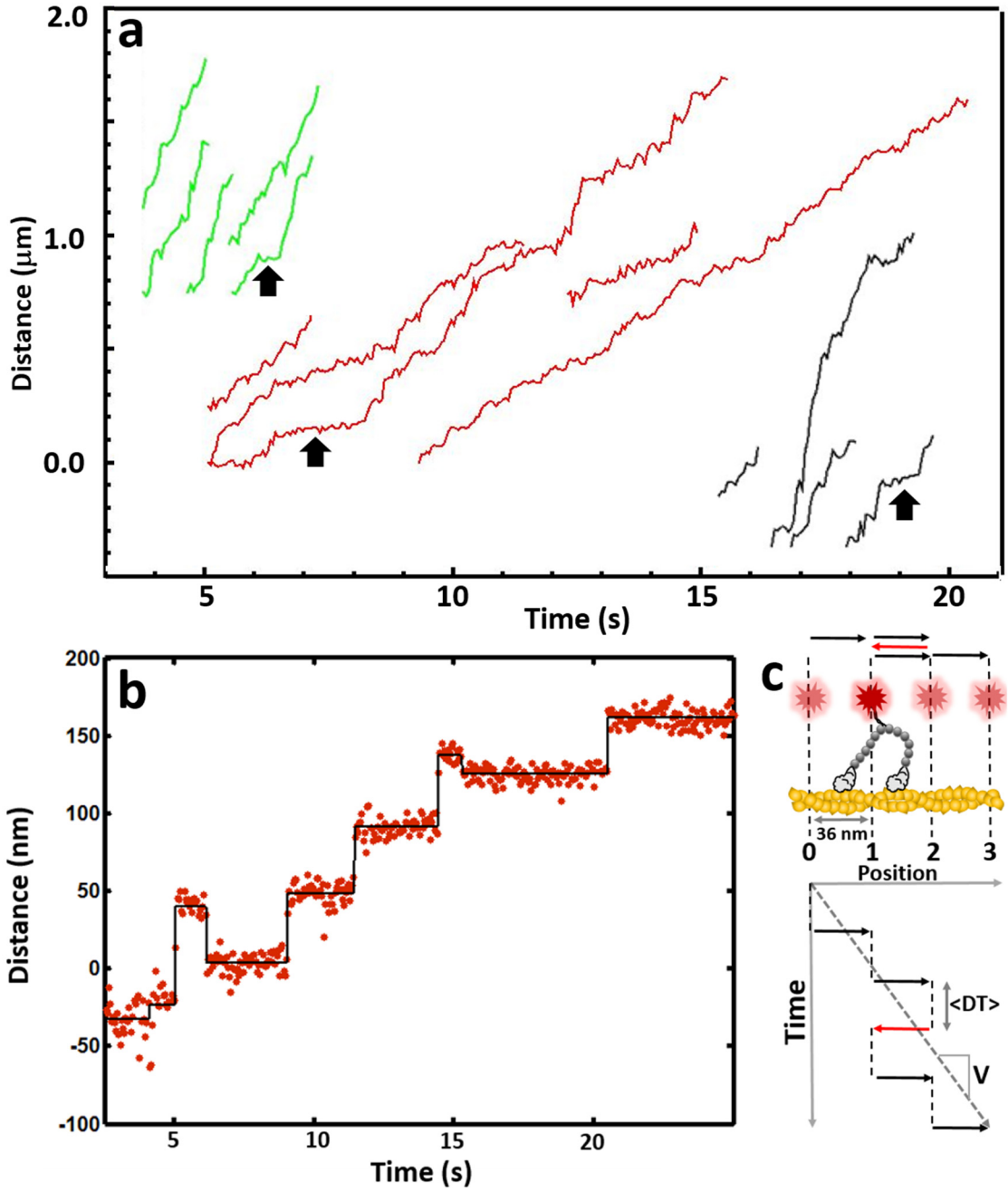

Figure 5.3: Myosin V velocity is reduced on NP-immobilized actin filaments due frequent backward steps. **a.** Distance (nm) vs time (s) plots of quantum dot-labeled myosin V trajectories along actin filaments immobilized on either D_{NP} = 20 nm (red), D_{NP} = 45 nm (black), or NEM-myosin II (control, green). **b.** FIONA trace of myosin V translocation on D_{NP} = 45 nm immobilized f-actin. Myosin V takes regular 36 nm steps and occasional backwards steps. **c.** Myosin velocity can be reduced by backwards steps alone. (Top) Illustration of 36 nm steps (black arrows) with single backwards step (red arrow). The bright spots depict the measured position (dashed black line, bottom) of myosin V determined by localization of a quantum dot attached to the tail

domain of HMM-Myosin V. (Bottom) Steps (arrows) occur after an average dwell time (<DT>) to determine corresponding velocity (dashed gray line). Backwards steps (red arrow) contribute to reduce the velocity by equation 5.1

5.4 Backwards stepping scales with D_{NP}.

To correlate the velocity reduction to surface properties, step-size distributions were collected for myosin translocation on f-actin immobilized by surfaces of different D_{NP} and the results are summarized in figure 5.4. Figure 5.4a shows the step-size distribution of the control in which backwards stepping is extremely rare, $f_{BS} < 0.01$. The distribution of forward steps agrees well with published data[3,4,10] with a mean step size, $\langle SS \rangle$, of 37.1 ± 11 nm SD. The <SS> is consistent with myosin V taking regular forward steps of 13 or 15 actin subunits. Figure 5.4b shows a step size distribution for myosin V translocating on D_{NP} = 20 nm immobilized actin. The f_{BS} = 0.10 and the distribution of backwards steps is consistent with both full and partial backwards steps where the mean backwards step size is 22 ± 11 nm. On NP-immobilized f-actin, the distribution of forward step sizes is similar to the control, $\langle SS \rangle$ of 37 ± 12 nm, indicating that the forward stride of the motor is not altered. Backwards steps indicate that the mechanism of strain-gating, whereby communication between the heads imparts high processivity, is compromised. Distributions of *SS* on surfaces of varying D_{NP} are similar (cf. figure A1.1). Figure 5.4c shows f_{BS} plotted against D_{NP}. Increasing D_{NP} leads to more backwards stepping and f_{BS} ranges from as low as 0.07 for D_{NP} = 12 nm to as much as 0.18 on D_{NP} = 85 nm surfaces. Additionally, higher surface roughness leads to a lower f_{BS}. The two data points at D_{NP} = 85 nm have a significantly different f_{BS} (cf. table A1.2). When Z_{RMS} is higher, f_{BS} = 0.15, and when Z_{RMS} is lower, f_{BS} = 0.18. The result is consistent with stronger binding of f-actin to surfaces leading to more significant disruption in myosin V stain-gating, i.e. increased f_{BS}.

The mean dwell times, $\langle DT \rangle$, of myosin V stepping determined from FIONA are shown in figure 5.4d to determine the ATP binding rate, k_{ATP+}. At 500 nM [ATP], $k_{stepping} = k_{ATP+} = \langle DT \rangle^{-1}$,

and thus the mean dwell time is an indicator of whether the ATP binding affinity of the motor is altered on NP-immobilized f-actin. In figure 5.4d, $\langle DT \rangle$ is plotted against D_{NP} and shows that athough $\langle DT \rangle$ ranges from 0.99 s to 1.5 s it does not change as a function of surface chemistry or D_{NP} relative to the control. Thus, these results indicate that NP surfaces do not change k_{ATP+} compared to the control. Using $k_{ATP+}([ATP] = 500\ nM) = \langle DT \rangle^{-1}$, k_{ATP+} is 1.8 ± 0.5 $\mu M^{-1}s^{-1}$ on NP-immobilized f-actin and 2.4 ± 0.25 $\mu M^{-1}s^{-1}$ for the control. Previous biochemical assays report k_{ATP+} = 0.9 ± 0.1 $\mu M^{-1}s^{-1}$.[18] The similar values of k_{ATP+} for the NP surfaces and the control indicate that the on-rate of myosin in the rigor state for ATP remains relatively unchanged. This supports the idea that the rigor complex of myosin V is structurally unaltered between NP assays and controls, consistent with the measured biochemical affinity of myosin V for ATP being similar for myosin bound or unbound to f-actin.[18] Since the actomyosin interaction does not change k_{ATP+} in myosin, structural alterations in f-actin induced by NP immobilization are not expected to change k_{ATP+}.

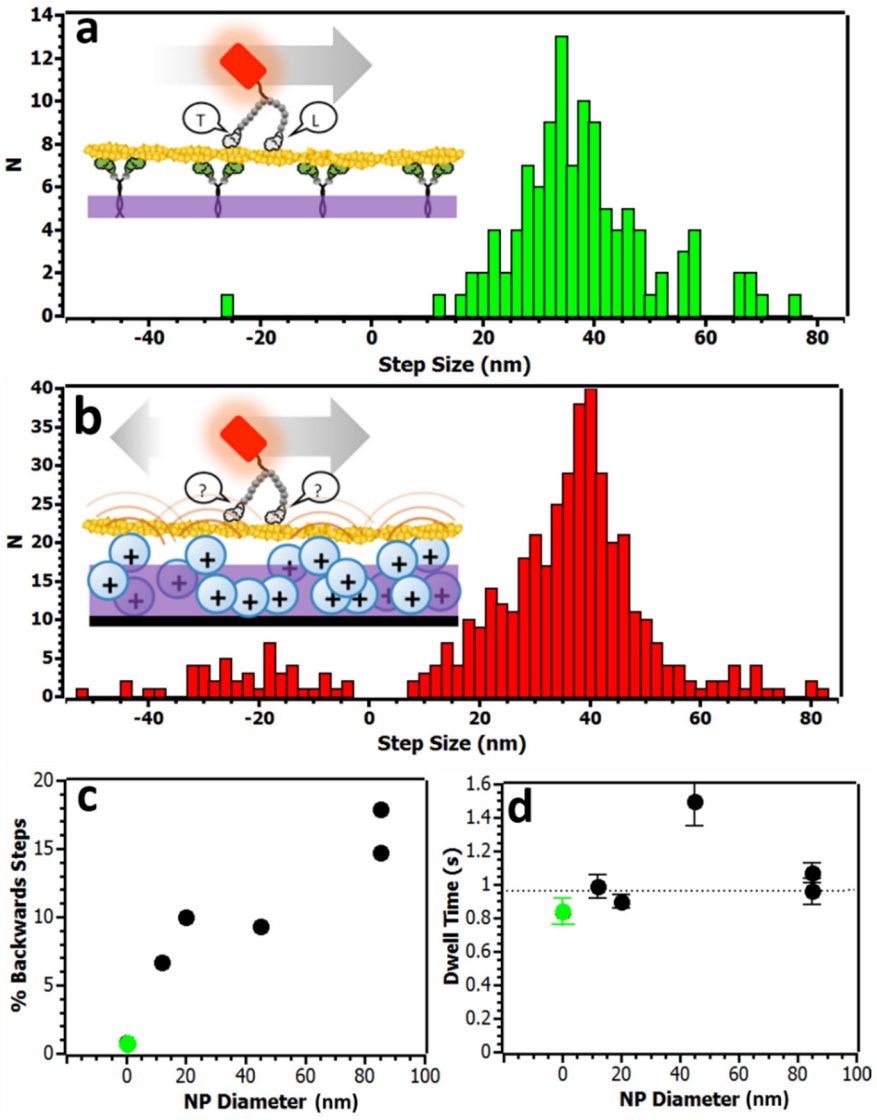

Figure 5.4: Step-size distributions of myosin V: NP-immobilization of f-actin enhances backwards stepping without changing the stepping rate, $k_{stepping}$. **a.** Step-size distribution determined for the control where f-actin is immobilized on glass slides coated with PMMA by N-Ethylmaleimide treated myosin II (NEM-MyoII) which blocks the nucleotide binding pocket of myosin leading to strong actin anchoring to surface. The inset diagram depicts the NEM-MyoII method of actin immobilization which promotes the native actomyosin interaction and full ATPase activity (velocity). In myosin V the inter-head spacing of ~36 nm enables strain-gating and inter-head communication. Strain-gating establishes asymmetry in the dimer allowing the trailing head (T) to step before the leading head (L) and myosin to consistently move forward. N = 134 **b.** Step-size distribution on D_{NP} = 20 nm immobilized f-actin, N = 441. The inset illustrates the disruption of stain gating. The leading and trailing head lose biochemical coordination and are confused about their identity (?). Either head may step first. **c.** Fraction of backwards steps ($f_{BS} = N_{FS}/N$) plotted against D_{NP}. Value of control is shown in green. **d.** Average dwell time,

<*DT*>, and standard error measured from step-size distributions on NP decorated surfaces plotted against D_{NP}. The control is placed at D_{NP} = 0 nm and colored green.

5.5 Michaelis-Menten kinetics reveal robust backward stepping behavior at all [ATP]

The hypothesis that backwards stepping leads to a reduction in velocity without a change in biochemical rate constants implies that the relative velocity reduction between NP-immobilized f-actin and the control does not depend on [ATP]. The velocity of myosin V is plotted versus [ATP] in figure 5.5 and figure 5.6. Myosin V velocity is known to follow Michaels-Menten kinetics whereby the myosin V enzyme hydrolyzes the ATP substrate by a process limited by ADP release (k_{ADP-}) at saturating [ATP] and limited by ATP binding at low [ATP].[4] The additional steps along the reaction coordinate, namely phosphate release, ATP hydrolysis, and the diffusive search time of the motor to unbind and rebind to actin are sufficiently fast so as to be ignored. Consequently, Michaelis-Menten kinetics capture myosin V velocity, and f-actin's role in catalyzing the rate of hydrolysis byproduct release. Equation 5.2 shows the Michaelis-Menten relationship for myosin V velocity as a function of [ATP], where v_{MAX} is the velocity of myosin at saturating [ATP] and K_M represents the half saturation value,

$$v(ATP) = \frac{V_{MAX}\,[ATP]}{K_M + [ATP]} \qquad (5.2)$$

The effect of backwards stepping on myosin V velocity can be evaluated by comparing experimental measurements of myosin velocity with a modified Michaelis-Menten kinetic model. In figure 5.5a the modeled effect of backwards stepping (colored lines) is compared to control data (green diamonds). The green trace indicates the best fit of equation 5.2 to the control data using V_{MAX} and K_M as independent variables with values of 478 ± 9.0 nm/s and 11.1 ± 0.9 μM, respectively. These values are consistent with previous results for myosin V under similar conditions indicating that the Michaelis-Menten curve captures the data well.

Using the values of V_{MAX} and K_M obtained from the control, multiplying equation 5.2 by equation 5.1 yields equation 5.3 which captures the effect of backwards stepping on v(ATP),

$$v(ATP) = (1 - 2f_{BS})\left(\frac{V_{MAX}\,[ATP]}{K_M + [ATP]}\right). \qquad (5.3)$$

The colored traces in figure 5.5a illustrate the effect of backwards stepping on where f_{BS} is varied from 0.05 to 0.20. Because the velocity is reduced at all [ATP], backwards stepping cannot lead to changes in K_M. The inset in figure 5.5a shows the velocity at low [ATP] where $v(ATP)$ is linear ([ATP] << K_M). In the absence of backwards stepping, the slope in the linear region is a direct measure of k_{ATP+}. Since the ATP binding rate was previously shown not to change, the reduced slope is a key signature of backwards stepping.

Figure 5.5b shows the velocity vs [ATP] (red, purple, and black symbols) for NP-immobilized f-actin where D_{NP} = 20 nm, 45 nm, and 85 nm and fixed surface roughness, Z_{RMS} ~ D_{NP} (cf. 5.1a). For these surfaces the velocity decreases as D_{NP} decreases, independent of [ATP]. The result is consistent with the data in figure 5.4c where backwards stepping increases as D_{NP} increases. This inset shows that the low [ATP] is characterized by a systematic reduction in slope as D_{NP} increases which is due to an increase in f_{BS}. Fitting the data to equation 3.5 with V_{MAX} and K_M constant as in figure 5.5a yields an estimate of f_{BS} values of 15 ± 1%, 22 ± 1%, and 27 ± 0.4% for D_{NP} of 20 nm, 45 nm, and 85 nm, respectively. However, fitting the data to the Michaelis-Menten model requires a reduction in K_M that scales inversely to D_{NP}. Fitting the data for K_M yields of 7.89 ± 1.0 μM, 8.4 ± 1.2 μM 9.15 ± 0.9 μM, respectively. (cf. table A1.1) The necessitated reduction in K_M suggests an increase in the affinity of myosin V for ADP on NP-immobilized f-actin which is consistent with a reduction in the catalytic effect of actin on myosin ATP hydrolysis. A slower ADP release rate explains the reduction in K_M, since $K_M \approx k_{ADP-}/k_{ATP+}$ and k_{ATP+} does not change, as shown in figure 5.4d.

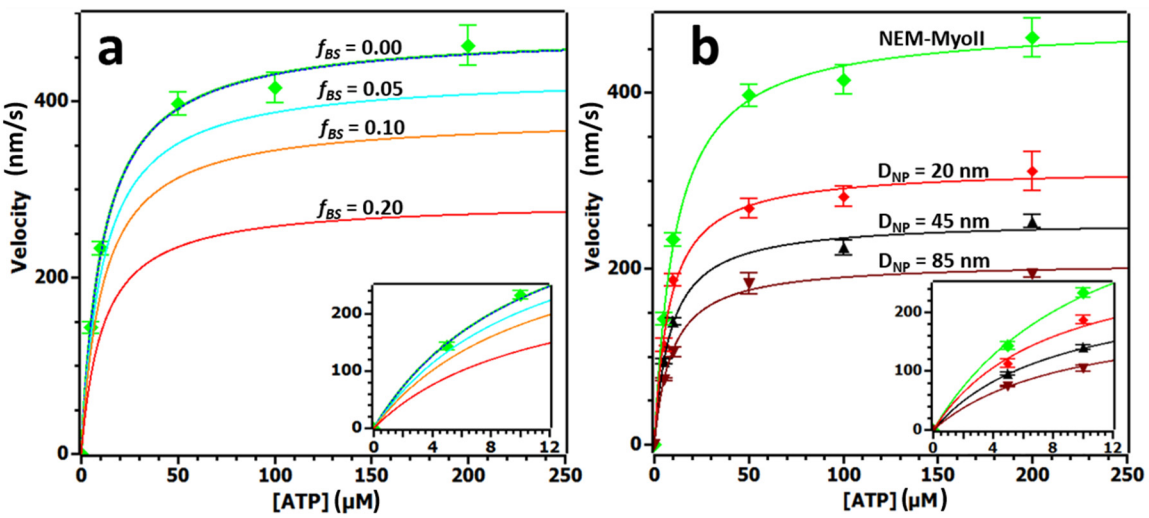

Figure 5.5: Enhanced backwards stepping of myosin V on NP-immobilized f-actin is independent of [ATP] and scales with D_{NP}. a. Modelling of Michaelis-Menten kinetics with fixed V_{Max} = 478 ± 9.0 nm/s and K_M = 11.1 ± 0.9 μM is determined by fitting control data (green symbols) The color traces show the effect of backwards stepping from 0-20% on velocity. The inset is a blow up of the low [ATP] region to show that backward stepping reduces the slope of v(ATP) where v(ATP) is linear ([ATP] << K_M). **b.** Myosin V velocity vs. [ATP] for NP-immobilized f-actin (red and black, see legend) and a control (green). Lines show fit to Michaelis-Menten kinetics where V_{Max} and K_M were adjustable variables. The inset shows the low [ATP] region of the plot where the slope is reduced, consistent with an increase in f_{BS}. Error bars show standard error. Symbols are average value of end to end velocity distribution.

5.6 Reduction of K_M on NP-immobilized f-actin is consistent with increased ADP affinity of Myosin V

To understand the effect of increasing ADP affinity on the velocity of myosin V, equation 5.3 is expanded to expose the biochemical parameters contributing to V_{MAX} and K_M. Namely, by inserting V_{MAX} = $\langle SS \rangle k_{ADP-}$ and K_M = k_{ADP-}/k_{ATP+} into equation 5.3, the velocity is given by,

$$v(ATP) = (1 - 2 * f_{BS}) \frac{\langle SS \rangle * k_{ADP-} * [ATP]}{\left(\frac{k_{ADP-}}{k_{ATP+}}\right) + [ATP]} \qquad (5.4)$$

Equation 5.4 illustrates how k_{ADP-} affects both V_{MAX} and K_M adding the additional constraint of V_{MAX} and K_M coupling through the ADP release rate. Figure 5.6 compares the velocity predicted by equation 5.4 with experimental data. The dotted blue line in figure 5.6a is the best fit of

equation 5.4 to the control data (green) which was used to determine the benchmark values of k_{ADP-} and k_{ATP+}, 13 ± 1.1 s^{-1} and 1.1 ± 0.1 $\mu M^{-1}s^{-1}$, respectively. The <*SS*> of 37.1 nm was previously determined from the mean of the step size distribution (figure 5.3a). The dependence of v(ATP) on k_{ADP-} is shown in figure 5.6a where k_{ADP-} ranges from 6 to 13 s^{-1} and f_{BS} = 0. As k_{ADP-} decreases the saturating velocity decreases. The result is a slower velocity at [ATP] > K_M while the velocity approaches the control at [ATP] << K_M (figure 5.6b) and the reduction in slope at low ATP, signature of backwards stepping (figure 5.5a, inset), is not observed. Changes in the velocity of myosin V due to NP-immobilized f-actin can be accounted for by the simultaneous contribution of backwards stepping and increased affinity for ADP (reduced ADP release rate) to lowering the velocity.

To determine if the two effects reducing the velocity could be decoupled, the strength of f-actin interaction with the surfaces was varied by changing the surface roughness at fixed D_{NP} = 20 nm (see figure 5.1b). Figure 5.6d shows v(ATP) on the control (green symbols) and three different surfaces (red symbols) where Z_{RMS} is greater than (high), equal to (medium), or less than (low) D_{NP} = 20 nm. The velocity decreases as roughness decreases. For surfaces with high and medium roughness, the velocity approaches the control velocity when [ATP] << K_M, consistent with a mechanism of reducing k_{ADP-} without producing backwards steps (figure 5.6c). However, the reduced slope at low [ATP] associated with a low roughness (Z_{RMS} < D_{NP}) indicates that this surface produces significantly more backwards stepping. Fixing <*SS*> = 37.1 nm and k_{ATP+} = 1.1 $\mu M^{-1}s^{-1}$, the experimental data is well fit by equation 5.4 (solid red traces). Table 5.1 summarizes the fit parameters of the curves in figure 5.6d to equation 5.4. Namely, when the velocity reduction is small (i.e., on rougher surfaces), reductions in k_{ADP-} can account for reductions in v(ATP), whereas greater velocity reductions (bottom red trace) require backwards stepping to account for reduced v(ATP). This finding is significant because it suggests that a

weaker electrostatic interaction decreases the ability of f-actin to catalyze myosin V ADP release, whereas stronger interactions further act to disrupt strain gating leading to backwards stepping.

Surface	f_{BS} (%)	k_{ADP-} (s^{-1})	K_M (μM) *	V_{MAX} (nm/s) *
20 nm High	0.3 ± 0.5	10.66 ± 1.5	6.7 ± 1.5	156 ± 8.5
20 nm Mid	1.0 ± 0.6	8.68 ± 1.1	7.89 ± 1.0	314 ± 8.7
20 nm Low	24.6 ± 0.2	8.32 ± 0.9	9.69 ± 1.3	393 ± 14
* *Values calculated from fit parameters*				

Table 5.1: Summary of fit parameters and effective f_{BS}, k_{ADP-}, K_M, and V_{MAX} obtained by fitting myosin V velocity data to equation 5.4. Error is determined from fits in figure 5.6d.

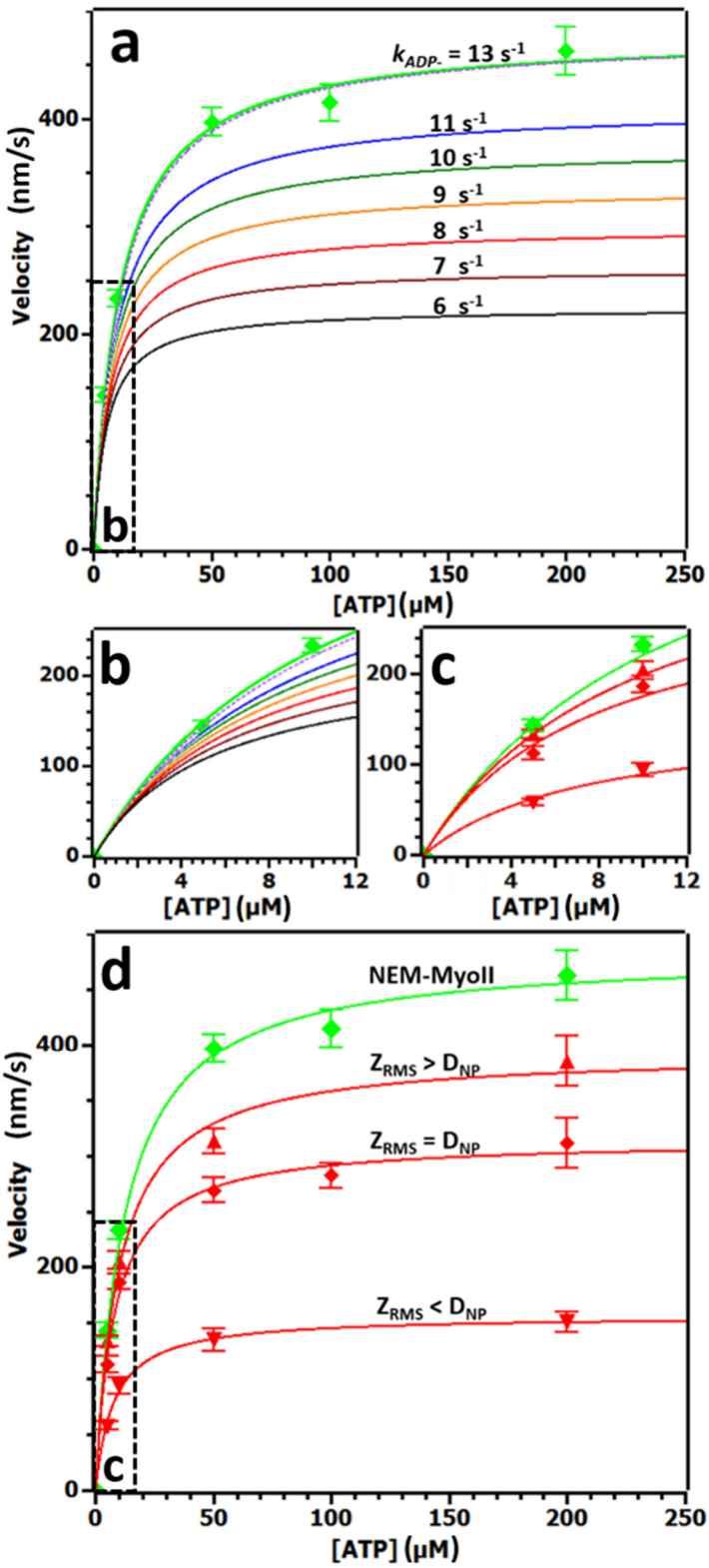
a
k_{ADP-} = 13 s^{-1}
11 s^{-1}
10 s^{-1}
9 s^{-1}
8 s^{-1}
7 s^{-1}
6 s^{-1}
Velocity (nm/s)
[ATP] (μM)
b
c
d
NEM-MyoII
$Z_{RMS} > D_{NP}$
$Z_{RMS} = D_{NP}$
$Z_{RMS} < D_{NP}$

Figure 5.6: Coupling V_{MAX} and K_M through k_{ADP-} indicates that NP-immobilization of actin increases myosin V ADP affinity and induces backwards stepping through separate mechanisms. a. Modelling the effect of reducing k_{ADP-} on v(ATP). Green data (control) is fit to equation 5.2 (green trace) and equation 4 (dashed trace) with fixed $\langle SS \rangle$ = 37.1 nm, k_{ATP+} = 1.1 $mM^{-1}s^{-1}$, and f_{BS} = 0. Best fit k_{ADP-} = 13 ± 1.1 s^{-1}. Colored traces show the effect of decreasing k_{ADP-} systematically (see legend). Inset (bottom left) shows slope change at low [ATP] does not occur with k_{ADP-} which determines both K_M and V_{MAX}. **b**. Average velocity measured on D_{NP} = 20 nm surfaces with Z_{RMS} greather than (high), equal to (middle), or less than (low) D_{NP}. Data points consist of average end-end velocity from N > 100 runs each, error bars mark standard error of mean. Solid traces are fits to equation 5.4 for f_{BS} and k_{ADP-} .

5.7 Induced backwards stepping and reduced K_M suggest coupled nucleotide affinity and power-stroke in myosin V

Figure 5.7 shows the kinetic cycle for myosin V attached to NP-immobilized f-actin. In the native binding between actin and myosin, (figure 5.7a) strain-gating between the heads caused by the strongly bound pre-power-stroke state reduces the k_{ADP}- of the leading head resulting in trailing head ADP release, subsequent ATP binding, and detachment of the trailing head. A forward step occurs and myosin arrives in the weakly bound pre-power stroke state (figure 5.7b) where rapid phosphate (P) dissociation in the leading head leads to the strongly bound pre-power-stroke state (figure 5.7c) similar to that of figure 5.7a. However, in the NP-immobilized case (NP drawn to illustrate association) the strain between the heads does not evolve (or dissipates) leading to similar probability of ADP release from both the trailing and leading head. This in turn leads to two possible states of myosin V (figure 5.7d) whereby the trailing or the leading head releases ADP first leading to subsequent ATP binding, detachment, and stepping of that head. When the leading head steps first (figure 5.7d, top) myosin can step backwards, or return to its original position (foot stomp) to continue its run. When the trailing head steps first the general consequence is a forward step.

The consequences of electrostatic immobilization of f-actin on myosin V motility are illustrated in figures 5.7c and 5.7d. The observation of backwards stepping indicates that

coordination between the leading and trailing heads is reduced, i.e., a loss of gating. The loss of gating may indicate a reduction in inter-head strain which would arise from either a structural alteration in the actin permitting relaxation of strain during the power stroke or decreased rigidity of the "persistence length compromised" f-actin leading to filament buckling under inter-head strain. The effect of backwards stepping in reducing the overall velocity is explained by equation 5.1; however, the biomechanical mechanism permitting leading head detachment, figure 5.7d top, mandates that the leading head be able to release ADP at a rate comparable to the trailing head (figure 5.7c). This predicts that after accounting for backwards stepping (equation 5.4) the observed k_{ADP}- would be increased (by as much as a factor of 2) leading to a measurable increase in K_M by fitting equation 5.3 or equation 5.4 to v(ATP) data, (figures 5.5 and 5.6). The results show a clear decrease in K_M that is well approximated by a decrease in $k_{ADP\text{-}}$. The fits to data in figure 5.6b indicate that a decrease in $k_{ADP\text{-}}$ accounts for minor velocity reductions before f_{BS} is significant and further decreases in velocity occur by backward stepping with little change in $k_{ADP\text{-}}$. Therefore, the reduction in ADP release rate and the loss of inter-head gating arise from independent (possibly related) mechanisms due to structure changes in f-actin altering actomyosin.

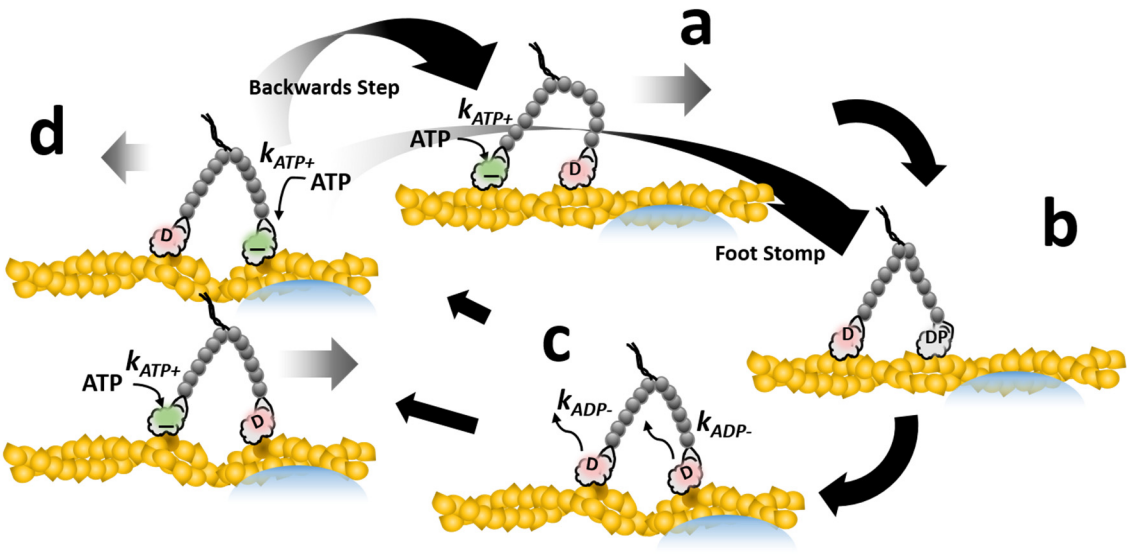

Figure 5.7: NP-immobilized f-actin enhances backwards stepping and reduces k_{ADP-} of myosin V. **a.** Native state of myosin V shown with leading head in partial power-stroke whereby strain between the heads leads to preferential ADP release from the trailing head and subsequent ATP binding. **b.** Immediately after a forward step, myosin V adopts its pre-power-stroke, weakly bound complex, from which phosphate release (P) is rapid. **c.** NP-immobilized f-actin shows reduced strain-gating. Consequently ADP can release from either head leading to a faster measured ADP release due to two sites. **d.** Myosin V enters two possible states from c to d. (Top) leading head releases ADP first which leads to leading head detachment and either a foot stomp or backwards step. (Bottom) Trailing head releases ADP first leading to a forward step.

As the myosin catalytic head progresses along its ATPase cycle, its interaction with actin becomes stronger. In the final steps before rigor, coordination of myosin V with actin in the strong binding complex triggers conformational changes in the switch II region which leads to tilting of the lever arm through coupled motions of the myosin relay-helix generating strain between heads.[20] The inter-head strain inhibits a cascade of conformational changes that lead to ADP release and the rigor structure. These conformation changes, namely coordinated motion of the seven-stranded β-sheet, switch I, and the P-loop, are the rate limiting step in the myosin V ATPase cycle, k_{ADP-}, and ensure a high duty ratio commensurate with processivity.[1,21-24] Defects in the actin structure which reduce the ability of myosin to fully coordinate with f-actin can reduce propagated structural changes in myosin. Namely, motion of the switch II region has

been shown to be coupled to the actin binding region of myosin and switch II is to coupled lever-arm tilting and inter-head strain. A reduction of switch II motion can lead to reduced inter-head strain which accounts for the appearance of backward steps since strain prevents leading head ADP dissociation (and subsequent detachment from actin and a backward step, figure 5.7d). Similarly, reduced switch II motion reduces k_{ADP-} because switch I, which regulates nucleotide affinity, is directly coupled to switch II through a salt bridge as the proposed mechanism regulating ADP release.[20] Thus, k_{ADP-} will approach the actin-dissociated value of 1.2 s^{-1}, roughly 10x slower than the actin-associated state, 12 s^{-1}.[18] The observed roughly 4 fold decrease in k_{ADP-} (2-fold from curve fitting, 2-fold illustrated by figure 5.7c) indicates the presence of a partial reduction in catalysis of myosin ADP release (1.2 s^{-1} < k_{ADP-} < 12 s^{-1}) along the entire length of the actin filament or a complete loss of catalysis, k_{ADP-} = 1.2 s^{-1}, occurring specifically at NP-associated regions of the actin filament. The lack of stops/stalls in myosin runs suggests a partial reduction of k_{ADP-} occurs by a reduced coordination between actin and myosin along the entire length of the actin filament. However, direct resolution of the effect is not currently possible.

5.8 Conclusion

Herein the effect of non-specific binding of f-actin by electrostatic interaction to NP-decorated surfaces is shown to reduce filament persistence length and myosin V velocity. The mechanism of myosin V velocity reduction imparts backwards stepping without compromising run length (cf. figure 5.3a) or changing the ATP binding rate (cf. figure 5.4d). The fraction of backwards stepping f_{BS} is shown to increase with the diameter of NP used in immobilizing f-actin which is consistent with previously shown results that enzymes absorbed to NPs lose activity in a fashion that increases with D_{NP}. Plotting v(ATP) and fitting to the Michaelis-Menten equation adjusted for backwards stepping (equation 5.3) for surfaces of different D_{NP} shows reductions in

velocity consistent with an increase in backwards stepping as well as a clear reduction in K_M. Expanding the equation to account for ADP release kinetics shows that velocity reductions are well captured by a combination of reduced k_{ADP-} and backwards stepping. Plotting v(ATP) and fitting with equation 5.4 shows that k_{ADP-} is reduced significantly (~35%) on surfaces even in the absence of significant f_{BS}. This is consistent with a mechanism that disrupts the coordination of the strong binding complex of actomyosin in which actin catalyzed structural changes in myosin affect both the power-stroke conformation and nucleotide affinity simultaneously. The observation of two distinct effects, K_M and f_{BS}, supports the hypothesis that the progression of myosin V into the strong binding state with f-actin results in propagated structural changes in the switch II region that regulates nucleotide affinity through coordination with the switch 1 region and induces force-generation between heads through coupling with the relay helix that leads to inter-head strain. The paper shows that small perturbations in f-actin structure can greatly affect myosin ATPase activity.

5.9 References

1. Sweeney HL, Houdusse A, Structural and Functional Insights into the Myosin Motor Mechanism, *Annu Rev Biophysics*, 39, **2010**, 539-557.
2. Mehta AD, Rock RS, Rief M, Spudich JA, Mooseker, Cheney RE, Myosin-V is a processive actin-based motor, *Nature*, 400, 5, **1999**, 590-593.
3. Yildiz A, Forkedy JN, McKinney SA, Ha T, Goldman YE, Selvin PR, Myosin V Walks Hand-Over-Hand: Single Fluorophore Imaging with 1.5-nm Localization, *Science*, 300, **2003**, 2061-2065
4. Forkey JN, Quinlan ME, Shaw A, Corrie JET, Goldman YE, Three-dimensional structural dynamics of myosin V by single-molecule fluorescence polarization, *Nature*, 422, **2003**, 399-404.
5. Sellers JR, Veigel C, Walking with myosin V, *Curr Opinion Cell Biol*, 18, 1, 2006, 68-73.
6. Veigel C, Wang F, Bartoo ML, Sellers JR, Molloy JE, The gated gait of the processive molecular motor, myosin V, *Nature Cell Biology*, 4, **2001**, 59-65.
7. Homma K, Saito, Ikebe R, Ikebe M, Ca^{2+} - dependent Regulation of the Motor Activity of Myosin V, *JCB*, 275, **2000**, 34766-34771.
8. Park JH, Sun Y, Goldman YE, Composto RJ, Self-assembled charged hydrogels control the alignment of filamentous actin, *Soft Matter*, 6, **2010**, 915-921.
9. Caporizzo MA, Sun Y, Goldman YE, Composto RJ, Nanoscale Topography Mediates the Adhesion of F-Actin, *Langmuir*, 28, **2012**, 12216-12224.

10. Rief M, Rock RS, Mehta AD, Mooseker MS, Cheney RE, Spudich JA, Myosin-V stepping kinetics: A molecular model for processivity, *PNAS*, 97, 17, **2000**, 9482-9486.
11. Watanabe TM, Iwane AH, Tanaka H, Ikebe M, Yanagida T, Mechanical Characterization of One-Headed Myosin-V Using Optical Tweezers, *PLoS ONE*, **2010**, 5, 8, e12224.
12. Oguchi Y, Mikhailenko SV, Ohki T, Olivares AO, De La Cruz EM, Ishiwata S, Load-Dependent ADP binding to myosins V and VI: Implications for subunit coordination and function, *PNAS*, 105 22, **2008**, 7714-7719.
13. Clemen A E-M, Vilfan M, Jaud J, Zhang J, Barmann M, Rief M, Force-Dependent Stepping Kinetics of Myosin-V, *Biophysical Journal*, 88, **2005**, 4402-4410.
14. Sellers JR, Veigel C, Direct observation of the myosin-Va power stroke and its reversal, *Nature Structural and Molecular Biology*, 17, 5, **2010**, 590-595.
15. Vertegel AA, Siegel RW, Dordick JS, Silica Nanoparticle Size Influences the Structure and Enzymatic Activity of Adsorbed Lysozyme, *Langmuir*, 20, **2004**, 6800-6807.
16. Pan H, Qin M, Cao Y, Wang W, How do proteins unfold upon adsorption on nanoparticle surfaces, *Langmuir*, 28, **2012**, 12779-12787.
17. Stueker O, Ortega VA, Goss GG, Stepanova M, Understanding Interactions of Functionalized Nanoparticles with Proteins: A Case Study on Lactate Dehydrogenase, *Small*, 10, 10, **2014**, 2006-2021.
18. De La Cruz EM, Wells AL, Rosenfeld SS, Ostap EM, Sweeney HL, The kinetic mechanism of myosin V, *PNAS*, 96 24, **1999**, 13726-13731.
19. Vikhorev PG, Vikhoreva NN, Mansson A, Bending Flexibility of Actin Filaments during Motor-induced Sliding, *Biophysical Journal* 95, **2008**, 5809-5819.
20. Trivedi DV, David C, Jacobs DJ, Yengo CM, Switch II Mutants Reveal Coupling between the Nucleotide- and Actin-Binding Regions in Myosin V, *Biophysical Journal*, 102, **2012**, 2545-2555.
21. Burgess S, Walker M, Wang F, Sellers JR, White HD, Knight PJ, Trinick J, The prepower stroke conformation of myosin V, *JCB*, 159 6, **2003**, 983-991.
22. Coureux P-D, Wells AL, Menetrey J, Yengo CM, Morris CA, Sweeney HL, Houdusse A, A structural state of the myosin V motor without bound nucleotide, *Nature*, 425 25, **2003**, 419-424.
23. Sun M, Oakes JL, Ananthanarayanan SK, Hawley KHJ, Tsien RY, Adams SR, Yengo CM, Dynamics of the Upper 50-kDa Domain of Myosin V Examined with Fluorescence Resonance Energy Transfer, *JBC*, 281, **2006**, 5711-5717.
24. Holmes KC, Angert I, Kull FJ, Jahn W, Shroder RR, Electron cryo-microscopy shows how strong binding of myosin to actin releases nucleotide, *Nature*, **2003** 423-427.
25. Lorenz M, Holmes KC, The actin-myosin interface, *PNAS*, 107, 28, **2010**, 12529-12534.

Chapter 6: Correlating Viscoelasticity with Metabolism in Single Cells using Atomic Force Microscopy

6.0 Introduction

The viscoelasticity of a cell reflects its function in an organism. Migratory cells, such as macrophages or neutrophils are compliant, whereas osteoblasts that generate bone are stiff.[1] An interplay between the mechanical properties of cells and their environment is crucial to maintaining homeostasis such that viscoelastic changes in cells are associated with disease. [2-4] In particular, the two leading causes of death in the United States, coronary artery disease and cancer[5], progress by mechanical changes in tissue. First, coronary artery disease (CAD), caused by the mechanical stiffening of the vascular system, can occur by elastin depletion, collagen deposition, endothelial cell dysfunction, hypercholesterolemia, or hormonal imbalance.[3] Clinically, the pathological trigger responsible for the stiffness change is difficult to identify because arteriosclerosis is identified by a single symptom, isolated systolic hypertension.[3] Second, tumors are stiffer relative to surrounding tissue which enables their growth,[4] while the metastatic transformation of malignant cells, that ultimately determines cancer lethality, is directly associated with cellular mechanical softening[6-8]. In particular, intravasion and extravasion of cancer cells require extensive cytoplasmic deformation and are thusly associated with a reduction in both the stiffness and viscosity of the cytoplasm.[4,6] Atomic force microscopy (AFM) can distinguish metastatic cancer at the single cell level by cell stiffness[7]. Here, AFM is shown to be sensitive to metabolic changes in cells by quantifying multiple viscoelastic

parameters, namely, viscosity, relaxation time, and stiffness, using variable indentation-rate rheometric analysis by Laplace transform, VIRRAL.

The complex elastic modulus of bulk soft materials, such as gels and tissue, is measured at the macroscopic level using rheometry.[9, 10] To measure viscoelasticity in single cells, techniques such as micropipette aspiration[11], optical trapping[12, 13], and atomic force microscopy[4, 14-19] combine micrometer to nanometer spatial resolution with piconewton force sensitivity. Using the atomic force microscope to measure the creep of cells, cell phenotypes are distinguished by their viscoelastic properties[14], and cancer progression is linked to a decrease in single-cell stiffness and viscosity.[15,17] Changes in keratin[20] and other intermediate filament expression lead to mechanical property changes associated with disease.[21] Within a cell, the degree of actin polymerization is shown to be the primary factor determining cytoskeletal stiffness and viscosity.[16] Degree of actin polymerization (i.e. f-actin concentration) is linked to metabolism through the ATP/ADP ratio[22] which suggests that cell stiffness scales inversely with metabolic rate. Although, metabolic changes are a hallmark of diseases such as cancer[23], a link between viscoelastic changes and cell metabolism is lacking.

To maximize efficiency, cells compartmentalize their processes and, therefore, viscoelasticity is spatially heterogeneous across the cell. For example, the leading edge of a migrating cell exhibits treadmilling of densely branched f-actin, while the f-actin concentration in the cytoplasm decreases.[2] Nuclear viscoelasticity, which is greater than cytoplasmic viscoelasticity, is determined by the organization and expression of a family of proteins known as lamins.[24] Cell-cell and cell-matrix adhesions are mediated by the expression of integrins which are overexpressed in tumor cells.[25]The spectrin family of proteins is responsible for cell shape and membrane pretension that provides neurons with their elasticity.[26] Consequently, spatially resolved measurements of viscoelasticity in specific areas on individual cells are

required to complete the picture of cell health and the ongoing processes that correlate with the onset and progression of disease.

Herein, a scanning probe technique based on atomic force microscopy is extended to accurately determine cell viscoelastic parameters with sub-micron spatial resolution. Variable indentation-rate rheometric analysis by Laplace transform (VIRRAL) has advantages over force displacement (creep) measurements because indentation curves are used to obtain spatially resolvable frequency sweeps. VIRRAL demonstrates how the viscoelasticity of the cytoplasm of THP-1 cells indicates metabolic dysfunction induced by silver NPs. The efficacy of novel dextran-lysozyme drug carriers (Dex-Gels) is evaluated at the sub-cellular level using VIRRAL. In particular, an increase in cytoplasmic stiffness and viscosity is detected after endocytosis of rhodamine B or Ag nanoparticle loaded Dex-Gels, while no change in stiffness occurs for the uptake of unloaded Dex-Gels compared to a control. The lack of viscoelastic change in THP-1 cells treated with unloaded Dex-Gels indicates that Dex-Gels are non-toxic and their presence in the cytoplasm does not affect cytoskeletal viscoelasticity. The increase in viscoelasticity correlates with metabolic stress induced by Ag Dex-Gels and confirmed by a fluorescence activity assay. These results are significant because they correlate metabolic changes in cells relevant to diseases with viscoelasticity that can be detected at the single cellular level using AFM.

6.1 Indentation Profile and Indenter Shape effect measured modulus.

Polyacrylamide gels (PAGs) with varying elastic moduli were synthesized to connect well-established bulk measurements of shear modulus to AFM nano-indentation measurements of elastic modulus. PAGs were formulated using various combinations of acrylamide and bis-acrylamide concentrations to generate a range of gels with elastic moduli that span two orders

of magnitude in a biologically relevant range (100 Pa – 60 kPa).[27] Figure 6.1a shows how the elastic shear modulus G' (closed symbols) and loss shear modulus G'' (open symbols) depend on frequency. A plateau of G' is observed between 0.1 and 10 Hz for all PAGs. This plateau modulus increases from 25 to 13000 Pa as the gel cross-linking density increases. For all PAGs tested, G" is an order of magnitude smaller than G' which indicates that the gels behave as elastic solids. A comparison between G'=2.5 kPa and the corresponding G" (open circles) in figure 6.1 represents the relative magnitude difference between G' and G" in all of the PAGs.

In AFM nano-indentation, cantilever deflection I used to determine the magnitude of the complex elastic modulus $|\varepsilon| = |\varepsilon' + i\varepsilon''|$, where ε' is the elastic component and ε'' is the loss component of the modulus. The elastic modulus (ε) is directly related to the shear modulus (G) by Poisson's ratio (ν) which is 0.48 ± 0.12 for PAG. (cf., equation 6.1)[28] Because G''<< G' for PAG, G" does not contribute to ε and AFM measurements can be directly compared to bulk rheometry by G',

$$\varepsilon = 2G'(1 + \nu)\,. \qquad (6.1)$$

The modulus measured by AFM nano-indentation (and other methods) depends on the waveform of the probing signal, which is called the indentation profile. Parallel plate rheology uses a sinusoidal shear indentation profile to independently determine the elastic and loss shear moduli. In contrast, AFM nano-indentation uses a constant cantilever velocity (V) which has a saw-tooth (triangle wave) indentation profile whose amplitude (A) is the indentation depth into the material (cf., figure 6.1b). The fundamental frequency of the triangle wave is determined by V and A, $\omega = \pi V/A$ rad/s. A triangle wave equates to the sum of a series of sinusoidal indentation profiles with decreasing periods and amplitudes related to integer multiples of ω. The high frequency harmonics have smaller amplitude than the fundamental frequency;

however, the modulus is typically independent of amplitude. Higher frequency harmonics therefore contribute as much at the fundamental frequency for the triangle wave indentation profile. Thus, when a material exhibits a frequency dependent modulus, such as PAGs at frequencies above 10 Hz (figure 6.1a) and cells, [12] a triangle wave indentation profile can overestimate the modulus compared to a sinusoidal profile at the same frequency.

AFM nano-indentation measurements of $|\varepsilon|$ systematically overestimate the modulus values determined by parallel plate rheology of the same PAGs as shown in figure 6.1c. Equation 1 is used to convert the shear moduli into elastic moduli so that measurements using the triangle wave indentation profile can be compared to the sinusoidal indentation profile (figure 6.1c). The triangle wave indentation profile has a fundamental frequency of ω_f = 6 rad/s and indents the surface with (red triangles) or without (blue circles) a sinusoidal overtone modulation of ω_o = 6 krad/s (cf. figure 6.1b). In this regime, amplitude does not contribute to modulus measurements. Thus, if the 6 krad/s overtone of the 6 rad/s triangle wave already contributes to the modulus measurement, the two sets of AFM data should agree with each other. Figure 6.1c shows the blue circles and red triangles are similar values of the modulus and together overestimate the modulus in comparison to parallel plate rheology (black squares, dotted line). Thus, higher sinusoidal harmonics associated with the triangle wave indentation profile are found to influence modulus measurements of PAGs giving rise to a systematic overestimation of the elastic modulus. Despite potential complications, a triangle wave indentation profile is used here because it is the more commonly used profile for measuring the modulus of cells by AFM and therefore allows for direct comparison with prior AFM nano-indentation measurements.

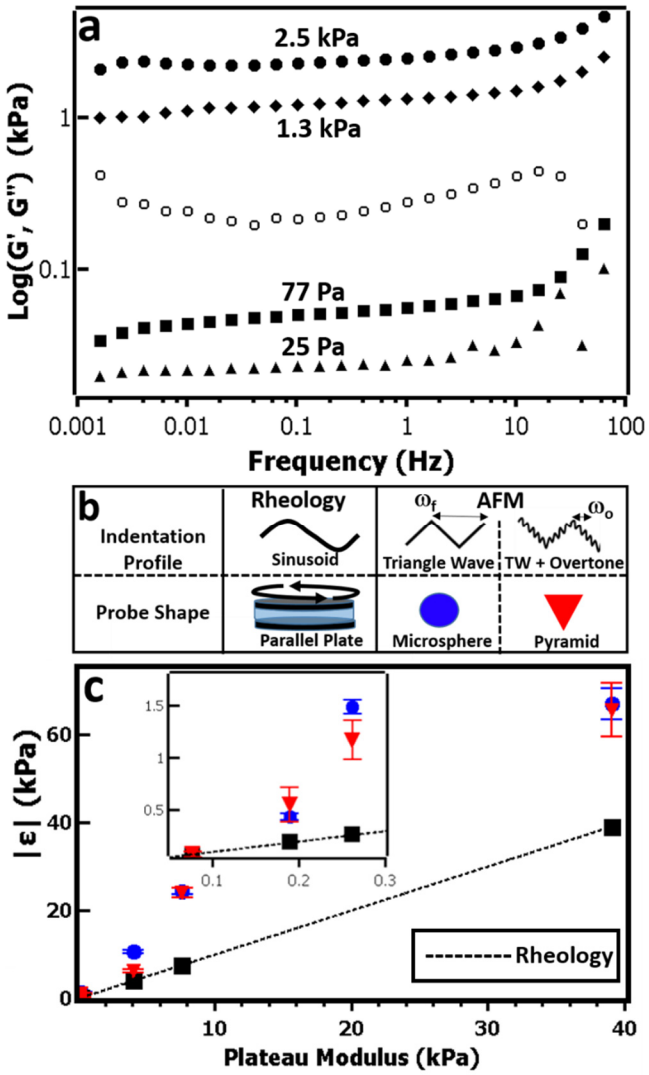

Figure 6.1: Modulus of Polyacrylamide Gels. a. The bulk shear modulus is determined as a function of frequency by parallel plate rheology. The real (elastic) component of the modulus, G', (closed symbols) is resolved from the complex (loss) component of the modulus, G" (open symbols). The modulus value at which the elastic component remains relatively unchanged with frequency is known as the plateau modulus, and occurs for all PAGs between 0.01 and 10 Hz. The loss modulus is shown for the PAG exhibiting a plateau modulus of 2.5 kPa displays a mean value of 286 Pa. In all cases G' << G" indicating PAGs behave as elastic solids. **b.** The value of the plateau modulus (rheology) is compared to AFM measurements using microsphere (blue circles) indenter or a pyramid-shaped indenter with a 1 kHz overtone (red triangles). The agreement of the two values suggests that indenter shape is not important for modulus determination of PAGs but that the difference in indentation profile between rheology and AFM leads to AFM overestimating the modulus compared to rheology. **c.** Diagram comparing rheology and AFM for modulus characterization highlighting the key parameter differences: indentation profile and probe shape.

The consistent agreement between modulus values measured with a spherical indenter (blue circles) and a pyramidal indenter (red triangles) indicates that tip shape (pyramidal or spherical) does not affect the modulus measurements of the PAGs. A sharp tip (conical) concentrates stress over a small area leading to modulus overestimation and reduced instrument sensitivity in cells, while the agreement between AFM data sets in figure 6.1c, regardless of PAG stiffness, suggests that PAG modulus is equivocally determined regardless of indenter shape. Spherical tips are shown to provide more accurate modulus measurements of cells than sharp tips.[29] Furthermore, the concentration of stress at the tip of a sharp indenter can irreversibly damage cells and poke through the membrane. For this study, two micron diameter silica spheres were attached to AFM cantilevers because they optimally balance spatial precision and force sensitivity.

6.2 The morphology of THP-1 cells containing Dex-Gels

The modulus of single cells is measured and correlated with cell state. THP-1 cells were chosen for their ability to differentiate into macrophage-like cells that will ingest a novel hydrogel carrier (Dex-Gel). Dex-Gels consist of a lysozyme inner core cross-linked with a dextran coating to form a 150 nm diameter nanoparticle that is digestible, capable of delivering drugs to cells, and suitable for grafting specific proteins for targeted cell delivery.[30] Three variations of Dex-Gels are used: (1) blank dextran-lysozyme nanoparticles (Dex-Gel) to test carrier toxicity; (2) rhodamine-labeled dextran-lysozyme particles (Rd Dex-Gel) to track uptake and degradation by fluorescent microscopy; and (3) silver nanoparticle (d = 5 nm) loaded dextran-lysozyme particles (Ag Dex-Gel) which can stress and kill THP-1 cells. Cells were exposed to Dex-Gels (20 μg/mL) for a 24 hr incubation period and then imaged.

Figure 6.2 shows optical micrographs of the AFM cantilever (dark triangle) above a representative macrophage from THP-1 cell populations whose morphologies are, well spread (normal), spoke-like in shape, or elongated. Spherical cells that adhere poorly to the coverslip are rare (<5%) in all populations and are not counted. The control THP-1 cells (figure 6.2a) unexposed to Dex-Gel are well spread and adhere to the coverslip. Dex-Gel treated cells (figure 6.2b) are similar in morphology to untreated THP-1 cells and exhibit the fewest percentage of cells with a spoke-like morphology (14%) and highest percentage of well spread cells (52%). Rd Dex-Gel treated cells (figure 6.2c) appear morphologically similar to untreated cells having a similar number of spoke-like cells (25%). The population of Ag Dex-Gel treated cells exhibits the largest percentage of spoke-like cells (43%) such as the cell shown in figure 6.2d (cf. figure A2.1).

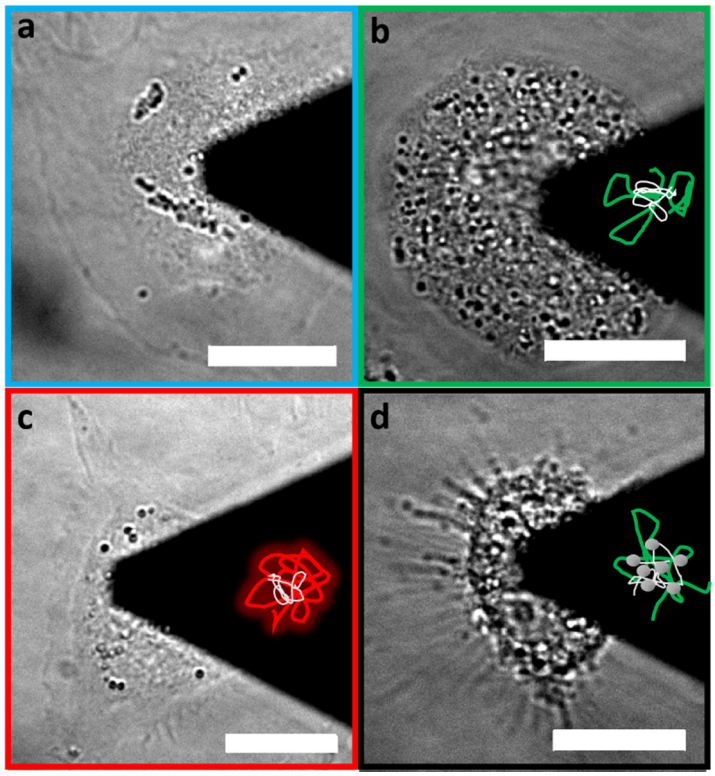

Figure 6.2: Optical micrographs of THP-1 cells which exhibit treatment dependent morphology. a. Untreated Macrophages (Control) **b.** Unloaded lysozyme-dextran conjugate nano-gel drug carriers (Dex-Gel) are exposed to macrophages for 24 h prior to imaging **c.** Rhodamine labeled dextran (Rd Dex-Gel) nanogels are exposed to macrophages 24 h prior to

imaging. **d.** Dex-Gel is seeded with a silver precursor to yield 5 nm silver nanoparticles within its core (Ag Dex-Gel) and macrophages are exposed to Ag Dex-Gels 24 h prior to imaging. A schematic of each drug/carrier complex is drawn inset, a top the AFM cantilever (black triangle). Scale bars are 20 μm.

6.3 THP-1 cell stiffness differs between nuclear, cytoplasmic and peripheral regions.

As shown by the optical micrographs in figures 6.3a and 6.3b, THP-1 cells uptake Rd Dex-Gel which localizes exclusively in the peri-nuclear region of the cytoplasm (Cyto, figure 6.3b). Rhodamine fluorescence shows white spots (Rd Dex-Gels) and a cytoplasmic haze which comes from dye being released as Dex-Gels are degraded. Neither, the nucleus (N) nor cell periphery (P) regions contain Dex-Gels while free rhodamine penetrates these regions. Taking advantage of combined optical microscopy and AFM, the nuclear, cytoplasmic, and peripheral regions are selectively indented and found to exhibit different stiffnesses (figure 6.3c). Figure 6.3c shows that the cytoplasmic region is softest with a modulus of 0.649 ± 0.1 kPa, whereas the nucleus and periphery are stiffer with moduli of 0.915 ± 0.07 and 0.876 ± 0.2 kPa, respectively. The nucleus was specifically identified and avoided in future measurements to prevent overestimation of the modulus in association with the observed greater nuclear stiffness. The cytoplasmic region represents a thicker region of the cell, up to 10 μm, which is optimal for nano-indentation (A = 0.5 μm << 10 μm), whereas the periphery is much thinner at circa 1 μm and may appear stiffer due to substrate effects (A = 0.5 μm ~ 1 μm). All further modulus measurements were taken from the cytoplasmic region because the Dex-Gels localize here, the area is sufficiently thick for indentation, and wide enough to allow for multiple measurements of the same cell.

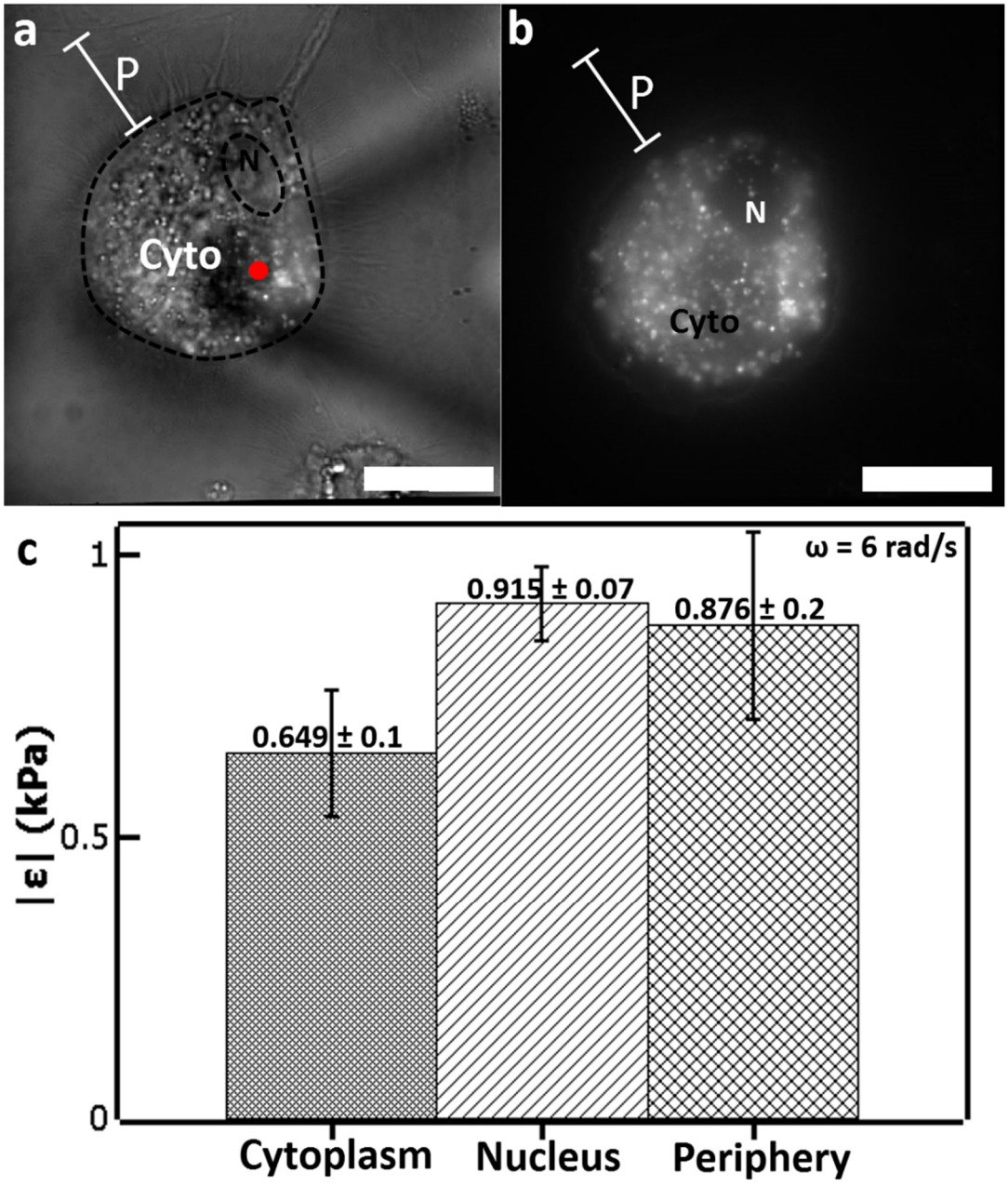

Figure 6.3: Localization of Rd Dex-Gel inside macrophage 24 h after exposure a. Simultaneous white light and fluorescent imaging showing distinguishable components of the cell. Cell periphery, P, cytoplasm, cyto, and nucleus, N, are labeled. The outline of the retracted AFM cantilever is visible and a red dot is drawn to the approximate size of the microsphere indenter. **b.** Red fluorescence image of the same cell shows Rd Dex-Gels (white dots) and diffuse rhodamine (grey cloud) in the cell. Dex-Gels are localized in the cytoplasmic region (Cyto) **c.** Elastic modulus is determined using AFM to show the P, Cyto, and N of the cell exhibit different stiffness. Sample size > 50 measurements per region on 20 cells with a scan frequency of 6 rad/s. Scale bars 20 μm.

6.4 Ag Dex-Gel treated cells are metabolically stressed.

Cell viability studies determine the health of THP-1 cell populations after 24 h of treatment with Dex-Gel (figure 6.4). Calcein violet (blue) intensity measures esterase activity inside cells, while ethidium homodimer (red) penetrates damaged cell membranes. In figure 6.4a-d, dead cells appear entirely red, healthy cells (fully active, intact membrane) appear entirely blue, and injured cells express both dyes. The inset histograms in figure 6.4a-d breakdown dye expression in each cell population by entirely blue, entirely red, or blue and red (purple) cells. Rd Dex-Gel could not be assessed by this method because of background fluorescence from the rhodamine dye. The control cells and the Dex-Gel treated cells (figure 6.4a and 6.4b, respectively) are normally active and healthy (high blue intensity and no red intensity). Ag Dex-Gel treated cells express both dyes indicating reduced esterase activity and membrane damage consistent with silver-induced injury of THP-1 cells. Silver nanoparticles are known to metabolically stress cells by damaging the mitochondrial potential,[31] and thus, expression of both dye is consistent with THP-1 cell shut down *peri-mortem*.

Figure 6.4e shows dead/alive quantification of viability assays for untreated (blue), Dex-Gel (green), Rd Dex-Gel (red), and Ag Dex-Gel (black) THP-1 cells at 24 h. Both the untreated and Dex-Gel treated cells are more than 95% viable, and therefore Dex-Gels are non-toxic to THP-1 cells. The Rd Dex-Gel exposed cells are 90% viable, a higher mortality rate than the control which is consistent with some rhodamine toxicity. Ag Dex-Gels are 62% viable by the dead/alive quantification method suggesting substantial toxicity of the Ag Dex-Gels. However, 92% of the Ag Dex-Gel treated cells are injured and still viable, shown by the purple bar in figure 6.4d, and only 3% of these cells show no esterase activity. 24h exposure to Ag Dex-Gel is optimal to look for modulus changes because the majority of the Ag Dex-Gel treated cells are in an injured state. Thus, the mechanical properties of Ag Dex-Gel treated THP-1 cells can be

correlated with the known toxicity of Ag nanoparticles whereby reduced mitochondrial potential leads to reduced [ATP] in cells and metabolic stress.

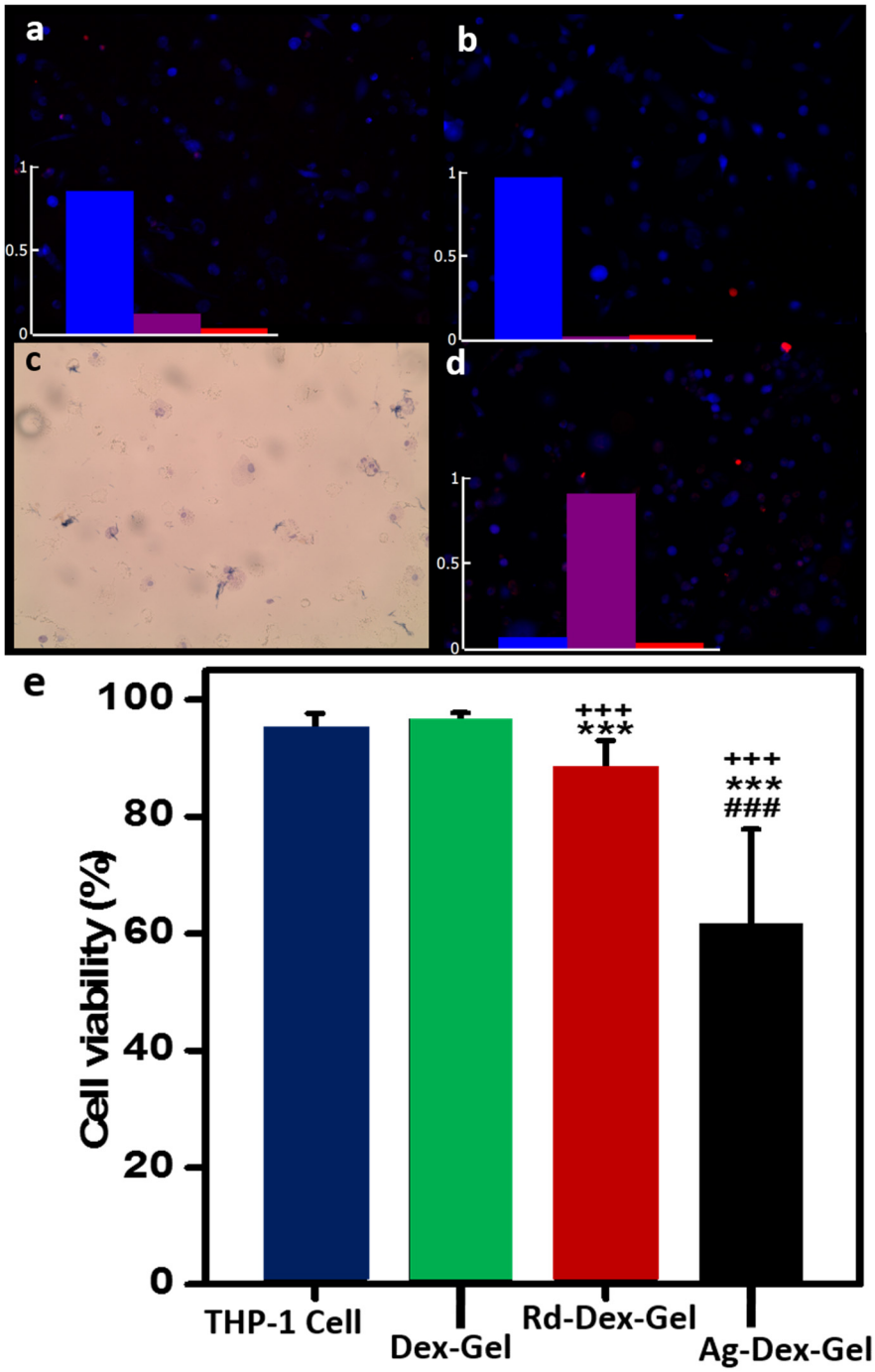

Figure 6.4: Viability staining of macrophages 24 h after exposure to Dex-Gels. a. Untreated Macrophages (Control) appear predominantly healthy (blue staining dominates histogram) **b.** Dex-Gel exposed macrophages are also healthy at 24 h indicating biocompatibility of the carrier. **c.** Rd Dex-Gel loaded macrophages require a different stain due to the fluorescence of the Rhodamine dye, thus no histogram indicated a stressed or unstressed population can be generated. **d.** Ag Dex-Gel loaded macrophages appear to be oxidatively stressed as cells expressing both dye (purple) dominate the histogram. **e.** Viability histogram for all populations. If the intensity of the blue is greater than the intensity of the red dye a cell is counted as alive while inset histograms (a-d) show proportion of each population which expresses blue, red, or both (purple) dyes.

6.5 AFM nano-indentation of THP-1 Cells detects stiffening in stressed cells.

Nano-indentation of THP-1 cell populations is performed across the relevant frequency range for determining viscoelastic parameters. The minimum and maximum indentation frequencies are chosen by determining the indentation rates where the modulus of Dex-Gel treated THP-1 cells becomes independent of frequency. Specifically, at velocities less than 200 nm/s and greater than 10 μm/s no significant changes in modulus with frequency are observed. Viscous entangled media will display a maximum in hysteresis at a frequency corresponding to the relaxation time. Thus, intermediate frequencies are selected by observing where the hysteresis between indentation and retraction curves on Dex-Gel treated THP-1 cells is maximized. Using this guideline, two intermediate velocities were selected, namely, 500 nm/s and 1000 nm/s. Some hysteresis is also observed at the maximum and minimum indentation rates (supplement figure A2.2) which suggests that cells are not purely elastic even at the highest and lowest rates. The average indentation depth (A) is fixed at 500 nm so that cantilever velocity, V, defines a frequency, $\omega = \pi V/A$.

Figure 6.5a shows the distribution of Dex-Gel treated THP-1 cell moduli at frequencies ranging from 1 to 60 rad/s. The mean cell stiffness increases as indentation frequency increases while the shape of the distribution remains similar. Between cells, the variance of the modulus increases with average modulus and is on the order of magnitude of the modulus. Each

individual measurement represents the average of 2-5 indentations on a single cell at each frequency. Multiple modulus measurements at one frequency on the same cell exhibit low variance; therefore, the variance of the modulus distribution is attributed to viscoelastic differences between cells and not to modulus variations within a single cell. The moduli of the Dex-Gel treated population at four different indentation frequencies is well fit by a log-normal distribution with $R^2 > 0.9$. The mean of the distribution, represented by circles, increases from 351 Pa to 612 Pa as indentation frequency increases from 1 rad/s to 60 rad/s, respectively. The accuracy of the fit to a single distribution at all frequencies indicates that subpopulations of cells with different frequency responses are not observed.

Stiffening was observed in THP-1 cells exposed to Rd Dex-Gel or Ag Dex-Gel independent of frequency. Figure 6.5b shows the distribution of the modulus at 3 rad/s for each THP-1 cell population. The distribution for untreated THP-1 cells (blue) is comparable to that of Dex-Gel treated THP-1 cells (green) and both are fit by a log-normal distribution (blue and green dashed lines) with $R^2 = 0.93$ and 0.96, respectively. The average modulus for the untreated and Dex-Gel treated THP-1 cells, represented by circles, are similar, 401 Pa and 427 Pa, respectively. The average moduli of Rd Dex-Gel and Ag Dex-Gel treated cells are greater than control THP-1 cells, 608 Pa and 689 Pa, respectively. The mean Ag Dex-Gel modulus is greater than the mean Rd Dex-Gel modulus, while the mode Rd Dex-Gel modulus is greater than the mode of the Ag Dex-Gel modulus. A broadening in the variance of moduli values for the Ag Dex-Gel THP-1 cells indicates that cells stiffen by different degrees in response to Ag Dex-Gel exposure.

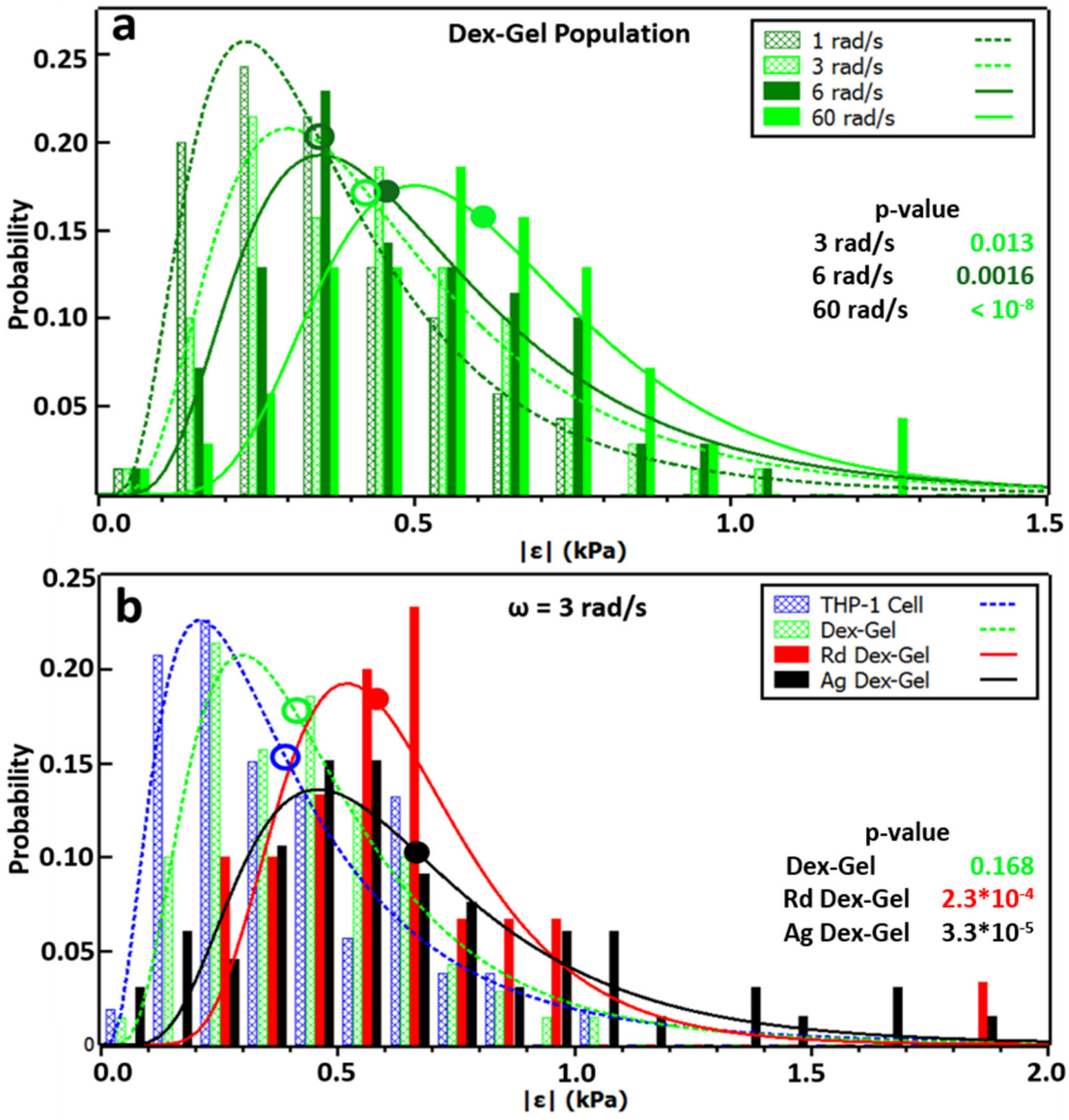

Figure 6.5: Elastic modulus distribution of THP-1 cell populations. a. Dex-Gel exposed macrophage modulus distributions at four different indentation frequencies. Histograms are well fitted by a log-normal distribution at all frequencies. Circles represent mean value of distribution. P-values reflect Mann-Whitney test of distributions compared to 1 rad/s data. **b.** Modulus distribution at 3 rad/s indentation frequency of the four cell populations. Histograms are fit by a single log-normal and dots show mean value. P-values reflect Mann-Whitney test of distribution compared to THP-1 Cell. N = 54; Dex-Gel, N=74; Rd Dex-Gel, N=32; Ag Dex-Gel, N = 67. Each modulus measurement (N) at each frequency is the result of 2-5 independent indentations.

A decrease in the fit quality (table A2.2) correlates with the increase in average |ε| indicating a stiffer subpopulation in the Rd Dex-Gel and Ag Dex-Gel treated cells that is not apparent from visual inspection of the data in figure 6.5b. As the quality of fit degrades for the stressed cell populations (Rd and Ag Dex-Gel), the mean of the distribution (circles) no longer correlates with the mean of the log-normal fit and underestimates the actual mean. This deviation is most substantial in the Ag Dex-Gel population where the mean of the fit is 0.52 kPa, a 24% underestimate, and the R^2 value is relatively low, 0.79. Similarly, for the Rd Dex-Gel treated distribution, the fit average is 0.55 kPa, a 10% underestimate, and the R^2 is 0.8. Thus, a correlation is observed between the stressed state, stiffening, and a degradation of the fit by a single log-normal which can be explained by the appearance of a stiffer subpopulation. While neither the Rd nor Ag Dex-Gel modulus distributions clearly evolve into bimodal distributions, stiff outliers and a reduced R^2 suggests anisotropic stiffening gives rise to stiffer subpopulations (cf. figure 6.5b). None the less, stiffening observed in Rd Dex-Gel and Ag Dex-Gel treated THP-1 cells is likely attributed to injury inflicted by rhodamine and silver inside cells.

In figure 6.6 the frequency dependence of average modulus is shown for all cell populations. As frequency increases, the measured modulus of THP-1 cell increases to a constant value at f = 60 rad/s. At low frequencies the modulus is also insensitive to frequency, and at 1 rad/s the modulus value is approximately the zero-frequency elasticity. At intermediate frequencies (between 1 rad/s and 60 rad/s), the transition between low modulus and high modulus defines the viscosity of the cell. The relative shape of |ε| with frequency is similar for all cell populations; however, at all frequencies a clear increase in the average modulus is observed for THP-1 cells treated with Rd Dex-Gel and Ag Dex-Gel. The basic behavior of |ε| with frequency for THP-1 cells is consistent with the spring and dashpot configuration illustrated (top) in figure 6.6, is known as the standard linear solid model (SLSM) of

viscoelasticity. The SLSM is a good approximation for quantifying the viscoelasticity of healthy and cancerous cells.[14-17]

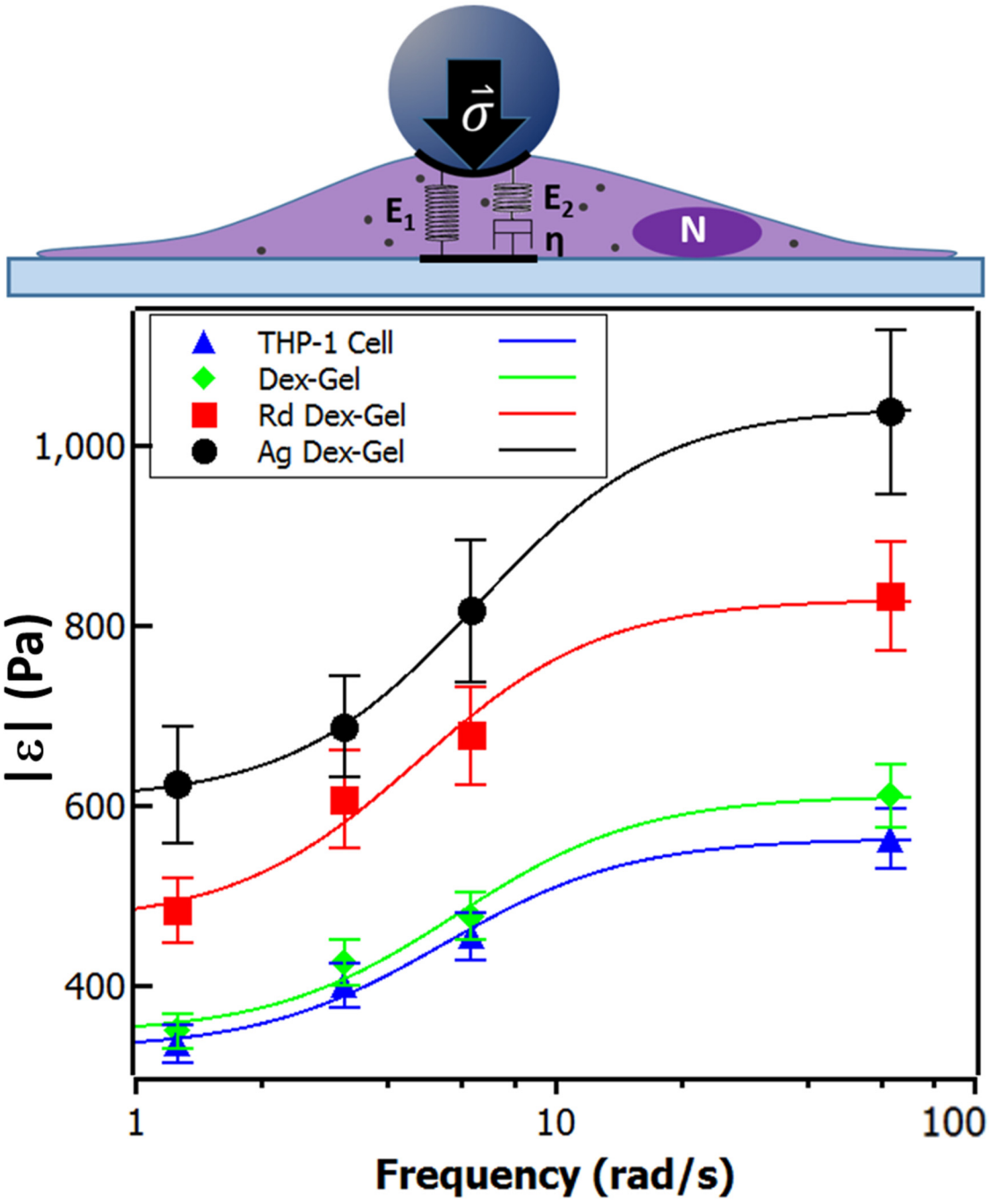

Figure 6.6: Frequency dependence of |Elastic Modulus| enables VIRRAL. Average elastic modulus determined by nano-indentation of THP-1 cells treated with different Dex-Gels is shown over two orders of magnitude of indentation frequency. The most simple viscoelastic model which captures the data is the standard linear solid model (illustrated top). Ag Dex-Gel

and Rd Dex-Gel exposed cells show higher average stiffness (black circles and red squares) Dex-Gel and untreated cells are routinely softer (green diamonds and blue triangles). Solving the equation of motion for the model shown in frequency space (top) yields equation 6.4 to which the data is well fitted. (solid lines) THP-1 Cell, N = 54; Dex-Gel, N=74; Rd Dex-Gel, N=32; Ag Dex-Gel, N = 67. Each modulus measurement (N) at each frequency is the result of 2-5 independent indentations.

	E_1 (Pa)	E_2 (Pa)	η (Pa*s)	τ (s)
TGP-1 Cell	330 ± 18	234 ± 22	38 ± 8	0.16
Dex-Gel	347 ± 27	264 ± 34	34 ± 11	0.13
Rd Dex-Gel	470 ± 45	360 ± 53	67 ± 22	0.18
Ag Dex-Gel	607 ± 3	436 ± 3	58 ± 1	0.13

Table 6.1: Parameters of the standard linear solid model for viscoelasticity of THP-1 Cells.

6. 6 Viscoelastic parameters determined by VIRRAL

The viscoelastic parameters of THP-1 cells are determined by fitting the frequency dependence of the THP-1 cell modulus to the SLSM frequency response. The elastic modulus, ε, is the transfer function relating stress, $\vec{\sigma}$, to strain, $\vec{e}$, as described in equation 6.2,

$$\vec{\sigma} = \varepsilon \vec{e} \quad . \qquad (6.2)$$

For the spring dashpot configuration in figure 6.6 (top), the Laplace transform of the solution to the equation of motion yields the frequency response of the standard linear solid system,

$$\varepsilon = \frac{E_1 E_2 + j\omega\eta(E_1+E_2)}{E2+j\omega\eta} \quad . \qquad (6.3)$$

E_1 and E_2 are the low and high frequency stiffnesses of the elastic elements illustrated in figure 6.6, top, and the strain response of the dashpot is $d\vec{e}/_{dt}\,\eta = j\omega\eta$ where η is the viscosity (Pa*s), *j* is the imaginary unit, and ω is the indentation frequency (rad/s). The experimentally measured parameter "elastic modulus" , |ε|, is determined by fitting the deflection of the AFM cantilever as it contacts the cell to the Hertz equation. |ε| is a real expression,

$$|\varepsilon| = \sqrt{\frac{(E_1E_2)^2+\omega^2\eta^2\,(E_1+E_2)^2}{E_2^2+\omega^2\eta^2}} \quad , \qquad (6.4)$$

that can be directly fit to the data in figure 6.6 (lines in figure 6.6) making it possible to experimentally determine E_1, E_2, and η, the values of which are in table 6.1). The other important parameter than can be extracted from the linear solid model is a relaxation time $\tau = {\eta}/{E_2}$ which represents the biomechanical response time of the cell.

Table 6.1 shows that the Ag and Rd Dex-Gel treated THP-1 cells exhibit a greater value of E_1, E_2, and viscosity compared to untreated and Dex-Gel treated THP-1 cells. The increase in E_1 indicates an up-regulation of immobile elastic structures within the cytoplasm. The increase in E_2 is indicative of stiffening or cross-linking of more mobile structures, and the increase in viscosity suggests a reduction in the mobility of cytoplasmic structures. The relaxation time appears to be conserved in the cell populations independent of state. The conserved τ values suggest that the mechanism which causes cells to become stiffer also makes them proportionally more viscous. The scaling of τ may be attributed to higher cross linking density of cytoskeletal filaments which increases the elastic stiffness and restricts the mobility of small molecules within the medium to flow away from stress (i.e. increasing the viscosity). Furthermore, E_1, E_2, and η values are in good agreement with results from AFM based creep tests.[14-17]

6.7 Physiological significance of frequency response

In addition to being spatially heterogeneous, the complexity of the cortex and cytoplasm make it difficult to unequivocally relate the three parameters (E_1, E_2, η) directly to physiological processes or cellular components. E_1 physically represents an entropic spring which retains its

elasticity independent of time scale. Such stiffness may be attributable to less motile cell contents like the cell membrane, intermediate filament networks, and cross-linked filamentous protein networks that reversibly compress but do not translocate on the seconds timescale. The contribution of elastic component E_2 occurs when the indentation rate exceeds $1/\tau$ and thus comes from the compression of cytoplasmic materials such as proteins and molecular motors which on a slower time scale are able to flow away from the stress.

Similar values of E_1, E_2, and η observed for untreated and Dex-Gel treated THP-1 cells suggest that Dex-Gels alone do not alter cytoskeletal structure. This supports the finding that unloaded Dex-Gels are biocompatible (figure 6.4b). The result also indicates that the mechanical properties of cells are closely linked to their vitality. A false positive for cell stress by AFM (observed stiffening) of this population would indicate that modulus measurements were sensing the incorporation of Dex-Gels within the cell. This finding supports the sensitivity of AFM nano-indentation to cell state and its utility as a non-invasive diagnostic tool for evaluating large populations of cells with single cell specificity.

The observed stiffening (increase in $|\varepsilon|$) of THP-1 cells treated with either Ag Dex-Gels or Rd Dex-Gels is likely attributable to physical stiffening associated with the metabolic stress prevalent in these cells. Both Ag nanoparticles[31] and rhodamine [32] have been associated with injury of mitochondria that inhibits ATP regeneration in cells reducing the ATP/ADP ratio in the cytoskeleton.[31,32] Stiffening in the Rd Dex-Gel treated cells could be explained by an increase in actin polymerization that is known to be induced by a reduction of ATP/ADP and occurs in silver and rhodamine exposed cells.[22] Subsequently, the increased expression of f-actin leads to a higher elastic modulus of the cytoskeleton primarily discernable in the elastic parameter E_1.

Filamentous actin has been shown to be the most important cytoskeletal protein in determining mechanical stiffness[16] and the increase of f-actin expression associated with a decrease in the cytoplasmic ATP/ADP ratio[22] links metabolism to mechanical stiffness. While the link established in this work shows that metabolic stress induces a mechanical stiffening in cells, the link between metabolism and stiffness can also explain the consistent observation that metastatic cancer cells, which are metabolically unregulated are routinely softer than benign cells.[7] Knocking down actin polymerization by cytochalasin D leads to a ten-fold decrease in stiffness[16] from which a reduction in E_1, E_2, and η is expected. Not only will a reduction in f-actin reduce E_1 and soften the cell, but also the confinement of cytoplasmic components within the filament mesh will be reduced leading to a lower cytoplasmic viscosity. The 10 fold decrease in $|\varepsilon|$ observed after cytochalasin D treatment also mandates a reduction in E_2 in association with f-actin depolymerization. This suggests that some of the cytoplasmic actin filaments are mobile on a time scale proportional to η/E_2 (~ 100 μs). At indentation rates greater than E_2/η these filaments contribute to $|\varepsilon|$. Thus, the three key parameters associated with the linear solid model are extremely informative correlating cell disease state to metabolism, whereby E_1 is an indicator of the filamentous actin expression and cross-linking density and E_2 and η reflect changes in cell dynamics.

6.8 Conclusions: VIRRAL enables correlation of viscoelastic parameters to cell metabolism.

This study evaluates the efficacy of Dex-Gel drug carriers as biocompatible delivery agents of small molecule (rhodamine) and nanoparticle (Ag) dosages as well as AFM nano-indentation as a potential non-invasive diagnostic tool for measuring cell health. Fluorescence microscopy shows that Dex-Gels are incorporated into the cytoplasm of cells and are digested. Viability assays indicate that unloaded Dex-Gels are biocompatible (>95% vitality at 24 h) and

that Ag Dex-Gel treated THP-1 cells are injured in association with the release of Ag in the cytoplasm damaging mitochondria (figure 6.4d). AFM nano-indentation detects higher stiffness in Ag Dex-Gels and Rd Dex-Gels at all indentation frequencies(figures 6.5b and 6.6) while no stiffness change is observed for unloaded Dex-Gel exposed cells compared to unexposed (control) THP-1 cells. Together these results show that Dex-Gels are a viable candidate as inert drug carriers and AFM nano-indentation is capable of distinguishing between populations of THP-1 cells which are stressed or unstressed. The analysis of the frequency dependence of modulus is also novel because it shows that viscoelasticity (elasticity and viscosity) can be accurately determined from the frequency dependence of modulus measurements from AFM nano-indentation. This allows for higher throughput and a larger dynamic range in analyzing cells as compared to conventional creep tests. Preforming this test over a larger bandwidth may allow more information about the cellular response to be obtained by extending the frequency response of $|\varepsilon|$ beyond the standard linear solid model. These experimental results should facilitate the development of cell viscoelasticity models that reflect the complexity (i.e., organelle level resolution) of stressed and healthy cells.

6.9 References

1. Engler AJ, Sen S, Sweeney HL, Discher DE, Matrix Elasticity Directs Stem Cell Lineage Specification, *Cell*, 126, **2006**, 677-689.
2. Fletcher DA, Mullins RD, Cell mechanics and the cytoskeleton, *Nature*, 463, **2010**, 485-492.
3. Shirwany NA, Zou M-h, Arterial Stiffness: a brief review, *Acta Pharmacologica Sinica*, **2010**, 31, 1267-1276.
4. Fritsch A, Hockel M, Kiessling T, Nnetu KD, Wetzel F, Zink M, Kas JA, Are biomechanical changes necessary for tumor progression?, *Nature Physics*, 6, **2010**, 730-733.
5. Hoyert DL, Xu J, Deaths: Preliminary Data for 2011, *National Vital Statistics Reports*, 61, 6, **2011**, 1-52
6. Wirtz D, Konstantopoulos K, Searson PC, The Physics of Cancer: the role of physical interactions and mechanical forces in metastasis, *Nature Rev Cancer*, 11, **2011**, 512-522.
7. Cross SE, Jin Y-S, Rao J, Grimzewski JK, Nanomechanical analysis of cells from cancer patients, *Nature Nanotechnology*, 2, **2007**, 780-782.

8. Paszek MJ, Zahir N, Johnson KR, Lakins JN, Rozenberg GI, Gefen A, Reinhart-King CA, Margulies SS, Dembo M, Boettiger D, Hammer DA, Weaver VM, Tensional homeostasis and the malignant phenotype, *Cancer Cell*, 8 **2005**, 241-254.
9. Gonzalez-Rodriguez D, Guevorkian K, Douezan S, Bouchard-Wyart F, Soft Matter Models Developing Tissue and Tumors, *Science*, 338, **2012,** 910-917.
10. Steinberg MS, Shafrir Y, Foty RA, Forgacs G, Viscoelastic Properties of Living Embryonic Tissues: a Quantative Study, *Biophysical Journal*, 74, **1998**, 2227-2234.
11. Pajerowski JD, Dahl KN, Zhong FL, Sammak PJ, Discher DE, Physical plasticity of the nucleus in stem cell differentiation, *PNAS,* 104, **2007**, 15619-15624.
12. Nawaz S, Sanchez P, Bodensiek K, Li Sai, Simons M, Schaap IAT, Cell Visco-Elasticity Measured with AFM and Optical Trapping at Sub-Micrometer Deformations, *PLOS One*, 7, 9, **2012**, e45297.
13. Hendricks AG, Holzbaur ELF, Goldman YE, Force measurements on cargoes in living cells reveal collective dynamics of microtubule motors, *Proceedings of the National Academy of Science*, 109, 45, **2012**, 18477-18452.
14. Darling EM, Topel M, Zauscher S, Vail TP, Guilak F, Viscoelastic properties of human mesenchymally-derived stem cells and primary osteoblasts, chondrocytes, and adipocytes, *Journal of Biomechanics* 41, **2008**, 454-464.
15. Darling EM, Zauscher S, Block JA,, Guilak F, A Thin-Layer Model for Viscoelastic, Stress-Relaxation Testing of Cells Using Atomic Force Microscopy: Do Cell Properties Reflect Metastatic Potential?, *Biophysical Journal*, 92, **2007**, 1784-1791.
16. Ketene AN, Roberts PC, Shea AA, Schmelz EM, Agah M, Actin filaments play a primary role for structural integrity and viscoelastic response in cells, *Integrative Biology*, 4, **2012**, 540-549.
17. Ketene AN, Schmelz EM, Roberts PC, Agah M, The effects of cancer progression on the viscoelasticity of ovarian cell cytoskeleton structures, *Nanotechnology*, 8, **2012**, 93-102.
18. Radmacher M, Fritz M, Kacher CM, Cleveland JP, Hansma PK, Measuring the Viscoelastic Properties of Human Platelets with the Atomic Force Microscope, *Biophysical Journal*, 70, **1996**, 556-567.
19. Rebelo LM, de Sousa JS, Mendes Filho J, Radamacher M, Comparison of the viscoelastic properties of cells from different kidney cancer phenotypes measured with atomic force microscopy, *Nanotechnology*, 24, **2013**, 055102.
20. Seltmann K, Fritsch AW, Kas JA, Magin TM, Keratins significantly contribute to cell stiffness and impact behavior, *PNAS*, 110, 46, **2013**, 18507-18512.
21. Snider NT, Omary MB, Post-translational modifications of intermediate filament proteins: mechanisms and functions, *Nature Reviews Molecular Cell Biology*, 15, **2014**, 163-177.
22. Atkinson SJ, Hosford MA, Molitoris BA, Mechanism of Actin Polymerization in Cellular ATP Depletion, *Journal of Biological Chemistry*, 279, **2004**, 5194-5199
23. Cairns RA, Harris IS, Mak TW, Regulation of cancer cell metabolism, *Nature Review Cancer*, 11, **2011**, 85-95.
24. Swift J, Ivanovska IL, Buxboim A, Harada T, Dingal PCDP, Pinter J, Pajerowski JD, Spinler KR, Shin J-W, Tewari M, Rehfeldt F, Speicher DW, Discher DE, Nuclear Lamin-A Scales with Tissue Stiffness and Enhances Matrix-Directed Differentiation, *Science*, 341, **2013**, 1240104.
25. Desgrosellier JS, Cheresh DA, Integrins in cancer: biological implications and therapeutic opportunities, *Nature Reviews Cancer*, 10, **2010**, 9-22.

26. Krieg M, Dunn AR, Goodman MB, Mechanical control of the sense of touch by β-spectrin, *Nature Cell Biology*, 16, **2014**, 224-233.
27. Fischer RS, Myers KA, Gardel ML, Waterman CM, Stiffness-controlled three-dimensional extracellular matrices for high-resolution imaging of cell behavior, Nature Protocols, 7, 11, **2012**, 2056-2064.
28. Boudou T, Ohayon J, Picart C, Tracqui P, An extended relationship for the characterization of Poisson's ratio of tunable polyacrylamide gels, *Biorheology*, 43, 6, **2006**, 721-728.
29. Vargas-Pinto R, Gong H, Vahabikashi A, Johnson M, The Effect of the Endothelial Cell Cortex on Atomic Force Microscopy Measurements, *Biophysical Journal*, 105, **2013**, 300-309.
30. Ferrer MCC, Sobolewski P, Composto RJ, Eckmann DM, Cellular Uptake and Intracellular Cargo Release from Dextran Based Nanogel Drug Carriers, *Journal of Nanotechnology in Engineering and Medicine,* 4 **2103**, 011002.
31. AshanRani PV, Mun GLK, Hande MP, Valiyaveettil S, Cytoxicity and Genotoxicity of Silver Nanoparticles in Human Cells, *ACS Nano,* 3, 2, **2009**, 279-290.
32. Alante A, Passarella S, Moreno G, Salet C, Effects of Rhodamine 123 in the Dark After Irradation on Mitochondrial Energy Metabolism, *Photochemistry and Photobiology*, 56,4, **1992** 471-478.

Chapter 7: Summary and Future Direction

7.0 Introduction

The widespread use of nanoparticles in biological applications is on the rise, while an understanding of NP toxicology is in its infancy. Predicting the toxicity of NPs is generally synonymous to identifying the biomolecules or organelles that NPs will interact with in the dense array of protein, nucleic acid, salt, and lipid inside the cell. Figure 7.1 outlines the experimentally observed effects of NPs on biological material and the predicted resulting cytotoxicity. This dissertation describes effects of non-specific binding of cationic nanoparticles (NPs) to biological material ranging from persistence length reduction of single actin filaments (cf. chapter 4), to modified kinetics of myosin motility (cf. chapter 5), and culminating with the detection of metabolic changes induced by silver loaded nanogels on THP-1 cells (cf. chapter 6). The experimental techniques range from atomic force characterization of cellular viscoelastic properties, down to single molecule tracking of quantum dot labeled myosin V translocation on nanoparticle-immobilized actin filaments by fluorescent imaging with one nanometer accuracy (FIONA). This chapter summarizes the key results in chapters 3-6 and provides motivation for future direction in extending the findings of this dissertation.

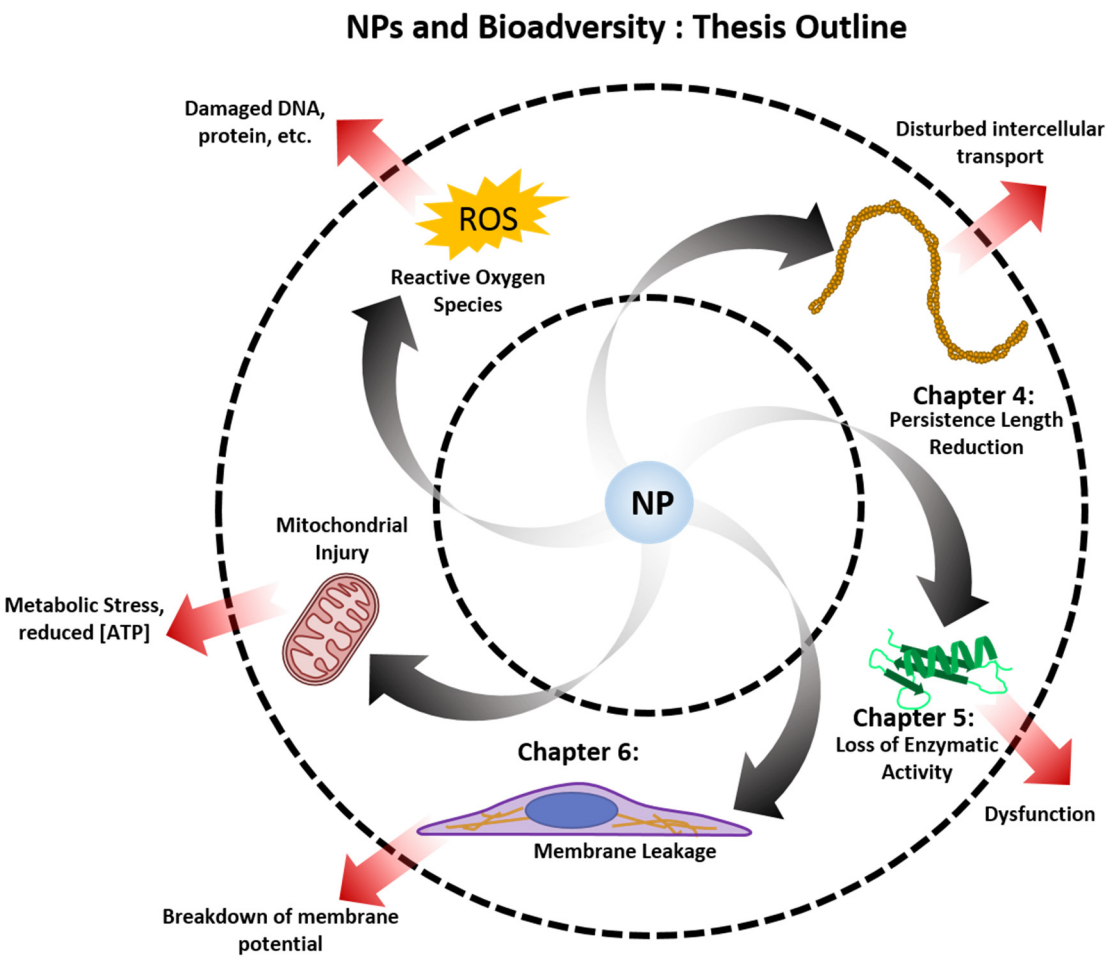

Figure 7.1: Overview of the bioadverse effects of nanoparticles addressed in this thesis.

7.1 Summary

The majority of the biological studies in this dissertation rely on precision roughness control of amine-functionalized NP-SAA composite films to tune the interaction between the surface and f-actin. The process for creating these surfaces in described in chapter 3. Poly(styrene-random-tertbutyl acrylate) thin-films, 100 nm thick, are converted to poly(styrene-random-acrylic acid), SAA, by thermal annealing at 135 to 200 ^{o}C to generate films with AA composition ranging from 2% to 29%. Amine functionalized NPs, 45 nm in diameter, are then grafted to SAA films activated with succinimide and swollen in ethanol. Film composition greatly

changes both the thermodynamics and kinetics of the NP grafting process. Namely, NP attachment becomes saturated at a monolayer for 4% AA films, SAA4, consistent with NPs being unable to sink into SAA4 films. Greater AA fractions than 4% exhibit NP multilayers and hierarchical roughness exceeding 45nm consistent with the thermodynamically favored entry of NPs into the SAA. Quartz crystal microbalance confirms the entry of NPs into SAA13 by measuring a deposited mass consistent with more than 3 close packed layers of NPs. The kinetics of NP grafting scale with the fraction of AA and greater AA content leads to faster NP interdiffusion. Highly roughened surfaces are observed for AA content of SAA13 and SAA29, and the majority of these surfaces exhibit super hydrophobicity, contact angle > 170^{o}.

The tunable surface roughness attained by high loading (jamming) of nanoparticles into SAA thin films while maintaining optical transparency is applied to study the adhesion of f-actin to NP-SAA composite coated glass coverslips. Aggregation of nanoparticles within the SAA increases the film scattering which reduces the fluorescent resolution. By precision manipulation of the thermodynamics and kinetics of NP incorporation in SAA films, the RMS roughness can be tuned from a few nms to hundreds of nms without compromising surface transparency as described in chapter 3. RMS roughness is shown to modulate actin binding strength between immobilized, side-on-wobbly, or end-on attachment of filaments. Chapter 4 describes the relationship between RMS roughness and actin binding strength. The persistence length of actin relates the size and spacing of surface features to f-actin binding strength through the worm-like chain model. Bends of f-actin tighter than the persistence length are observed more regularly on surfaces with increased actin affinity. Regular sub-persistence length bends suggest that structural changes in f-actin are induced by surface attachment.

To test the degree of f-actin structural change, myosin V motility is characterized on surfaces of varying NP diameter and RMS roughness in chapter 5. Myosin V velocity is found to

be slowed due to an increased frequency of backward stepping which indicates that the inter-head coordination of the processive dimer is disrupted on NP-immobilized actin filaments. The Michaelis-Menten relationship of myosin velocity vs ATP concentration on NP-immobilized actin shows a reduction in K_M and V_{MAX} that is explained by backwards stepping and an increased ADP affinity of the actomyosin complex. Both backwards stepping and increased ADP affinity can be explained by a reduced coordination between myosin and actin caused by structural disturbances in actin resulting from NP-actin binding. Limited coordination of actomyosin reduces the nucleotide byproduct release of myosin that is directly linked to the structural changes associated with the force-generating power-stroke of myosin. The results show that non-specific absorption of protein to cationic NPs can decrease protein catalytic activity. The induced kinetic changes of the actomyosin interaction investigated in chapter 6 are a mechanism by which intra-cellular association of actin with cationic NPs would negatively impact transport efficiency and may induce metabolic stress.

A slowing down of molecular motors would manifest as an effective viscosity increase at the periphery of the cell where myosin dominates vesicular transport and actin filaments are a dense meshwork. Local viscoelastic changes may be detectable externally through nanoscale indentation by atomic force microscopy, however methods sensitive enough to probe local viscoelasticity within cells are lacking. Chapter 7 outlines the method of variable indentation-rate rheometric analysis by Laplace transform (VIRRAL) which is developed to utilize basic Hertzian fitting of force curves collected at different rates to extract the frequency dependent viscoelastic modulus by fitting modulus versus indentation frequency to the standard linear solid model. The utilization of novel drug carriers, Dex-Gels, to coat Ag nanoparticles, leads to the rapid ingestion of AgNPs by THP-1 cells and subsequent mitochondrial damage which metabolically stresses cells and decrease cytoplasmic ATP concentration. The ATP decrease

leads to increased f-actin concentration and slowed intracellular transport which is detected as an increase in complex modulus of the cytoplasm of the THP-1 cells. The low-frequency elastic term and the viscous term increase in metabolically stressed THP-1 cells in correlation with increased f-actin expression and while the fundamental relaxation time of the cell, τ, remains conserved as viscous and elastic changes scale proportionally.

7.2 Future work

In this dissertation, the cornerstone techniques of materials science and physiology are combined to study perturbations in molecular motors kinetics induced by nanoparticle-decorated surfaces. Recent developments in single molecule tracking software has enabled routine measurement of diffusion coefficients from single-molecule trajectories *in-vivo*.[1] However, these techniques have not been applied to study NP toxicology, *in-vivo* molecular motility, or polymer-NP interdiffusion. Directly analogous to the fluorescence techniques utilized in this dissertation to measure NP-induced changes of myosin V kinetics, diffusive tracking *in-vivo* has the propensity to directly detect in intracellular transport associated with NP toxicology by tracking molecular motor translocation *in-vivo.* Performing simultaneous viscoelastic measurements on cells using the VIRRAL technique, while tracking molecular motility *in-vivo* will enable the correlation between molecular motor activity and viscoelasticity. To date, studies of this sophistication have yet to be realized. These studies will enable direct correlation between viscoelastic parameters, E_1, E_2, and η with intercellular transport phenomena such as molecular motor density, and $v([ATP])$ analogous to chapters 5 and 6.

7.3 Concluding remarks

Looking forward, there is a great deal to be investigated regarding the interaction of nanomaterials with biological molecules. While the widespread use of nanoparticles in

sunscreens, cosmetics, and pharmaceuticals, makes their contact with people an everyday affair, identifying the toxicological effects of NPs has been lagging. Progress is ongoing to dissect the fundamental physical parameters of NPs that lead to cellular injury through both *in-vivo* and *in-vitro* studies. While *in-vitro* studies lend themselves to a high degree of spatial and temporal resolution and precision control over environmental conditions, correlating *in-vitro* results, such as NP-induced loss of enzyme activity, with observed cytotoxicity is not straightforward. Conversely, *in-vivo* studies enable the direct observation of cytotoxicity by NPs, but dissecting the mechanism is not always possible due to the complex environment of the cytoskeleton and limitations in tracking or measuring intercellular properties. Thusly, the new techniques explored in this study, such as the hierarchical topography, fluorescent imaging in one nanometer accuracy (FIONA), and variable indentation-rate rheometric analysis by Laplace transform (VIRRAL), can be applied simultaneously to correlate molecular motor dynamics with NP toxicology, or track diffusion of NPs within cells while simultaneously probing for changes in viscoelastic properties. Furthermore, tracking of NPs in polymer matrices at sub-diffraction resolution has the propensity to directly test models for polymer-NP interdiffusion, namely, NP "hopping" diffusion and/or the existence of faster polymer chain dynamics at the interface of a polymer film.

7.4 References

1. Persson F, Linden M, Unoson C, Elf J, Extracting intracellular diffusive states and transition rates from single-molecule tracking data, *Nature Methods*, **2013**, 10, 265-269.

Appendix 1: Supporting Information for

Chapter 5

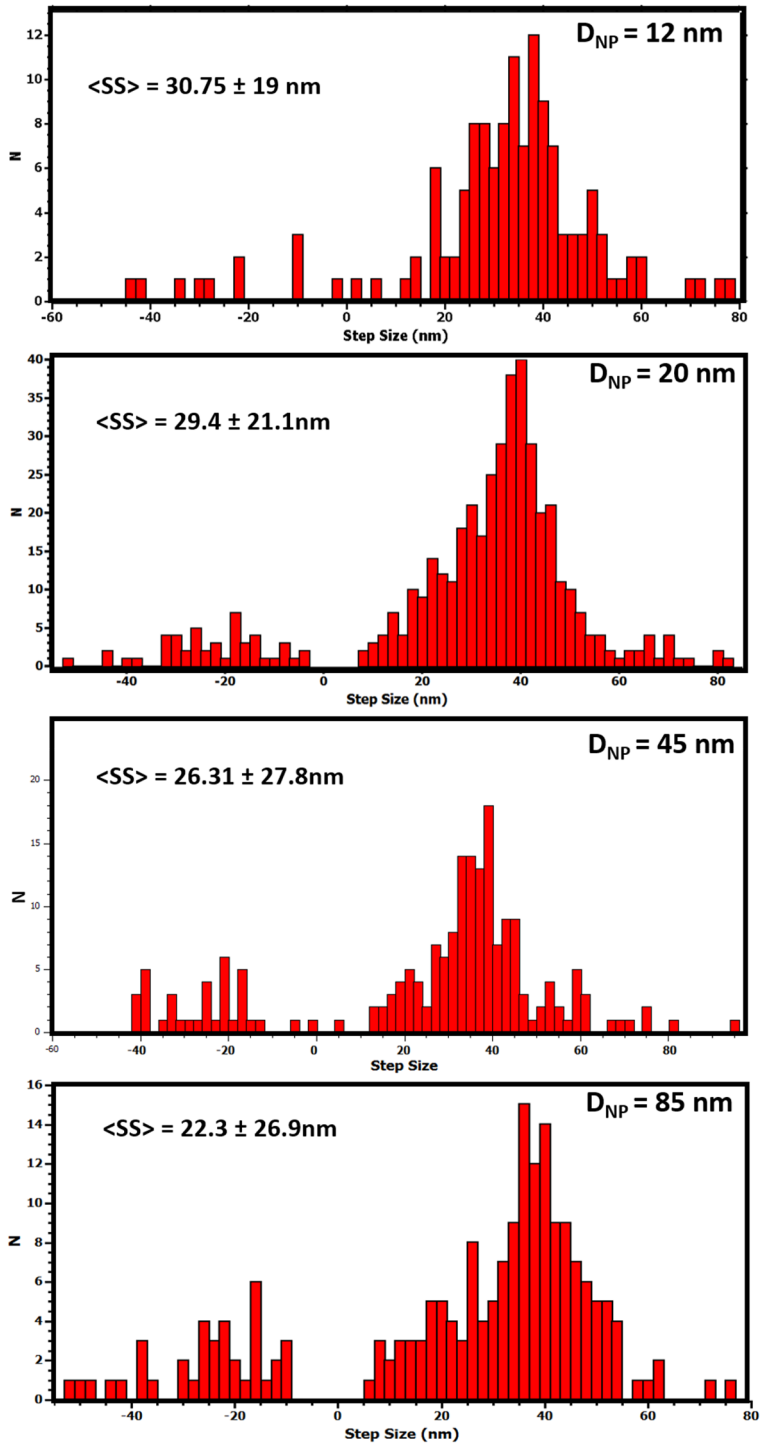

Figure A1.1: Step Size distributions of myosin V on surfaces of different D_{NP}.

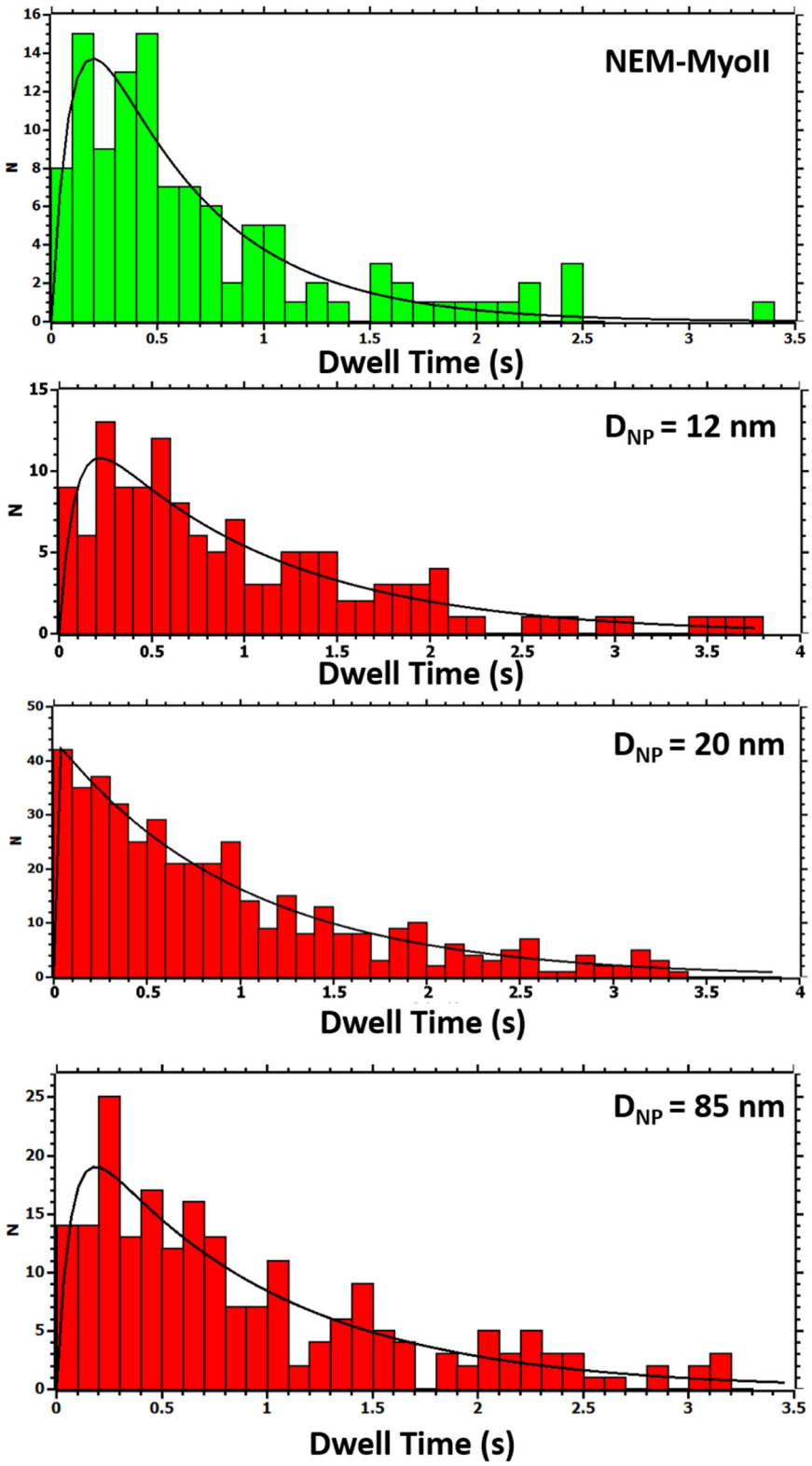

Figure A1.2: Dwell time distributions of myosin V on surfaces of different D_{NP}.

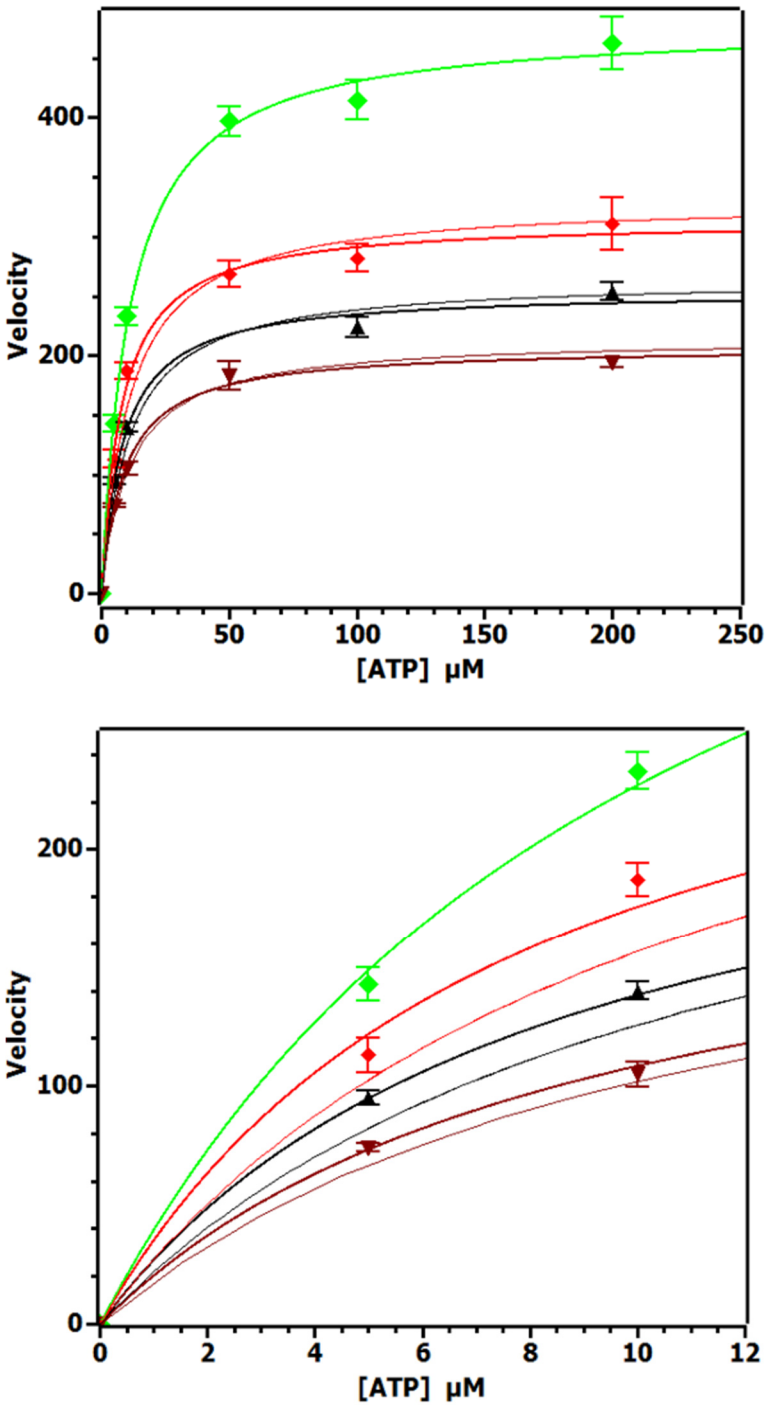

Figure A1.3 Comparison of fits to data with and without K_M fixed. Thin lines shows fit to backwards stepping only, where by K_M and V_{MAX} are fixed to control values compared to thick lines where K_M is allowed to change.

Surface	f_{BS} %	K_{ADP-}	K_M*	V_{max}*
20nm Med	15.0 ± 1.1	-	11.1	478
45nm Med	22.2 ± 1.0	-	11.1	478
85nm Low	27.0 ± 0.4	-	11.1	478

* Values Fixed as Control Values

Table A1.1: Summary of fit parameters where K_M and V_{MAX} are held constant. The approximation of backwards step percent from velocity data when K_M does not change. (Fit curves are shown by the thin lines in figure A1.3).

	BS%	<SS>	S Error	<DT>	S Error	%V by <SS>	%V by BS
Control	0.8	37.1	1.26	0.84	0.08	-	-
12	6.7	31.65	1.9	0.99	0.07	0.88	0.87
20	10	29.35	1	0.9	0.04	0.815	0.8
45	9.3	28.7	1.4	1.5	0.15	0.797	0.813
85	14.7	27.3	2	1.07	0.06	0.76	0.71
85	17.9	22.3	1.9	0.96	0.08	0.62	0.64

Table A1.2: Summary of data collected on NP-decorated surfaces.

Surface	K_M	V_{Max}
Control	11.1 ± 0.9	478 ± 9.0
20 nm Low	6.7 ± 1.5	156 ± 8.5
20 nm Med	7.89 ± 1.0	314 ± 8.7
20 nm High	9.69 ± 1.3	393 ± 14
45 nm Med	8.4 ± 1.2	255 ± 8.9
85 nm Med	9.15 ± 0.9	208 ± 5.3
85 nm High	10.98 ± 4.65	308.8 ± 34.6

Table A1.2: Summary of fit parameters on NP-decorated surfaces.

Appendix 2: Supporting Information for

Chapter 6

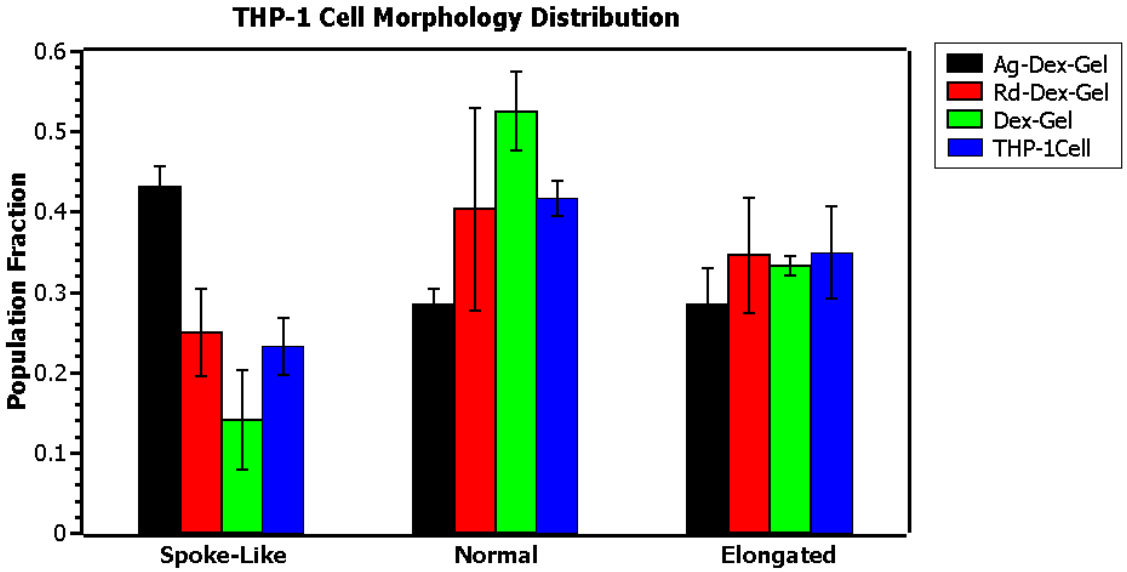

Figure A2.1: THP-1 cell shape. The shape of THP-1 cells treated with different Dex-Gels is shown by analysis of 150x optical microscopy. Cells are imaged and classified as spoke-like, elonaged, or normal. THP-1 Cell, N = 104; Dex-Gel, N=78; Rd Dex-Gel, N=52; Ag Dex-Gel, N = 95. The experiment was performed in duplicate and averaged from which standard deviations (error bars) were determined.

	1 rad/s	3 rad/s	6 rad/s	60 rad/s
A	0.257 ± 0.01	0.21 ± 0.01	0.192 ± 0.01	0.18 ± 0.02
σ	1.46 ± 0.03	0.57 ± 0.4	0.53 ± 0.04	0.40 ± 0.04
μ	-1.46 ± 0.04	-1.211 ± 0.05	-1.04 ± 0.05	-0.69 ± 0.04
R^2	0.99	0.96	0.92	0.88

Table A2.1: Fit parameters for log-normal distributions in figure 5a.

	Ctrl	Dex-Gel	Rd Dex-Gel	Ag Dex-Gel
A	0.23 ± 0.02	0.21 ± 0.01	0.19 ± 0.02	0.14 ± 0.01
σ	0.7 ± 0.06	0.57 ± 0.4	0.36 ± 0.05	0.5 ± 0.06
μ	-1.57 ± 0.07	-1.211 ± 0.05	-0.66 ± 0.05	-0.78 ± 0.06
R^2	0.93	0.96	0.8	0.79

Table A2.2: Fit parameters for log-normal distributions in figure 5b.

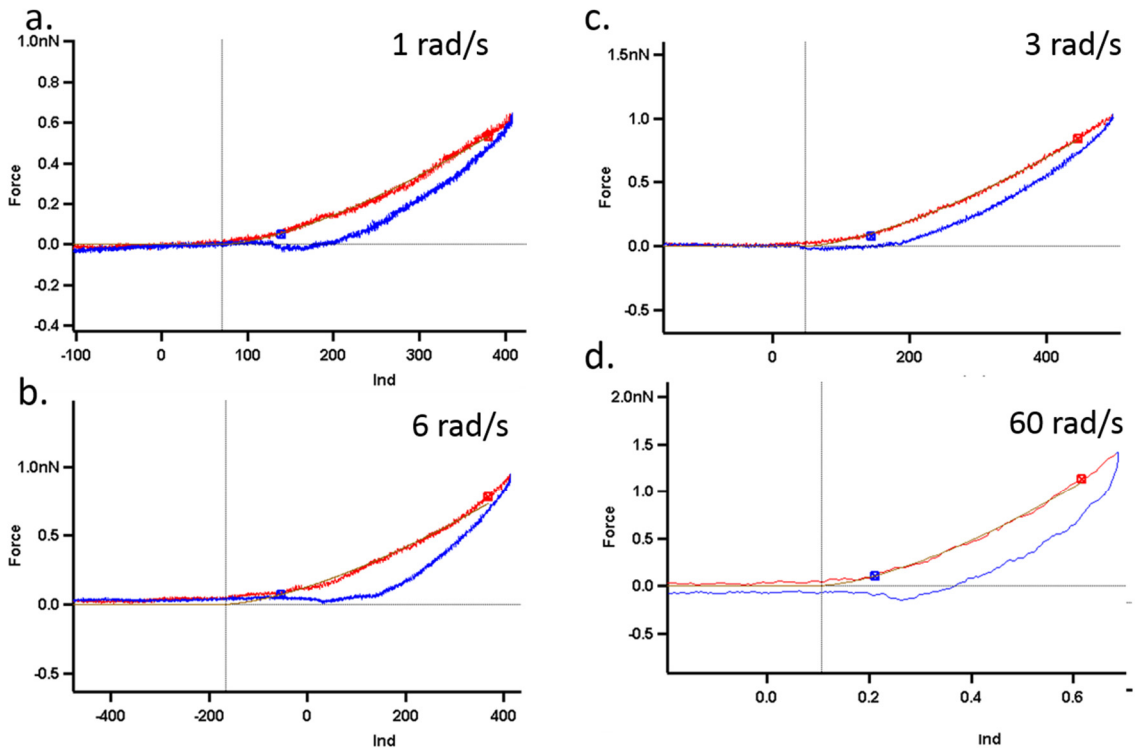

Figure A2.2: Exemplary indentations and Hertz model fits for THP-1 cells. a-d. Force (cantilever deflection*spring constant) is plotted vs indentation depth (Z-sensor) at the 4 different scan velocities (200 nm/s, 500nm/s, 1000 nm/s, 10000 nm/s) used to probe THP-1 cell modulus. **a.** At 200nm/s the minimum realistically obtainable hysteresis is observed while the force reached at A=500nm is around 600pN. **b.** At 500 nm/s the hysteresis is larger than at 200 nm/s and the force realized increases to just under 1 nN. **C.** At 1000 nm/s the hysteresis has increased from lower values and the force realized is just above 1 nN. **d.** At 10000 nm/s the hysteresis does not change significantly with ~ 1000nm/s changes in velocity and the maximum reliable velocity is observed. The force realized is near 1.5 nN and a slight separation between indentation and retraction indicates hydrodynamic forces on the cantilever will be prohibitive of obtaining reliable results at increased tip velocities.